Lunar Laser Ranging for Autonomous Cislunar Spacecraft Navigation

Matthew P. Zaffram

Thesis submitted to the Faculty of the
Virginia Polytechnic Institute and State University
in partial fulfillment of the requirements for the degree of

Master of Science
in
Aerospace Engineering

Riley M. Fitzgerald, Chair
Kevin K. Schroeder
Shane D. Ross
Samantha P. Kenyon

June 27, 2023
Blacksburg, Virginia

Keywords: Halo, Lyapunov, Cislunar, xGEO, Autonomous, Navigation

Lunar Laser Ranging for Autonomous Cislunar Spacecraft Navigation

Matthew P. Zaffram

(ABSTRACT)

The number of objects occupying orbital regimes beyond Geosynchronous Earth Orbit and cislunar space are expected to grow in the coming years; Especially with the Moon reemerging as the latest frontier in the race for space exploration and technological superiority. In order to support this growth, new methods of autonomously navigating in cislunar space are necessary to reduce demand and reliance on ground based tracking infrastructure. Periodic orbits about the first libration point offer favorable vantage points for scientific or military spacecraft missions involving the Earth or Moon. The work presented in this thesis develops a new autonomous spacecraft navigation method for cislunar space and analyzes its performance applied to Lyapunov and halo orbits around L_1. This method uses existing lunar ranging retroreflectors (LRRR) that were installed on the Moon's surface in the 1960s and 1970s. A spacecraft can make laser ranging measurements to the LRRR to estimate its position and velocity. A simulation platform was created to test this concept in the circular restricted three body problem and evaluate its performance. This navigation method was found to be the most successful for a subset of Lyapunov and halo orbits when cycling the five measurement targets. Simulation data showed that sub-kilometer position estimation and sub 2 centimeter per second velocity accuracies are achievable without receiving any state updates from external sources.

Lunar Laser Ranging for Autonomous Cislunar Spacecraft Navigation

Matthew P. Zaffram

(GENERAL AUDIENCE ABSTRACT)

The number of objects occupying the space between the Earth and Moon (cislunar space) are expected to grow in the coming years as the Moon regains popularity in the latest race for space exploration and technological superiority. In order to support this growth, new methods of determining a spacecraft's position and velocity while in this region of space are necessary to reduce dependence on Earth-based methods. Repeating orbits around the equilibrium point between the Earth and Moon provide valuable observation points for scientific and military spacecraft missions. This thesis develops a new spacecraft navigation method for cislunar space and analyzes how well it performs in Lyapunov and halo orbits. This method uses existing laser reflector panels on the Moon's surface that were installed during the 1960s and 70s. A spacecraft can use these panels to make distance measurements in order to estimate its position and velocity. Software was written to simulate the motion of a spacecraft as it is acted on by gravity from the Earth and Moon. Different scenarios were then simulated to test this concept and evaluate its performance. Lunar laser ranging was found to be successful for a some Lyapunov and halo orbits when switching between the five different reflector panels on the Moon. Data generated from the simulations show that position can be estimated with errors less than 1 km, and velocity error on the order of a few centimeters per second, all without receiving any additional information from Earth based systems.

Dedication

To my parents for inspiring and encouraging me to pursue the things I love and for providing me with the opportunities to do so.

Acknowledgments

I would like to thank my advisor Dr. Riley Fitzgerald for all of the guidance and support he has provided for me during my time at Virginia Tech. Without his direction and seemingly endless depth of knowledge, this thesis would not have been possible.

Thank you to my committee members, Dr. Kevin Schroeder, Dr. Samantha Parry Kenyon, and Dr. Shane Ross all of the feedback and thought provoking conversations we have had during the last few semesters.

Thank you to all of the awesome teachers and professors I have had this far in my academic career. I definitely would not be where I am today with out your influences and inspiration over the years.

Thank you to my friends, girlfriend, and family for your mentorship, love, and support.

Lastly, thank you to all of the strangers in Blacksburg, VA for letting me pet your dogs while I was away from my own.

Contents

List of Figures

List of Tables

List of Abbreviations

L_1 Libration Point 1

ADCS Attitude Determination and Control System

DOD United States Department of Defense

DRO Distant Retrograde Orbit

DSN Deep Space Network

EDL Entry Descent and Landing

EKF Extended Kalman Filter

GEO Geosynchronous Orbit

GNC Guidance Navigation and Control

GNSS Global Navigation Satellite Systems

GPS Global Positioning System

GRAIL Gravity Recovery and Interior Laboratory

GSSAP Geosynchronous Space Situational Awareness Program

HEO High Earth Orbit

JPL Jet Propulsion Laboratory

JWST James Webb Space Telescope

LCRD Laser Communications Relay Demonstration

LEO Low Earth Orbit

LLRE Lunar Laser Ranging Experiment

LPO Libration Point Orbit

LRO Lunar Reconnaissance Orbit

LRRR Lunar Ranging Retroreflectors

MEO Medium Earth Orbit

NASA National Aeronautics and Space Administration

NHRO Near Rectilinear Halo Orbit

NSN Near Space Network

SBSS Space Based Space Surveillance System

SDA Space Domain Awareness

SSN United States Space Surveillance Network

STM State Transition Matrix

TDRSS Tracking and Data Relay Satellite System

xGEO Orbital regime beyond GEO, used interchangeably with cislunar

Chapter 1

Introduction

In recent years, there has been a trending wide spread interest in orbital regimes beyond Geosynchronous Orbit, or "xGEO," extending out to the Moon. Much of this can be attributed to revived ambitions of sending robotic and human exploration missions back to the Moon and beyond with NASA's Artemis missions. As these efforts begin to gain traction, a number of other countries have announced plans of sending their own exploration missions to the Moon [7]. The region between the Earth and moon, or the "cislunar" region, has also gained popularity in the science communities. Especially with the long awaited James Webb Space Telescope (JWST) recently coming online and demonstrating the unique science that can be conducted at libration points in this region of space. Another trend in the space exploration community is a preference towards small spacecraft and dis-aggregated, distributed systems for deep space missions [8, 9]. Additionally, xGEO has the attention of the US Department of Defense (DOD) as it prioritizes efforts to improve space domain awareness (SDA), space traffic management, and operational capabilities in this region to monitor and protect the developing infrastructure and assets operating in this region [7, 10, 11]. Since almost all of the deep space satellites in operation are dependent on the Deep Space Network (DSN) for providing precise telemetry updates via radiometric tracking [12], the anticipated demand increase from this influx of spacecraft populating or transiting through xGEO will eventually overload the DSN [8, 13]. This necessitates either improving the capacity of the Deep Space Network or developing viable methods of autonomous navigation in cislunar

space. The latter of these is the focus of the research presented in this thesis. The aim of this work is to propose a new method of autonomous cislunar navigation, develop the concept of operations, and create a simulation platform to evaluate the performance. The method will be applied to periodic orbits about the first libration point, L_1, in the Earth-Moon, circular restricted three-body system.

The structure of the thesis is as follows: Chapter 1 overviews the problem, summarizes other research efforts in cislunar navigation, and introduces the concepts of the current work. Chapter 2 gives an overview of the relevant models and concepts employed by the research presented. Chapter 3 goes into detail on how the simulation works, Chapter 4 discusses the results of the simulations, and Chapter 5 draws conclusions for from the results and presents ideas for future research in this area.

1.1 Problem Definition

Traditional methods of orbit determination used by spacecraft in orbit around Earth take advantage of the extensive ground and space based infrastructure currently in operation and benefit from Earth's known physical features and predictable dynamical environment. This renders many of the techniques unsuitable for trajectories and orbits in regimes beyond GEO, as there lacks an infrastructure to support spacecraft in this region and many of the Earth's features become impractical to use. Historically, deep space and cislunar missions have relied on dead reckoning with inertial navigation sensors and up-linked inertial state updates from radiometric tracking by the DSN [12, 14, 15]. As more deep space missions are launched for military, science and exploration purposes, the demand for support from the DSN will eventually overwhelm the network [13, 15, 16]. Additionally, while relying on the DSN for guidance and navigation is a proven heritage method, it is not resilient against major failures

such as those caused by natural disasters, jamming interference, or strategic attacks from adversarial entities. Adopting autonomous techniques as the primary method of navigating can also contribute to lower mission operating costs, as continuous ground support and regular contact with mission control may not be required [17]. Additionally, autonomous navigation and other guidance, navigation, and control (GNC) functions are required on the upcoming Artemis human spaceflight missions to ensure the safety of the astronauts [18]. In the case of periodic orbits about the collinear equilibrium points (L_1, L_2, and L_3), the dynamics are highly unstable and require precise position and velocity knowledge in order to execute corrective maneuvers to remain approximately on the reference trajectory. Furthermore, other application cases such as entry descent & landing (EDL), and interplanetary trajectories also require high accuracy navigation. There have been numerous proposals of methods for autonomous cislunar navigation summarized in section 1.2.2. However, many are not truly autonomous in the sense that they rely on external sources of information, such as ground-based resources or other satellites to provide measurement updates. Other methods may not yet be practical due to a lag in current technology, and others pose valid solutions for certain mission scopes. Because each method has limitations, it is important to explore all possible methods for improvements in performance and applicability in different scenarios.

1.2 Review of Spacecraft Navigation Methods

1.2.1 Navigation Methods for Earth Orbit

Traditional methods of orbit determination used by spacecraft in orbit around Earth become less viable options for spacecraft navigation on missions beyond Geosynchronous Earth Or-

bit (GEO). Signals from Global Navigation Satellite System (GNSS) constellations such as Global Positioning System (GPS) are too weak beyond GEO [12, 17, 19]. Other traditional orbit determination methods used on spacecraft in Earth orbit take advantage of the existing vast space infrastructure on and around Earth for telemetry updates and commands. Spacecraft in close proximity to Earth benefit from having access to more telecommunication ground stations such as the Near Space Network (NSN), which operate at shorter ranges than the DSN. Earth is also home to a number of ground-based radio and optical sensor networks such as the International Laser Ranging Service (ILRS) global tracking network [20], the French Doppler Orbitography and Radiopositioning Integrated by Satellite (DORIS) system [17], the US Space Surveillance Network (SSN), and many other commercially available systems that are used for tracking space objects [15, 21]. There are also space based observation networks such as the Space Based Space Surveillance System (SBSS) and the Geosynchronous Space Situational Awareness Program (GSSAP) dedicated to tracking spacecraft [16]. Earth Orbits provide more opportunity for access to other spacecraft and constellations such as the Tracking and Data Relay Satellite System (TDRSS) which can be leveraged for satellite-to-satellite measurements [17]. A common concern with current conventional object tracking methods is they are insufficient in effectively monitoring and serving the regions beyond GEO [7, 11].

Alternative orbit determination methods for Earth orbits depend on accurate attitude determination. Directional measurements to celestial bodies via attitude sensors are coupled with measurements of Earth's magnetic field. Together, these can be used to estimate spacecraft position and velocity [17, 22, 23]. It has also been shown that optical measurements of natural landmarks on Earth can be used for orbit determination [17, 24]. The dynamical environment in near Earth orbits can be leveraged for orbit determination. Observations of perturbations in Earth's gravity field [17, 14] and acceleration disturbances from solar

radiation pressure [17] have been proposed in limited capacities.

1.2.2 Navigation Methods for xGEO

The United States first started sending spacecraft to explore the Moon in the late 1950s, coinciding with the construction of NASA's Pioneer Deep Space Station in 1958 [25]. The original facility of what is now the Goldstone Deep Space Communications Complex, is one of three that make up the Deep Space Network (DSN) [25]. Every deep space robotic mission since has relied on the DSN to provide tracking and communications support throughout the spacecraft's lifetime to prevent drifting of onboard inertial navigation sensors. There have been many proposed ideas for new methods of navigating in xGEO, some of which are autonomous to eliminate reliance on the external updates and improve mission performance.

Linked, Autonomous, Interplanetary Satellite Orbit Navigation (LIASON) takes advantage of the two-axis asymmetrical acceleration field that exists around the collinear libration points, L_1 and L_2 [17]. Because each periodic orbit about these points is locally unique, there is only one possible orientation for each orbit size and shape. This enables relative crosslink measurements between two or more spacecraft to be used for determining the absolute orbit and position of spacecraft within the orbit [26, 27]. The Cislunar Autonomous Positioning System (CAPS) is a commercialized product which applies the concept of LIASON to a Near Rectilinear Halo Orbit (NHRO), which has been implemented on a CubeSat mission, Cislunar Autonomous Positioning System Technology and Navigation Experiment (CAPSTONE) [28]. Leveraging the asymmetry of the gravitational field in which the NHRO exists, CAPSTONE is able to determine its absolute position and velocity from relative range and range rate measurements of the Lunar Reconnaissance Orbit (LRO) [29].

The StarNAV concept proposes the use of stellar observations for autonomous navigation.

Apparent shift in wavelength and direction from the spacecraft to guide stars can be used to directly estimate inertial velocity [30]. Changes in these observable parameters are mostly driven by changes in spacecraft states relative to the light sources. However, current limitations in sensing technology inhibit the practical use of this concept [30].

Spacecraft laser ranging is a technique that has been used since the mid 1960s and still provides tracking services for several missions in operation around the Earth and Moon [20]. Position of spacecraft equipped with laser retroreflectors are able to be accurately measured from laser pulses emitted from the ILRS network. Range is calculated from the time delay between when the pulse is sent and when the reflected pulse is received at the ground station [20]. Most recently, it was announced that the European Space Agency's (ESA) Lunar Pathfinder spacecraft will use laser ranging from Earth for positioning updates in addition to radio ranging and leveraging Galileo and GPS signals during operation in its highly elliptical, Frozen Lunar Orbit [31]. This mission is part of ESA's Moonlight initiative which seeks to establish a network of communications and navigation spacecraft around the Moon to serve as support infrastructure for future missions and lunar operations [31, 32]. It is not yet clear if this network will be able to provide spacecraft in libration point orbits and trans-lunar trajectories with navigation and communications services as most of the publicly available work has focused on entry, decent, and landing, lunar surface, and lunar orbit operations.

Methods using celestial X-ray sources such as pulsars have been presented for both attitude and translation state determination. The stable rotation and regular periodic emission of X-ray pulses enables spacecraft to estimate velocity by measuring relative Doppler shift of pulsar X-ray sources [33, 34]. Position can be estimated using a combination of an accurate *a priori* estimate, directional measurements to a pulsar and a planetary body, and the apparent diameter of the planetary body if absolute position of the planetary body is known [33].

Alternatively, relative position to a planetary body can be determined by observing pulsar occultations with the planetary body [33]. If the spacecraft starts with accurate position knowledge, a third way of determining position is by recording the time of arrival of received X-ray pulses to get changes in range relative to the pulsar [33, 34]. In theory, because pulsars exist at astronomical distances, they provide a good option for navigating long distances within the solar system. However in practice, using X-ray pulsars for navigation is challenging and may require further technology and algorithm development before wide scale usage for cislunar navigation [33].

Work done by Yim, Crassidis, and Junkins in [19] shows that if attitude is known, autonomous navigation is possible using Doppler shift from sunlight, and directional measurements from the spacecraft to the sun and Earth. Other work, detailed in Christian and Lightsey 2009, also makes use of natural targets for relative directional and range measurements. For example, directional measurements to known planetary bodies via horizon observations or angular measurement to the estimated centroid can be complimented by apparent diameter measurements from optical sensors [12]. Optical methods involving natural targets require accurate position and velocity knowledge of the targets which is only available for some of the potential measurement targets. Additionally, optical methods may suffer from poor visibility or lighting conditions depending on the spacecraft trajectory relative to viable targets and nearby light sources. The Orion capsule also uses a centroid finding method to determine range and bearing angle from processed images of the Earth and Moon [35]. Other optical methods use angular measurements between reference stars and either a known landmark on planetary body, or the horizon of the planetary body [12]. Previous exploration missions, MESSENGER and Mariner 9, used radiometric tracking combined with angular measurements between reference stars and their target body extracted from images using onboard cameras [12, 36, 37]. Image processing is computationally expensive and in

the case of MESSENGER and Mariner 9, this was done by ground control teams [12, 36, 37]. Altimeter range measurements are also discussed in [12] however this technique requires a spacecraft to be in close proximity of a target body and is not suitable for most of cislunar space.

Time-of-passage measurements of stars as they pass behind planetary bodies has been proposed for navigation for both Earth and Lunar Orbits [38]. While stellar occultation observations can be feasible for navigation in orbits close to primary bodies, this method is not viable for trans-lunar trajectories due to the lack of observable occultations when the spacecraft is far from planetary bodies [39]. It is anticipated that using stellar occultations for libration point orbits will suffer from the same geometric lack of available measurements. Libration points are far from the primary bodies in a three-body system and do not move significantly relative to the primaries. This means that the driving factor behind the motion of stars passing behind either of the two primary bodies is the rotation of the three-body system. The rate at which the system rotates is unlikely to be fast enough to generate sufficient measurement opportunities for the spacecraft to estimate its position and velocity.

Other commercially proposed concepts include Inverted PNT (iPNT) from Aerospace Corporation [40] and Jervis Autonomous Module (JAM) from Rhea Space Activity (RSA) [41]. A similar concept to the current work was proposed in [42] for navigation in Earth orbits, but did not consider trajectories in cislunar space.

Despite many of the hurtles currently limiting many of the proposed navigation strategies, some show potential and may be applicable for cislunar space. However, it is important to have multiple viable options available as some methods may not be ideal for certain trajectories or conducive to the overall mission architecture. There is a need for more feasible autonomous navigation methods that are suitable for cislunar space. Furthermore, autonomous navigation methods are desired in the case of human spaceflight to provide an

added level of safety and assurance that the crew will not be lost in space if something goes wrong.

1.3 Current Work

The goal of this research is to propose and analyze a new cislunar navigation method that is fully autonomous and self contained, meaning that it does not require future lunar space or ground based infrastructure development. This can be done via laser ranging to the five lunar ranging retroreflectors (LRRR) on the Moon's surface (shown in Figure 1.1) from the Lunar Laser Ranging Experiment (LLRE), which began in the late 1960s [43]. Installed on the Moon during the United State's Apollo and Soviet Union's Luna program (see Figure 1.2), the LRRRs are designed to reflect laser pulses sent from Earth ground stations. Each LRRR is an array of corner cube reflectors which reflect radiation back in the direction of the source, at the same angle of incidence. Distance from a station to a reflector is found from the elapsed time between when a laser pulse sent from a ground station to one of the retroreflectors, and when the reflected signal is received back at the ground station.

This same concept can be flipped and applied to track a spacecraft in cislunar space. Here, the spacecraft performs the role of the ground station, and the objective becomes determining the distance from the spacecraft relative to the Moon rather than the distance of the Moon relative to the Earth. It is assumed that the spacecraft attitude is accurately known and controllable such that it has the ability to point itself toward each of the retroreflectors. Precise range measurements from laser pulse time-of-flight are passed into an Extended Kalman Filter (EKF) to update the spacecraft's estimated position and velocity. Since the Moon's position and velocity are known, as well as the coordinates of the retroreflectors on the Moon's surface, the absolute position of the spacecraft can be estimated from determining

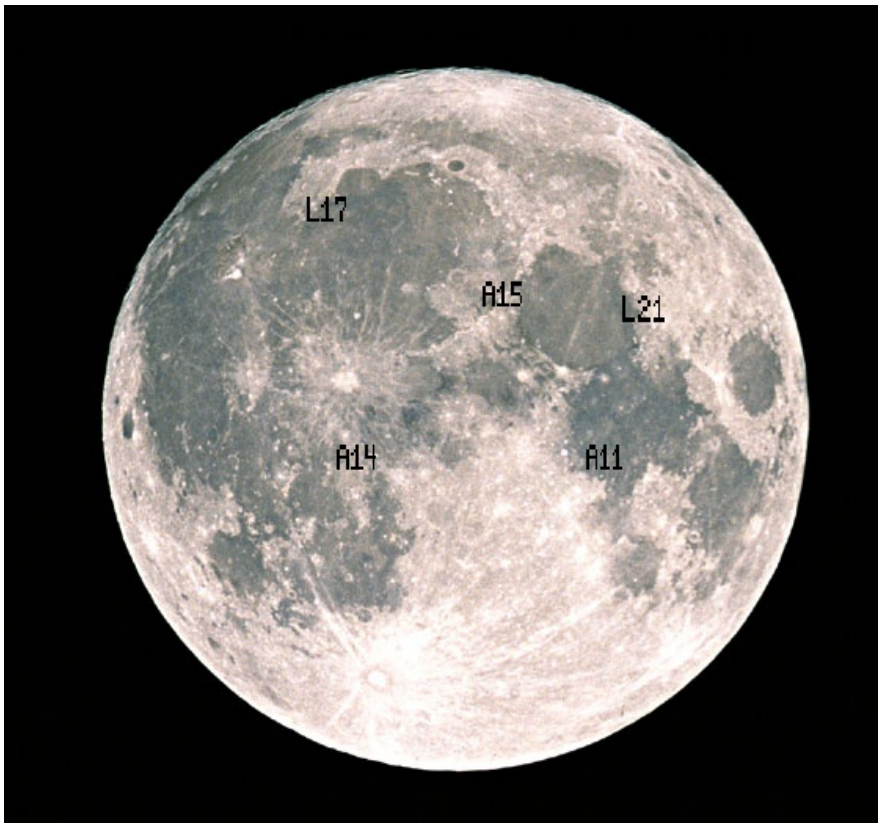

Figure 1.1: Locations of Apollo (A) and Lunokhod (L) LRRR on Lunar Surface, courtesy of [1].

the relative distance to one or more LRRR. An illustration of this concept is shown in Figure 1.3 where red circle is the current position of the spacecraft in its halo orbit (blue trajectory) about L_1 (red "X") as it sends a laser pulse (dashed green line) to one of the five LRRR, depicted by the pink squares on the Moon's surface.

The baseline case study for this navigation method will be a periodic halo orbit about libration point, L_1 in the Earth-Moon circular restricted three-body problem. Of all the families of periodic orbits, Lissajous, distant retrograde orbit (DRO), near-rectilinear halo orbit (NRHO), and halo orbits have been historically some of the most useful for various mission objectives. A L_1 halo was chosen in particular because it exists between the Earth and Moon in the Earth-Moon three-body system, and it offers continuous access to the near

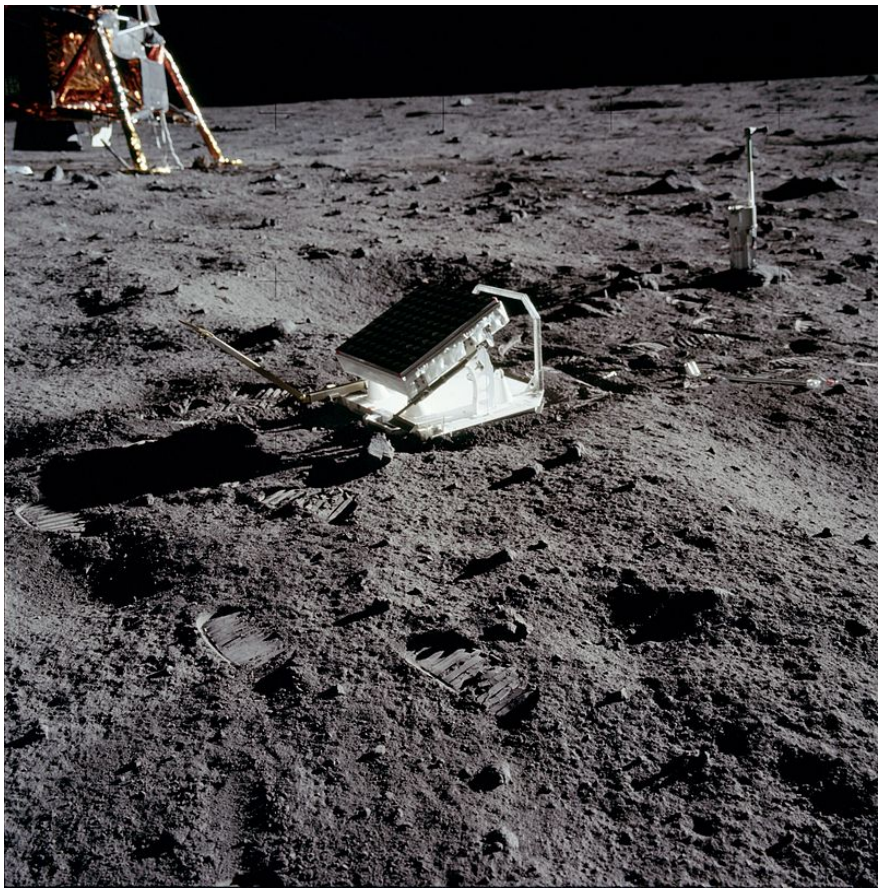

Figure 1.2: LRRR in front of LM-5 placed during Apollo 11, courtesy of [2].

side of the Moon and all five LRRR. This is because the Moon is tidally locked with the Earth, meaning that the Moon rotates about its axis at approximately the same rate as the Moon revolves around the Earth.

Initial Conditions for the baseline case are given in Table 1.1. Note that only non-zero states of the initial conditions will be listed. For the remainder of this thesis, it is implied that components of the initial state vector are zero if not otherwise specified.

Table 1.1: Non-dimensional initial condition for baseline halo orbit.

x_0 (DU)	z_0 (DU)	$\dot{y}_0$ (DU/TU)
0.823423184431389	0.029981078411693	0.140541278691750

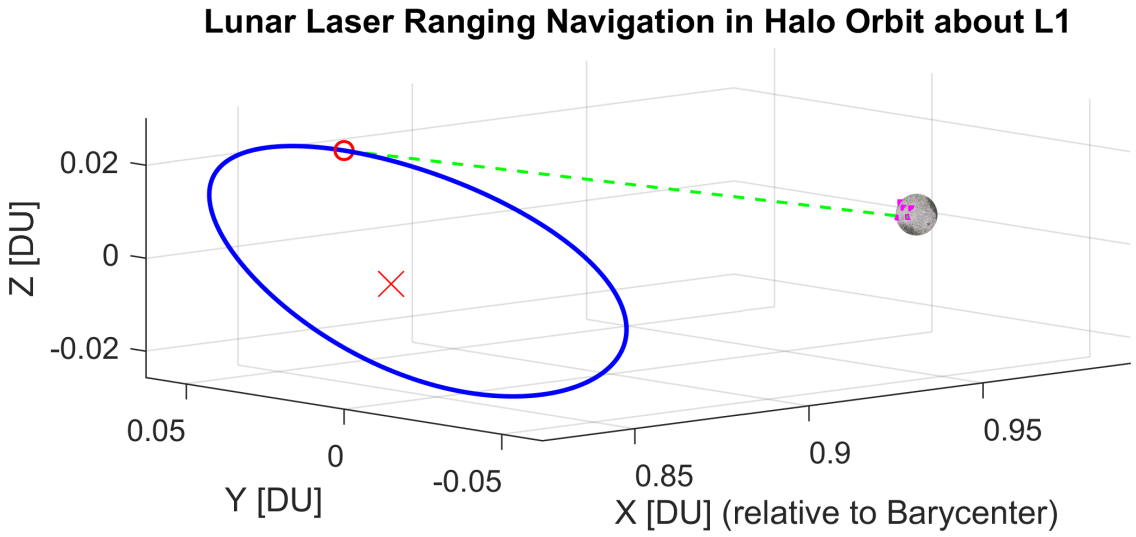

Figure 1.3: Diagram of proposed the navigation method.

The laser ranging ground stations typically used with LRRRs are equipped with powerful lasers, telescopes, and sensitive photon detecting sensors such as avalanche photodiodes and photomultipliers [43, 44]. Given that the focus of this research is navigation and not optics or hardware design, for the purposes of presenting this concept, it is assumed that the instrumentation and technology required to conduct laser ranging to the Moon exists and is scalable such that it can be packaged on a spacecraft. The region around L_1 offers improved conditions for laser ranging to the Moon compared to Earth's surface. The distance to the LRRR is significantly closer and measurements are not subject to interference from weather conditions, atmospheric effects, or light pollution. This reduces the round trip time of the laser pulse and eliminates major sources of noise in measurements from ground stations. However, a new challenge is presented because the spacecraft moves in its orbit during the measurement process. Similar to the relative motion between the ground station on Earth and the LRRR on the Moon due to planetary motion, the photon sensor on the spacecraft is at a different point in space from when the laser pulse was sent. In both cases, this is mitigated by laser beam divergence as the pulse travels to the retroreflector and back to the sensor. The amount that the receiver moves in space from the time the pulse was sent, still

falls within the cross sectional area of the beam projected along the direction of the reflected pulse at the distance of the photon sensor. This means that the sensor will still be able to detect the returned laser pulse. The geometry of this problem will be further discussed in Section 2.2.2.

The advantages that this method offers is that it works on a single spacecraft, uses existing lunar infrastructure, does not rely on ground station updates nor other spacecraft during its mode of normal operation, and grants continuous access to make measurements for cislunar spacecraft. In comparison to methods previously discussed, often times geometry of relative motion and visibility of target objects can have large impact on performance of state estimation from optical methods. Additionally, some optical methods use image processing which can be very expensive and requires a lot of onboard computing power. Proposed solutions involving satellite-to-satellite tracking are still limited in that they depend on other spacecraft for measurement updates. In the current state of cislunar and lunar infrastructure and satellite population, this method lacks redundant measurement opportunities and carries the risk of encountering periods of insufficient access to the few available spacecraft. This has the potential to degrade state estimation and interfere with trajectory correction maneuvers. For example, CAPSTONE requires active cooperation from LRO, and CAPSTONE has access to LRO for less than 6% of its orbit [29].

1.3.1 Assumptions

Some of the assumptions baked into this preliminary exploration of a new navigation concept are as follows:

- The spacecraft will rely on the DSN or other long-range, Earth-based tracking service during transit from Earth to L_1 until it arrives at its libration point orbit (LPO). The

spacecraft's laser ranging navigation system will then take over.

- It is assumed that the spacecraft is able to determine its attitude accurately, onboard actuators have full control over its orientation, and the GNC, ADCS systems can provide sufficient pointing accuracy.
- For the purposes of analyzing navigation by spacecraft laser ranging to LRRR, it is assumed that the necessary hardware, sensors, and technology exist and are feasible to be implemented on a spacecraft.
- Spacecraft instrumentation is capable transmitting lasers with sufficient beam divergence to satisfy the geometry of the proposed laser ranging measurement.
- The laser pulse reflected by a LRRR is detectable by the spacecraft despite any losses of transmitted power/intensity caused by beam divergence, reflector efficiency, or distance traveled.
- The spacecraft and relevant supporting sub-systems are capable of supplying all of the required power, computational capabilities, and other resources needed to make measurements and run estimation algorithms.
- The simulation and analysis of this concept is conducted in the circular restricted three-body problem.

Chapter 2

Background

2.1 The Circular Restricted Three-Body Problem

The circular restricted Three-Body Problem is a simplified dynamics model used to represent motion of a third body with negligible mass in the vicinity of two massive primary bodies in circular orbits about their mutual center of mass. The two primaries, or primary and secondary masses, orbit about the system's barycenter at a constant rate and dominate the gravitational field and forces from all other bodies are neglected [7]. This is particularly useful for modeling the motion of spacecraft that is subjected to influences from both primary bodies such as translunar trajectories, lunar orbits, libration point orbits, orbiting about binary asteroid systems, etc.

The CR3BP is most commonly defined in a rotating frame of reference known as the Synodic frame, centered at the system barycenter depicted in figure 2.1. The x axis of Earth-Moon Synodic frame is defined by the direction from the center of the Earth to the Moon's center of mass. The z axis is angular momentum vector of the Moon and Earth rotating about the barycenter, normal to the orbital plane [45, 46]. Lastly, the y axis completes the right handed triad. This frame rotates with the primaries as they orbit the barycenter which provides a unique vantage point of the dynamics that occur from the interactions of both primaries with the third body. The primaries in the rotating frame appear stationary as the frame moves with the bodies. However, if viewed in an inertial frame, the primary bodies

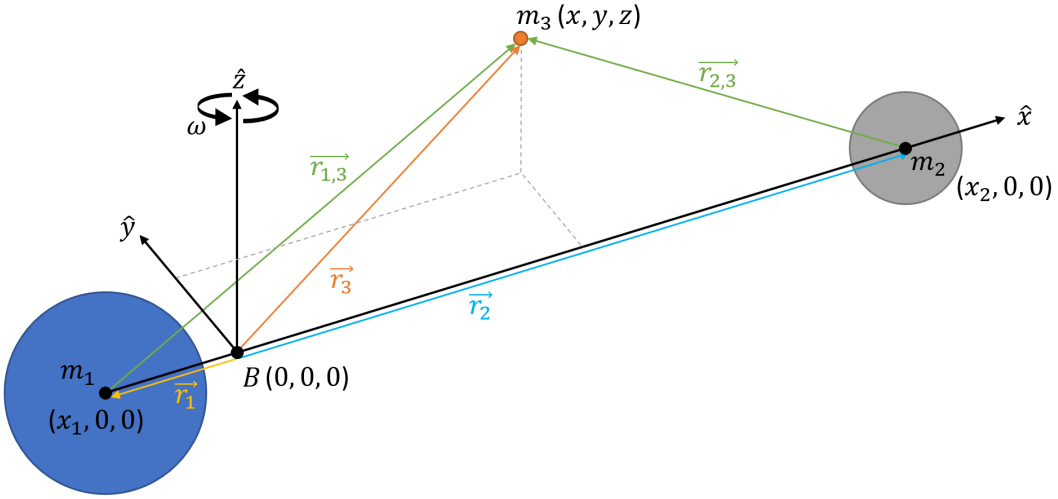

Figure 2.1: Circular Restricted Three-Body Problem Diagram (angles are to scale, but relative distances and sizes are not).

would appear to rotate about the system barycenter in circular orbits, while the distance between them remains constant [47]. Additionally, because the Moon's orbit is inclined, the Earth and Moon will appear to oscillate in the z direction in an inertial frame, similar to a playground seesaw or teeter-totter with the barycenter as the pivot point. Figure 2.2 illustrates the Earth-Moon geometry in context of the CR3BP.

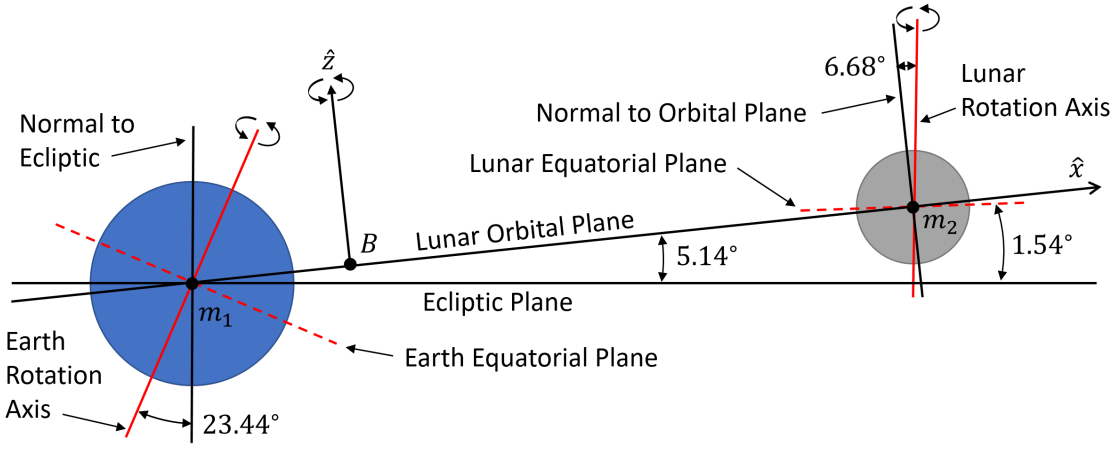

Figure 2.2: Two-dimensional $x-z$ plane projection of the CR3BP and Earth-Moon Geometry (angles are to scale, but relative distances and sizes are not).

The assumptions underpinning the CR3BP are:

- The mass of the third body is infinitesimally small compared to the mass of the primaries such that it has no affect on the motion of the two primary bodies ($m_1 > m_2 \gg m_3$).
- The primary and secondary bodies have Keplerian, circular orbits about the mutual center of mass, such that the distance between the centers of mass of the primaries remains constant.
- Both bodies are spherically symmetric and gravity is the only significant force.

Let subscripts 1,2,3 represent quantities corresponding to the Earth, Moon, and spacecraft, respectively. Note, these equations are general such that any other three-body system can be represented for example the Sun-Earth or Sun-Jupiter systems.

The scalar mean angular velocity of the primary and secondary masses about the barycenter is given as [47]:

$$\omega = \sqrt{\frac{G(m_1 + m_2)}{||\boldsymbol{r}_{12}||_2^3}} \tag{2.1}$$

where ω is counter-clockwise about the z axis of the S frame, G is the universal gravitational constant, and m is mass. $\boldsymbol{r}_{12} = \boldsymbol{r}_2 - \boldsymbol{r}_1$ denotes the relative position vector from Earth to the Moon. The state, position and velocity vectors are defined as:

$$\boldsymbol{X} = \begin{bmatrix} \boldsymbol{r} & \boldsymbol{v} \end{bmatrix}^T \tag{2.2}$$

$$\boldsymbol{r} = \begin{bmatrix} x & y & z \end{bmatrix}^T \tag{2.3}$$

$$\boldsymbol{v} = \begin{bmatrix} v_x & v_y & v_z \end{bmatrix}^T = \dot{\boldsymbol{r}} = \begin{bmatrix} \dot{x} & \dot{y} & \dot{z} \end{bmatrix}^T \tag{2.4}$$

The orbital period of the Earth-Moon system is given by [47]:

$$\begin{aligned} T &= \frac{2\pi}{\omega} \\ T &= 2\pi\sqrt{\frac{||\boldsymbol{r}_{12}||_2^3}{G(m_1+m_2)}} \end{aligned} \tag{2.5}$$

The motion of a spacecraft in the CR3BP is governed by the following equations of motion [48]:

$$\ddot{\boldsymbol{r}}_3 = \frac{-Gm_1\boldsymbol{r}_{13}}{||\boldsymbol{r}_{13}||_2^3} + \frac{-Gm_2\boldsymbol{r}_{23}}{||\boldsymbol{r}_{23}||_2^3} \tag{2.6}$$

Equation 2.6 is often non-dimensionalized by physical properties of the three-body system. The characteristic quantities for mass, length, and time represent the combined mass of the primaries, the distance between the primaries' centers of mass, and the period of the system rotating about the barycenter, respectively. The values of these quantities are accurately calculated from JPL ephemeris and are available on the JPL Three-Body Periodic Orbit Catalog and Horizons System maintained by the Solar System Dynamics group [5]. The characteristic parameters for the Earth-Moon system are given in Table 2.1.

Table 2.1: Normalizing parameters of the Earth-Moon CR3BP system, adopted from [5].

Earth-Moon System	
Mass Parameter, μ	$1.215\,058\,560\,962\,404 \times 10^{-2}$
Characteristic Length, L^*	389 703 km
Characteristic Time, t^*	382 981 s
Characteristic Mass, m^*	6.0456×10^{24} kg

The formulas behind the pre-computed values given in Table 2.1 are as follows [6, 48]:

$$\begin{aligned} m^* &= m_1 + m_2 \\ L^* &= ||\boldsymbol{r}_2 - \boldsymbol{r}_1||_2 \\ t^* &= \sqrt{\frac{(L^*)^3}{Gm^*}} \end{aligned} \tag{2.7}$$

Dividing these characteristic quantities into the dimensional parameters, position, velocity, etc. yields non-dimensional quantities with distance units, DU and time units, TU, or some combination of them. This unit transformation is done to generalize the problem and allows for more accurate numerical integration. In the dimensional version of the equations (km and km/s for position an velocity respectively), the relative magnitude of the position compared to the velocities is large, which creates non-uniformity in accuracy across the states. Additionally, non-dimensionalizing simplifies the equations of motion where the synodic period becomes 2π, and the universal gravitation constant, distance between the primaries, and angular rate of the system, all become unity [49, 50].

The non-dimensional mass quantities are handled by introducing a mass parameter, μ [48, 49]:

$$\begin{aligned} \mu &= \frac{m_2}{m^*} = \frac{1}{\frac{m_1}{m_2} + 1} \\ 1 - \mu &= \frac{m_1}{m^*} \end{aligned} \tag{2.8}$$

Such that the normalized masses add to one. It is important to note that μ here is a mass ratio and is not to be confused with the standard gravitational parameter, also commonly represented by μ, defined as $\mu = G(m_1 + m_2)$ for the Three-body system. From this point forward, non-dimensional equations will be used although notation has not changed.

The non-dimensional equations of motion of a third body or spacecraft become [6, 7, 48, 51]:

$$\begin{aligned}
\ddot{x} &= -\frac{(1-\mu)(x+\mu)}{r_{13}^3} - \frac{\mu(x-1+\mu)}{r_{23}^3} + x + 2\dot{y} \\
\ddot{y} &= -\frac{(1-\mu)y}{r_{13}^3} - \frac{\mu y}{r_{23}^3} + y - 2\dot{x} \\
\ddot{z} &= -\frac{(1-\mu)z}{r_{13}^3} - \frac{\mu z}{r_{23}^3}
\end{aligned} \tag{2.9}$$

Where the distances from each of the primaries to the spacecraft are defined as:

$$\begin{aligned}
r_{13} &= \sqrt{(x+\mu)^2 + y^2 + z^2} \\
r_{23} &= \sqrt{(x-1+\mu)^2 + y^2 + z^2}
\end{aligned} \tag{2.10}$$

In the dimensional version of the CR3BP, the distances of the primary masses to the barycenter are defined by the distance between the primaries scaled by the ratio of each primary's mass to the mass of the system. Therefore when non-dimensionalizing, the mass parameter becomes a valid way of quantifying distances. Given a set of initial conditions, equations 2.6 and 2.9 can formed into a first order state space model be numerically integrated over time to produce a trajectory in the CR3BP.

2.1.1 Libration Points

The circular restricted three-body problem is unique in that the dynamics of the system create five equilibrium points, commonly known as Lagrange or Libration points and are refered to as L_1, L_2, L_3, L_4, and L_5. The Libration points are only observable in the rotating frame and rotate with the system about the primaries, illustrated in Figure 2.3. If one could place a spacecraft exactly at any of the points, it would be in equilibrium because it would remain permanently stationary relative to the primaries, and no maneuvers would

be required to keep it there (assuming all external disturbances are neglected) [47, 48]. The equilibrium points are a result of the combined gravitational pull of the primaries acting as the centripetal force, balancing out the centrifugal force of the rotating system. This becomes more evident when considering the dimensional Equation 2.6. All equilibrium points lie in the orbital plane of the two primaries and can be split into two groups, collinear points, and triangular points.

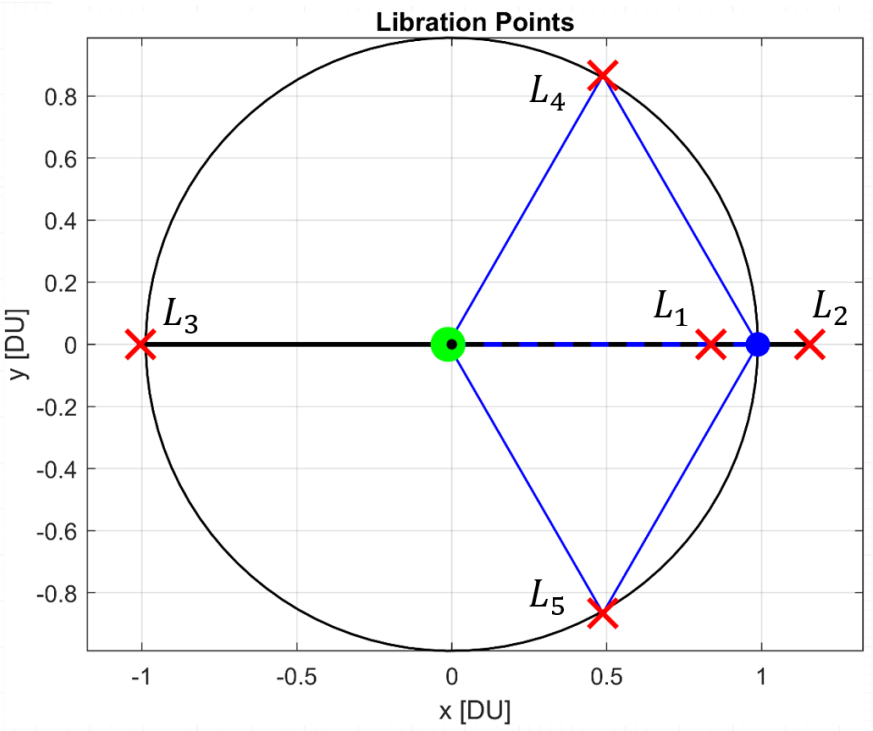

Figure 2.3: Locations of five libration points in synodic frame of the CR3BP. The green dot represents Earth, the black dot is the system barycenter, and the blue dot is the moon. The large black circle represents the moons orbit about the barycenter, the each libration points is marked by a red "x", and the blue triangles help identify the triangular libration points.

The three collinear points, L_1, L_2, L_3 are located along the x axis of the synodic frame and can be calculated from the equations of motion for the third body. Since the points are at equilibrium, and remain stationary in the rotating frame, all of the acceleration and velocity terms are set to zero and there should be no unbalanced forces at the points. If a spacecraft

in the three-body system had a non-zero, z position component, both primaries would exert an unbalanced force on the spacecraft toward the orbital plane. Therefore to z must equal zero. Additionally, this particular set of solutions fall on the x axis so $y = 0$ as well. This yields [6, 52]:

$$0 = -\frac{(1-\mu)(x+\mu)}{r_{13}^3} - \frac{\mu(x-1+\mu)}{r_{23}^3} + x \tag{2.11}$$

This equation can be solved numerically which will return five solutions. To extract the correct values for each libration point, the solutions with imaginary components are associated with the triangular points and can be ignored. The remaining three solutions corresponding to L_1, L_2, and L_3 are given in Table 2.2.

Table 2.2: Pairing non-dimensional numerical solutions for x position to the correct libration point [6] with values from [5].

Libration Point	x Position	
L_1	$-\mu < x < (1-\mu)$	0.836 915 13 DU
L_2	$x > (1-\mu)$	1.155 682 17 DU
L_3	$x < -\mu$	−1.005 062 65 DU

Alternatively, if it's desired to solve directly for each point instead of all three at once, one can manipulate the signs of terms in equation 2.11 associated with the primaries based on the anticipated location of each point, as shown in [6, 48].

The two triangular points, L_4 and L_5, exist at the points of an equilateral triangle where the two primaries make up the other two points with the base running along the x axis, shown by the blue lines in Figure 2.3. These points can be found using geometry [6, 52, 47].

$$\begin{aligned} x &= \frac{1}{2} - \mu \\ y &= \pm\frac{\sqrt{3}}{2} \end{aligned} \tag{2.12}$$

Since L_4 and L_5 are symmetrical over the x axis, they have the same x component and

opposite y components (shown in Fig. 2.6). Where x is the distance half way between the primaries and y is the offset from the x axis, equivalent to the height of a equilateral triangle with sides equal to one, or the second leg of a right triangle with hypotenuse equal to one and first leg equal to one half.

Table 2.3: Triangular Lagrange point locations given by [5].

Libration Point	x Position	y Position
L_4	0.487 849 41 DU	0.866 025 4 DU
L_5	0.487 849 41 DU	−0.866 025 4 DU

2.1.2 Periodic Orbits

Periodic motion is a highly sought after attribute of the CR3BP where trajectories can be designed to have repeating patterns or periodic orbits about libration points. Visualized in the rotating frame, these orbits can either retrace their orbit regularly (periodic) or follow a path that remains in the vicinity of the libration point but doesn't necessarily follow a repeating path (quasi-periodic). Formally, if a trajectory about a libration point intersects the $x-z$ plane perpendicularly, such that x and z components of velocity are zero when $y = 0$ ($v_y \neq 0$, $v_x = v_z = y = 0$), the orbit is periodic [48, 53]. This is illustrated in Figure 2.4, where the red halo trajectory crosses the light blue highlighted section of the $x-z$ plane perpendicularly.

Additionally, if a trajectory intersects the x axis perpendicularly, such that the x component of velocity is zero when $y = 0$ ($v_y, v_z \neq 0$, $v_x = y = 0$), the orbit is also periodic [53]. This can also be visualized with Figure 2.4, where the black line is the x axis projected onto the crossing point. If this was the actual x axis, the second condition for periodic motion would also be satisfied because the axis is crossed perpendicularly. Periodic orbits can have motion in the $y-z$ plane when crossing the x axis ($v_z, v_y \neq 0$ when $v_x = y = 0$) as long as there is

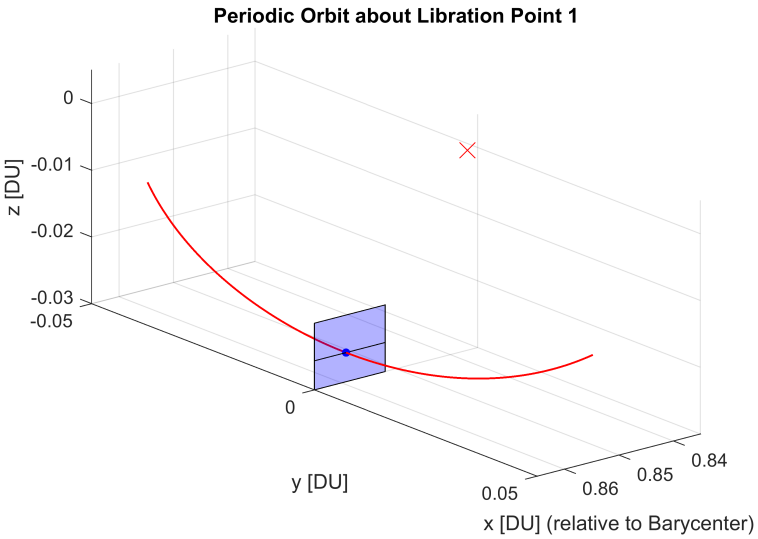

Figure 2.4: Example of a L_1 halo periodic condition.

no component of velocity along the x direction. There are many different types of behaviors of periodic and quasi-periodic motion which have been grouped into "families" of orbits. Orbits within the same family typically have similar dynamical behavior, orientation, and shape, but may differ in size and orbital period. For example, a few orbits from the planar Lyapunov and northern halo families are plotted in figure 2.5. It is common for specific periodic orbits to be identified by parameters such as period, Jacobi constant, or initial conditions (typically x or z). Periodicity occurs when the frequency of an orbit's oscillatory in plane (x and y directions) and out of plane motion (z direction) are equal. This is evident in the case of halo orbits. Periodicity can also occur if the out of plane frequency is zero, as seen in Lyapunov orbits. Quasi-periodicity occurs when the in plane and out of plane frequencies do not match as seen in Lissajous orbits [17, 52].

The underlying cause of the periodic and oscillatory motion experienced by third bodies in the system is the symmetry in the gravitational field. The acceleration due to gravity of the two primaries is symmetric in the y and z directions while asymmetric in the x direction [17]. In the case of some orbit families halo, butterfly, dragonfly, with out of plane motion, the

symmetry allows for a complimentary set of orbits mirrored across the lunar orbital or $x-y$ plane. To distinguish between the two sets, the orbits which have initial conditions above the $x-y$ plane ($+z$ direction) are denoted "northern" and the orbits with initial conditions below the $x-y$ plane (-z direction) are called "southern" [5, 17].

While libration points are points of equilibrium, the space surrounding the collinear points is dynamically unstable. Similar to the inverted pendulum problem, any deviation from the exact libration point location due to perturbing forces will cause a spacecraft to rapidly drift from equilibrium. The same goes for orbits around these points, if a spacecraft does not regularly execute trajectory correction maneuvers (TCM) to maintain its orbit, it will exponentially diverge from its periodic orbit [17, 52]. On the contrary, L_4 and L_5 are marginally stable if the mass ratio of m_1/m_2 is greater than 24.96 or the mass parameter is less than 0.03852 [47, 54]. A spacecraft orbiting in the vicinity of these points will tend to converge at the equilibrium location. An intuitive way to visualize the libration points and their dynamical stability is by looking at curves of zero velocity in the orbital plane, shown in figure 2.6.

Points along the curves, illustrated in figure 2.6, have the same value Jacobi constant when velocity is set to zero [52]. The Jacobi constant, C has a number of implications about the three-body system. It is computed by evaluating the time integral of the dot product of the velocity and acceleration vectors of the third body [48]. This yields the Jacobi integral equation [48, 53, 54, 55]:

$$C = 2U - (\dot{x}^2 + \dot{y}^2 + \dot{z}^2) \tag{2.13}$$

Where U is the pseudo-potential function [6, 48, 50, 54, 55]:

$$U = \frac{(1-\mu)}{r_1 3} + \frac{\mu}{r_2 3} + \frac{1}{2}(x^2 + y^2) \tag{2.14}$$

This constant of integration is used as a measure of energy, such that it is negatively proportional to the actual amount of energy associated with the third body [48, 49, 52, 54]. In figure 2.6, the contour lines of Jacobi constant form a saddle point as the collinear points are approached. It is also shown that the triangle libration points lie in a valley or a region of relatively lower Jacobi constant values. Saddle points have a stable and unstable direction where perturbations in the unstable direction cause a rapid divergence from the equilibrium point. The triangular points act as a sink where perturbations decay to zero and remain at the equilibrium point. In reality however, the L_4 and L_5 libration points are not truly stable. Gravitational disturbances from the Sun require spacecraft orbiting about these points to make TCMs in order to maintain their trajectory [47].

2.1.3 Bifurcation Points & Monodromy Matrix

Families of periodic orbits in the three-body problem are all connected such that they branch off each other. Specific locations where new families of solutions intersect are called bifurcation points and can be found numerically by analyzing eigenvalues of the state transition matrix. The state transition matrix, Φ, is a linear mapping between state vectors at two

different arbitrary points in time, t_1 and t_2.

$$\begin{aligned}
\Phi(t_2,t_1) &= \begin{bmatrix} \Phi_{\boldsymbol{rr}}(t_2,t_1) & \Phi_{\boldsymbol{rv}}(t_2,t_1) \\ \Phi_{\boldsymbol{vr}}(t_2,t_1) & \Phi_{\boldsymbol{vv}}(t_2,t_1) \end{bmatrix} \\
&= \begin{bmatrix} \frac{\partial \boldsymbol{r}_2}{\partial \boldsymbol{r}_1} & \frac{\partial \boldsymbol{x}_2}{\partial \boldsymbol{r}_1} \\ \frac{\partial \boldsymbol{r}_2}{\partial \boldsymbol{x}_1} & \frac{\partial \dot{\boldsymbol{x}}_2}{\partial \boldsymbol{x}_1} \end{bmatrix} = \begin{bmatrix} \frac{\partial \boldsymbol{r}_2}{\partial \boldsymbol{r}_1} & \frac{\partial \boldsymbol{v}_2}{\partial \boldsymbol{r}_1} \\ \frac{\partial \boldsymbol{r}_2}{\partial \boldsymbol{v}_1} & \frac{\partial \boldsymbol{v}_2}{\partial \boldsymbol{v}_1} \end{bmatrix} \\
&= \begin{bmatrix}
\frac{\partial x_2}{\partial x_1} & \frac{\partial x_2}{\partial y_1} & \frac{\partial x_2}{\partial z_1} & \frac{\partial x_2}{\partial \dot{x}_1} & \frac{\partial x_2}{\partial \dot{y}_1} & \frac{\partial x_2}{\partial \dot{z}_1} \\
\frac{\partial y_2}{\partial x_1} & \frac{\partial y_2}{\partial y_1} & \frac{\partial y_2}{\partial z_1} & \frac{\partial y_2}{\partial \dot{x}_1} & \frac{\partial y_2}{\partial \dot{y}_1} & \frac{\partial y_2}{\partial \dot{z}_1} \\
\frac{\partial z_2}{\partial x_1} & \frac{\partial z_2}{\partial y_1} & \frac{\partial z_2}{\partial z_1} & \frac{\partial z_2}{\partial \dot{x}_1} & \frac{\partial z_2}{\partial \dot{y}_1} & \frac{\partial z_2}{\partial \dot{z}_1} \\
\frac{\partial \dot{x}_2}{\partial x_1} & \frac{\partial \dot{x}_2}{\partial y_1} & \frac{\partial \dot{x}_2}{\partial z_1} & \frac{\partial \dot{x}_2}{\partial \dot{x}_1} & \frac{\partial \dot{x}_2}{\partial \dot{y}_1} & \frac{\partial \dot{x}_2}{\partial \dot{z}_1} \\
\frac{\partial \dot{y}_2}{\partial x_1} & \frac{\partial \dot{y}_2}{\partial y_1} & \frac{\partial \dot{y}_2}{\partial z_1} & \frac{\partial \dot{y}_2}{\partial \dot{x}_1} & \frac{\partial \dot{y}_2}{\partial \dot{y}_1} & \frac{\partial \dot{y}_2}{\partial \dot{z}_1} \\
\frac{\partial \dot{z}_2}{\partial x_1} & \frac{\partial \dot{z}_2}{\partial y_1} & \frac{\partial \dot{z}_2}{\partial z_1} & \frac{\partial \dot{z}_2}{\partial \dot{x}_1} & \frac{\partial \dot{z}_2}{\partial \dot{y}_1} & \frac{\partial \dot{z}_2}{\partial \dot{z}_1}
\end{bmatrix}
\end{aligned} \tag{2.15}$$

The STM has the following properties:

$$\begin{aligned}
\Phi(t_2,t_0) &= \Phi(t_2,t_1)\Phi(t_1,t_0) \\
\Phi(t_2,t_1) &= \Phi^{-1}(t_1,t_2) \\
\det\big(\Phi(t_2,t_1)\big) &= 0 \\
I_{6\times 6} &= \Phi^{-1}(t_2,t_1)\Phi(t_2,t_1) \\
\Phi(t_1,t_1) &= I_{6\times 6}
\end{aligned} \tag{2.16}$$

Additionally, if t_2 is one orbital period, T, in the future from t_1 ($t_2 = t_1 + T$), the state transition matrix is referred to as a monodromy matrix, $M = \Phi(t_1 + T, t_1)$. The eigenstructure of the monodromy matrix provides information about how the states at t_2 are affected from perturbations or changes in states at t_1 [48]. Eigenvalues indicate the stability of the corresponding eigenvectors which represent the perturbation direction or magnitude of change in

each initial state. The 6×6 matrix has three reciprocal eigenvalue pairs of the form $\lambda_i, \frac{1}{\lambda_i}$, for $i = 1,2,3$ [50]. Typically, one pair will be real values, one pair will be a complex conjugate, and one pair will be unity.

Zero eigenvalues, $\lambda_i = 0$, indicate that the corresponding change in initial conditions results in zero change in the end states. If $\lambda_i = 1$, the change in initial state will be translated to the exact same change in final state. The direction that would put a spacecraft onto the unstable manifold is given by $|\lambda_i| > 1$, where the perturbation in initial state is amplified in the final state after each orbit, eventually causing a divergence from the periodic solution. Similarly, the stable manifold direction is given by $|\lambda_i| < 1$, where the change in initial conditions is diminished each orbit, eventually returning to the unperturbed end conditions. These stable and unstable directions come from the eigenvalue pair with real values. Manifolds are essentially "tubes" in space defined by a collection of trajectories with similar stability behavior. More on manifolds can be found in [56, 57, 58, 59].

If the monodromy matrix is calculated for a periodic solution, one pair of eigenvalues will be unity [53, 55]. The two remaining pairs determine the linear or first-order stability of the periodic orbit [50, 53]. The unity pair of eigenvalues corresponds to change in initial conditions that continues the current orbital family. When a bifurcation point is reached, a second pair of eigenvalues will become unity, corresponding to eigenvectors pointing in the direction of the new orbit family branch.

Bifurcation points can be found by looking at the eigenvalues of the monodromy matrix for multiple periodic orbits across a periodic family. For example, Figure 2.7 shows the eigenvalue pair associated direction of the new orbit family plotted over a portion of the planar Lyapunov family as a function of the x initial condition for each orbit. In this plot, the blue points represent the real component of the eigenvalue pair while the red points represent the imaginary component. The eigenvalue pairs converge to unity at two points,

$x = 0.781\,\text{DU}$ and $x = 0.823\,\text{DU}$, where the real parts become one and the imaginary parts become zero. These two bifurcation points correspond to the bifurcation orbits for the halo and axial families of orbits which branch off of from the planar Lyapunov family. The Monodromy matrix is calculated by numerically integrating equation 2.17 simultaneously with the equations of motion (2.9) over a full period, starting with the $I_{6\times6}$ as the initial condition.

$$\dot{\Phi}(t_2, t_1) = A\Phi(t_2, t_1) \tag{2.17}$$

Where A is the jacobian matrix of the time derivitive of the spacecraft states with respect to the spacecraft states:

$$A = \frac{\partial \dot{\boldsymbol{X}}}{\partial \boldsymbol{X}} = \begin{bmatrix} \frac{\partial \dot{\boldsymbol{r}}}{\partial \boldsymbol{r}} & \frac{\partial \dot{\boldsymbol{r}}}{\partial \boldsymbol{v}} \\ \frac{\partial \dot{\boldsymbol{v}}}{\partial \boldsymbol{r}} & \frac{\partial \dot{\boldsymbol{v}}}{\partial \boldsymbol{v}} \end{bmatrix} = \begin{bmatrix} 0_{3\times3} & I_{3\times3} \\ U_{rr} & 2\Omega \end{bmatrix} \tag{2.18}$$

$U_{\boldsymbol{rr}}$ is a matrix of second partial derivatives of the pseudo potential function (Eqn. 2.14) with respect to the spacecraft position vector [6, 48, 55]:

$$U_{\boldsymbol{rr}} = \frac{\partial \dot{\boldsymbol{v}}}{\partial \boldsymbol{r}} = \begin{bmatrix} \frac{\partial^2 U}{\partial x^2} & \frac{\partial^2 U}{\partial x \partial y} & \frac{\partial^2 U}{\partial x \partial z} \\ \frac{\partial^2 U}{\partial y \partial x} & \frac{\partial^2 U}{\partial y^2} & \frac{\partial^2 U}{\partial y \partial z} \\ \frac{\partial^2 U}{\partial z \partial x} & \frac{\partial^2 U}{\partial z \partial y} & \frac{\partial^2 U}{\partial y \partial z^2} \end{bmatrix} \tag{2.19}$$

Ω is a matrix resulting from the Jacobian Equation 2.9 with respect to the spacecraft states, where the only non-zero elements are the non-dimensional rotation rate, ω, of the three-body system:

$$\Omega = \frac{\partial \dot{\boldsymbol{v}}}{\partial \boldsymbol{v}} = \begin{bmatrix} 0 & 1 & 0 \\ -1 & 0 & 0 \\ 0 & 0 & 0 \end{bmatrix} \tag{2.20}$$

2.2 Lunar Laser Ranging Experiment

The Lunar Laser Ranging Experiment was formulated in the late 1950s to precisely study the dynamics of the Moon by regularly calculating the distance to the five LRRR at specific locations on the lunar surface, shown in Figure 1.1. Individual LRRR are designated by the mission that they were installed on (e.g. Apollo 11 or A11). The calculation is done by measuring round trip time of laser pulses from Earth to a LRRR, and back to the Laser ranging station. Since the speed of light is known and the time is measured, distance can be accurately found. The objectives of the experiment were to generate accurate ephemeris for the lunar orbit, determine the lunar center of mass, study the Moon's physical librations (the apparent "wobble" of the Moon), and test physics theories [43]. Several laser ranging stations (see Figure 2.8) across the world have used LRRR measurement data for various scientific endeavors and have achieved range accuracies at the sub centimeter level [60]. Each LRRR consists of a hundred or more solid fused silica corner reflectors arranged in a two dimensional grid, shown in Figure 2.9 [43, 60]. The reflectors are 3.8 cm in diameter and are designed to reflect light back to where the transmitted incident rays originated [43, 60, 44]. The retroreflectors are passive devices, and are still operational, used by many countries in present-day.

2.2.1 Lunar Coordinate Frames

There are two main body-fixed selenographic or Moon centered coordinate systems that are used on the Moon with origins at the lunar center of mass. These coordinate systems are used to map the Moon's geography and identify locations on the lunar surface. The Mean Earth/Mean Polar Axis (MER or ME) is defined by the mean direction to Earth and the mean rotation axis of the Moon [43]. The x axis of this reference frame is the

mean direction from the center of the Moon to the center of the Earth [45]. This axis also defines the mean sub-Earth point, which is the projection of this direction onto the Moon's surface, marking the intersection between the Moon's equator and prime meridian [45, 46, 61, 62, 63]. This direction is averaged over the Moon's librations, caused by orbital inclination, eccentricity (causing slight differences in rotation rate and revolution rate about Earth), and other gravitational forces and perturbations experienced by the Moon [61, 62]. The z direction of the ME frame is defined by the mean polar or rotational axis and the y direction completes the right hand rule [63, 62].

The second, Principal Axis (PA), coordinate system is defined by the principal axes of the Moon's moment of inertia. The frame's orientation was established from gravitational field maps generated by the Gravity Recovery And Interior Laboratory (GRAIL) mission [46, 61, 62, 64]. The gravitational forces and torques due to the Moon's non-uniformly distributed density are responsible for a discrepancy between the MER and PA frames of approximately 1 km at the Moon's surface [45, 61, 62, 63, 65]. To transform between the two reference frames, three constant Euler angles are used as a first order approximation of the rotation [61, 63]. The Euler angles are derived from Developmental Ephemeris (DE) (usually accompanied by a three digit number specifying the release version e.g. DE418) published by NASA's Jet Propulsion Lab (JPL) [45, 61, 63, 65]. JPL DE is updated as more accurate data from lunar laser ranging and other methods becomes available [45]. This allows for lower uncertainty in calculations of higher-degree coefficients in the spherical harmonics gravitational models used to derive rotation between PA and MER frames [63]. Spherical coordinates for all five LRRR in the MER frame are given in Park et al. 2021 [64] and Wagner et al. 2012 [66].

For the purposes of this work, it is desired to have the Cartesian position vector of each LRRR in the Earth-Moon synodic, S frame with the origin at the Earth-Moon system barycenter.

To do this, selenocentric spherical coordinates need to be converted to Cartesian coordinates. This follows the same process as converting from latitude, longitude, and geocentric altitude to Earth Centered, Earth Fixed (ECEF) coordinates. Then, Moon centered Cartesian position vectors of LRRR can be transformed from the MER frame to the S frame. Since the x and y axes of these frames lie in the lunar orbital plane, the z axis of the S frame is parallel to the z axis of the MER frame. The x directions of the MER and S frames are pointing in exact opposite directions and consequentially the y directions are as well. The result is a trivial rotation matrix (3×3 identity with negative first two diagonal elements) to rotate vectors from MER to S.

Additionally, the origin needs to be translated from the lunar center of mass to the barycenter of the Earth-Moon system. This is done by adding the barycentric position vector of the Moon to the selenocentric position vectors of each LRRR in the S frame. If the coordinates of LRRR are given in the PA frame, they first need to be rotated to the MER frame before converting to the S frame. The DE421 Euler angles and rotation matrices from PA to MER and vice versa are given in [61, 63, 64].

2.2.2 Laser Geometry

Over the many years of service, laser ranging ground stations have used different hardware configurations for both sending and receiving laser signals. For the purposes of this discussion we will consider a Q-switched, mode-locked Nd:YAG laser used at the the Apache Point Observatory in New Mexico, detailed in Murphy et al. 2000 [44]. This laser uses a wavelength of 532 nm, and provides a beam divergence angle of $1''$ (1 arcsecond), which translates to a spot size of 2 km on the lunar surface [44]. For the reflected laser beam, the LRRR provides between $7''$ and $10''$ of divergence, which gives a beam diameter of 13 km to 18 km at the

Earth's surface [44, 60].

As mentioned previously, beam divergence plays an important role in enabling a spacecraft to detect the reflected laser pulse despite moving away from the position that the beam is being returned to. Assuming a Gaussian beam geometry far from the laser source, the beam width, $2w$ as a function of axial distance, d from the laser source can be calculated with Equation 2.21 [67].

$$w(d) = d \tan\left(\frac{\Theta}{2}\right) \tag{2.21}$$

In Equation 2.21, Θ is the beam divergence angle shown in Figure 2.10. As seen in figure 2.10, the diverging beam can be visualized as a right circular cone with the apex starting at the laser source and expanding out to the base of the cone ending at a target. In the context of spacecraft laser ranging, the center line of the cone, or axis if the beam, is the line of sight between the spacecraft and the centroid of the LRRR array. For the laser pulse sent from the spacecraft, the apex is the spacecraft's position at the time the pulse was sent, t_{sent}, and the base is the beam width projected on the surface of the Moon. For the returned laser pulse, the apex is the LRRR and the cone expands out towards where the spacecraft was at t_{sent}. The base is the beam width area projected on to a plane in space, normal to the line of sight between the LRRR and the spacecraft at t_{sent}.

To approximate the divergence area experienced by a spacecraft in the vicinity of L_1, let d be the distance between L_1 and the Moon's surface, approximately 57 000 km. The time for light to travel this distance twice is approximately 0.39 s. Using equation 2.21, and a divergence angle of 1″, the beam size on the Moon's surface is about 0.28 km. Using 1″ gives an conservative estimate as a laser packaged on a spacecraft will likely not achieve the same beam divergence performance as a ground station. Additionally, using a divergence angle of 10″, the size of the reflected beam at L_1 is about 2.8 km. This means that in order to receive the reflected laser pulse, a spacecraft must move less than 1.4 km away

perpendicularly from the beam axis, during the time it takes light to travel to the reflector and back ($\Delta t = t_{\text{sent}} - t_{\text{received}}$). This distance limit is specific to motion in the plane that is normal to the beam axis. Alternatively, the average velocity perpendicular to the beam axis during the Δt must not exceed 3.6 km/s. Motion along the direction of the beam axis will change the beam size at the position when the reflected beam is received. The geometry of this scenario is illustrated in Figure 2.11.

For example, if the spacecraft's motion during Δt is directly towards the LRRR along the line of sight, then the beam width at t_{received} will be smaller than at t_{sent} because the light is traveling a shorter distance from the LRRR back to the spacecraft. Additionally, if the spacecraft's motion during Δt is perpendicular in any direction to the beam axis, the beam width observed at t_{sent} and t_{received} will be the same because the light will have traveled the same distance along the line of sight. However, if the distance moved is greater than half the beam width (beam radius) then the spacecraft does not fall within the cone and the reflected laser pulse is not observable by the spacecraft.

Simulated data can be used to verify that the divergence geometry enables a spacecraft orbiting about L_1 to receive a reflected pulse from a LRRR. Consider the baseline halo orbit with dimensional initial conditions in the barycentric S frame:

$$\boldsymbol{r} = \begin{bmatrix} x_0 & y_0 & z_0 \end{bmatrix} = \begin{bmatrix} 320890.4852424654 & 0 & 11683.7162002719 \end{bmatrix} \text{ km}$$

$$\boldsymbol{v} = \begin{bmatrix} \dot{x}_0 & \dot{y}_0 & \dot{z}_0 \end{bmatrix} = \begin{bmatrix} 0 & 0.143008086034200 & 0 \end{bmatrix} \text{ km/s}$$

Assuming a 7″ divergence angle and a 45° angle of incidence limit, the reflected beam diameter at the spacecraft's position during its orbit ranged from 840 m to 1078 m, and

round trip time of the laser, Δt ranged from 0.33 s to 0.42 s. Again, this is a conservative estimate because $7''$ is the minimum in the range of typical divergence angles for LRRR. The beam diameter at the spacecraft's position after Δt was calculated by projecting the relative position vector from the LRRR to the spacecraft at t_{received} on to the line of sight direction from the LRRR to the spacecraft at the position at t_{sent}. This is done to account for the motion of the spacecraft along the laser's path during the Δt. Additionally, the motion of the spacecraft perpendicular to the laser's path was calculated. At t_{received}, the perpendicular distance from the axis of the reflected beam ranged from 51 m to 60 m which was significantly less than the diameter of the diverged beam. During each measurement made, the laser pulse reflected by the LRRR was observable by the spacecraft.

On Earth, the ground stations collect about 5-10 photons per pulse which gives an accuracy of 2 cm and 3000 for 1 mm [44]. Because beam width grows as a function of distance traveled by the light, the intensity of the beam also fades. This is because the same number of photons are becoming spread out over a larger area. A spacecraft in orbit about a L_1 has more favorable conditions for photon collection. The laser beams don't have to travel as far, which means less divergence and higher intensity of reflected pulses. There is also less variability in each collection due to no atmosphere, weather or light pollution affects. Future work can include analyses of photon detection for a spacecraft in orbit about L_1 to determine proper sizing of relevant hardware components, however, it is beyond the scope of the current work.

Now that the necessary concepts for the circular restricted three-body problem, libration points, periodic orbits, monodromy matrix, and laser beam geometry are introduced, they can be employed in a simulation to evaluate the performance of this proposed navigation method.

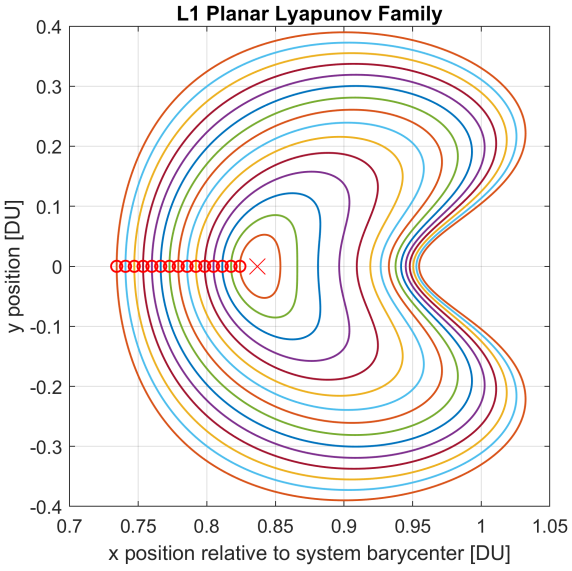

(a) L_1 Lyapunov family.

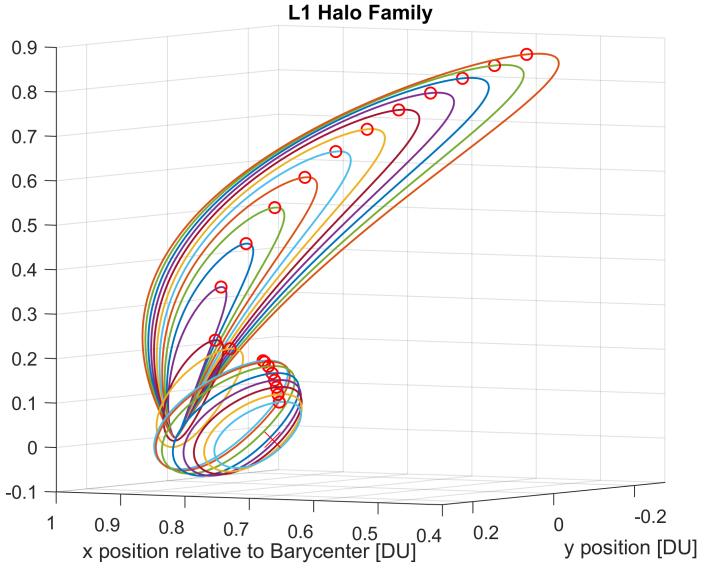

(b) L_1 halo family.

Figure 2.5: Lyapunov and halo families of periodic orbits around L_1.

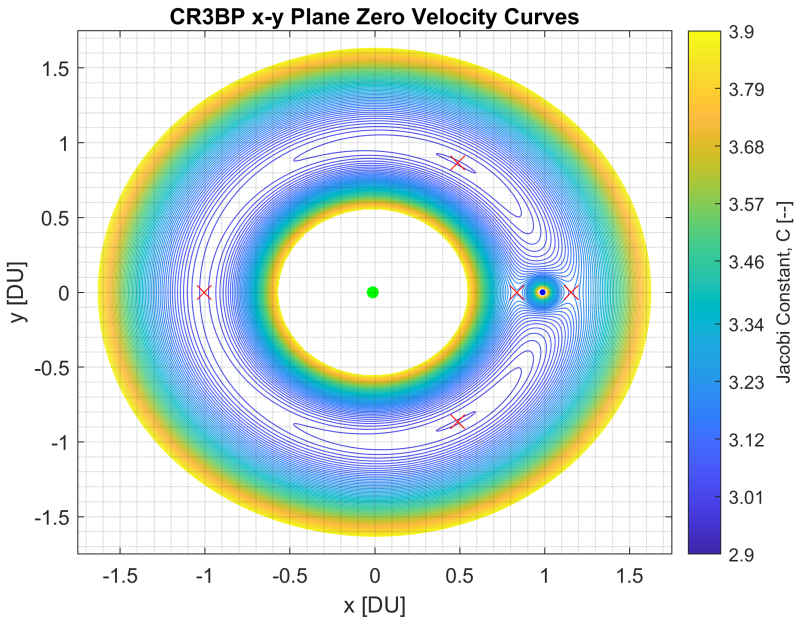

(a) Zero velocity curves in the $x - y$ plane.

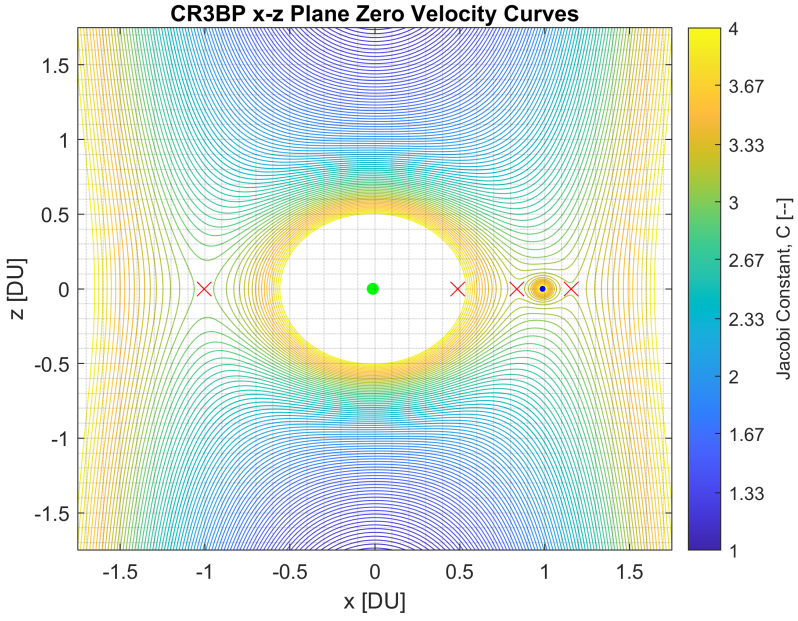

(b) Zero velocity curves in the $x - z$ plane.

Figure 2.6: Zero velocity curves in the Earth-Moon CR3BP.

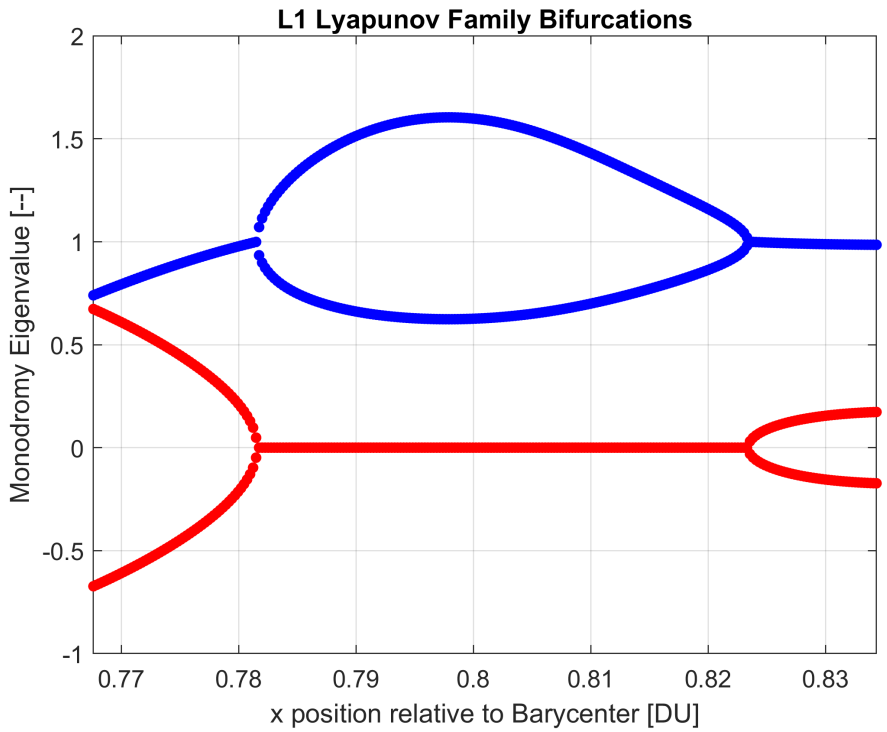

Figure 2.7: Eigenvalues of the monodromy matrix for orbits in a section of the planar Lyapunov family about L_1.

Figure 2.8: Lunar laser ranging station, courtesy of [3].

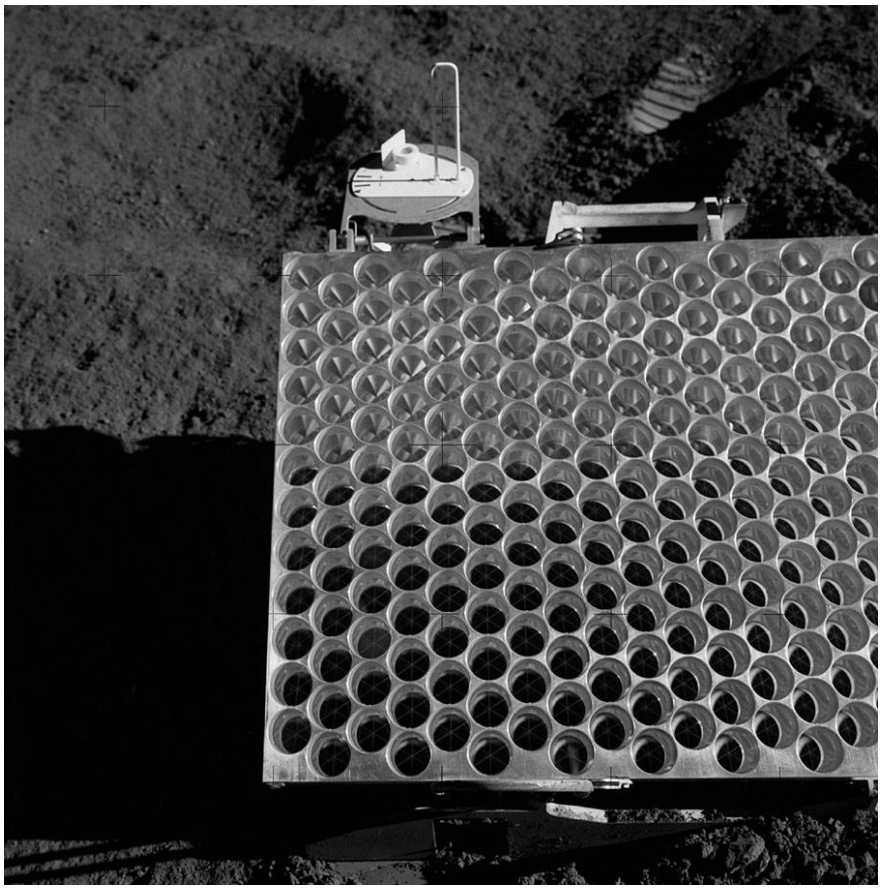

Figure 2.9: Close up view of LRRR placed during Apollo 15, courtesy of [4].

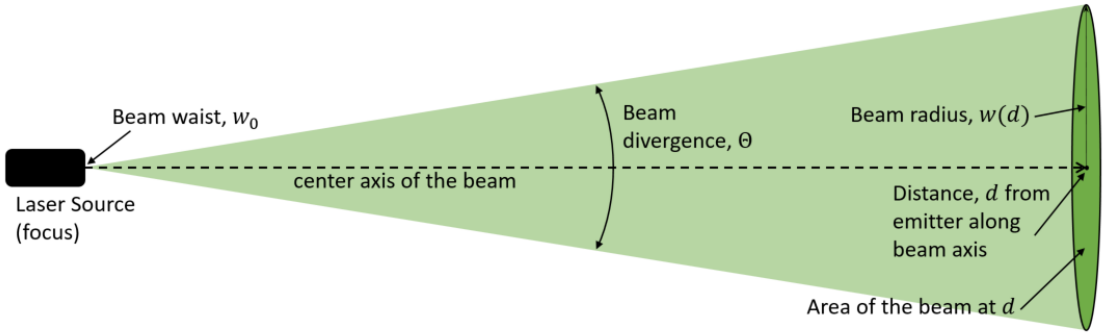

Figure 2.10: Gaussian Laser Beam Geometry.

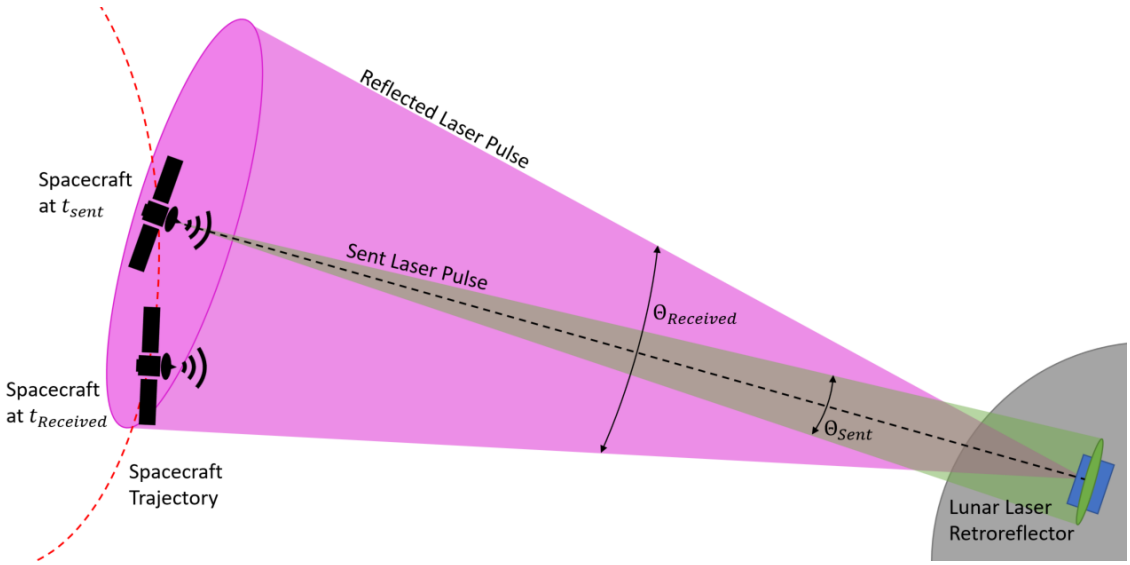

Figure 2.11: Send and Receive Beam Divergence Geometry.

Chapter 3

Methodology

In order to analyze the feasibility and performance of spacecraft laser ranging to LRRR for navigation in libration point orbits, a simulation framework was constructed. The general work flow of the program is as follows:

- The three-body system, spacecraft, and simulation are initialized from input parameters
- Pre-simulation calculations are executed
  - Non-dimensionalizing or dimensionalizing parameters based on simulation inputs
  - Libration point positions in CR3BP
  - LRRR locations are calculated and transformed into CR3BP
  - Initial conditions for periodic orbit solution are corrected from initial guess
  - The reference trajectory is constructed
- Specific analysis functions are called (if applicable)
  - Some functions dont require simulation data, and only need the three body system parameters, spacecraft input parameters, or pre-simulation calculations for running analyses and generating figures. Examples include finding bifurcation points, LRRR visibility studies, plotting zero velocity curves (Fig. 2.6), pulling

data from the JPL database, and generating diagrams such as Figures 3.1, 2.6, and 2.7.

- Run the main simulation
  - Corrected initial conditions for the true and estimated trajectories are propagated forward in time in the CR3BP dynamics
  - If a measurement update is scheduled at the current time step, the input-specified navigation algorithm (EKF or SRF) provides a updated spacecraft state estimate which is propagated to the next simulation time step
  - If a measurement update is not scheduled, then the estimated states at the current time step are propagated forward without a update from the estimator
- Simulation results such as final trajectories and state estimation error are plotted with other performance metrics used for analysis

3.1 Periodic Orbit Initial Conditions

There are two conventions for defining initial conditions of halo and Lyapunov orbits around any of the collinear libration points. Satellites in these orbits generally travel clockwise about the synodic frame z axis and intersect the $x-z$ plane twice in a single period, where they can be specified by the conditions at either crossing point. The actual rotation axis for halo orbits will have some angular offset relative to the synodic z axis. The average orbit plane of a halo will be tilted with respect to the three-body orbit plane. This offset will be greater for halos with larger z amplitudes. The following discussion in Section 3.2 and initial conditions listed in Tables 1.1, 4.2, and 4.1 use the convention where the orbits start on the x axis with an initial velocity v_y in the positive y direction with $x_{\text{InitialCondition}} < x_{\text{LibrationPoint}}$. Furthermore,

all of the initial conditions in this thesis are specified with respect to the CR3BP system barycenter unless otherwise specified.

The other convention uses $x_{\text{InitialCondition}} > x_{\text{LibrationPoint}}$ and an initial velocity v_y in the negative y direction. It is important to note that the JPL database ([5]) makes use of both conventions. If the second convention is followed, the change of sign in the y position component when crossing the $x-z$ plane will be the opposite as mentioned in Section 3.2.

3.2 Finding Solutions in the CR3BP

A two-stage single shooting correction method was employed to find periodic solutions to the CR3BP about L_1 (illustrated for L_1 in Fig. 3.1). An initial guess is propagated forward in time until the trajectory crosses the $x-z$ plane, at approximately half of a periodic orbit (shown in Fig. 3.1a). This stopping condition is triggered when the value of y becomes zero, or changes from positive to negative. The initial condition is then corrected until the trajectory crosses the $x-z$ plane perpendicularly, shown by the green trajectory in Figure 3.1b. This constraint is enforced by minimizing the x and z components of velocity at the plane crossing (when $y = 0$). The corrected initial condition from the first stage is then used as the initial guess for the second stage. The refined initial condition is propagated forward again in time until it crosses the $x-z$ plane twice, approximately a full periodic orbit (shown in Fig. 3.1c. This end condition is triggered when the value of y becomes zero again, or changes from negative back to positive. The initial condition is then corrected again to ensure that the resulting trajectory crosses the $x-z$ plane perpendicularly each time, satisfying the requirement for periodicity (shown by red trajectory in Fig. 3.1d). In practice, this is accomplished by using a numerical solver to minimize the $x-z$ plane crossing conditions by tweaking initial conditions after propagating until an event or crossing has

occurred.

3.3 Simulation

The simulation begins by propagating the periodic initial conditions in the CR3BP dynamics forward in time by one time step. The initial estimated states are the periodic initial conditions with added random error, scaled by an initial covariance matrix, P_0, defined by Equation 3.1 and values in Table 3.1. This error is to show convergence of the filters while also modeling some realistic orbit injection error from maneuvering to arrive at the libration point.

$$P_0 = \begin{bmatrix} \sigma_{\boldsymbol{r}_0}^2 & 0 & 0 & 0 & 0 & 0 \\ 0 & \sigma_{\boldsymbol{r}_0}^2 & 0 & 0 & 0 & 0 \\ 0 & 0 & \sigma_{\boldsymbol{r}_0}^2 & 0 & 0 & 0 \\ 0 & 0 & 0 & \sigma_{\boldsymbol{v}_0}^2 & 0 & 0 \\ 0 & 0 & 0 & 0 & \sigma_{\boldsymbol{v}_0}^2 & 0 \\ 0 & 0 & 0 & 0 & 0 & \sigma_{\boldsymbol{v}_0}^2 \end{bmatrix} \tag{3.1}$$

After each propagation, the code checks to see if a measurement update or trajectory correction burn is scheduled to be applied at the current step. For navigation, a measurement frequency f_z is prescribed by the simulation input parameters which gets compared with the current simulation time, t_{sim}, and executed at the specified time intervals.

The navigation module takes care of the state estimation functions of the simulation. It uses the measurement model, given in Section 3.4 to provide a better estimate of the spacecraft's position and velocity through the use of an Extended Kalman Filter (EKF) or a Square Root Filter (SRF) which are described in further detail in Sections 3.5 and 3.6.

Because this is a simulation, there are three different trajectories or sets of spacecraft states

that are maintained; true, reference, and estimated. The true states define the actual motion of the spacecraft subject to the dynamical environment, and the estimated states are what the spacecraft thinks its motion is. The reference states define the ideal trajectory which is what the spacecraft is supposed to follow. However, process noise, modeling errors, measurement error, control errors, etc. all perturb the spacecraft which cause the true and estimated trajectories to deviate from the reference, and from each other. Although one could make the simulation have zero errors, it is important to model these quantities to add fidelity and conduct a realistic analysis of the methods being used. Table 3.1 lists the standard deviations used to define the noise and error in the initial estimation of the spacecraft states.

Table 3.1: Baseline simulation parameters used to generate results.

Parameter	Symbol	Value
Position process noise standard deviation	$\sigma_{Q_{\boldsymbol{r}}}$	$0\,\mathrm{mm/h}$
Velocity process noise standard deviation	$\sigma_{Q_{\boldsymbol{v}}}$	$3.33\,\mathrm{mm/s/h}$
Measurement error standard deviation	σ_R	$2\,\mu\mathrm{s}$
Initial position error standard deviation	$\sigma_{\boldsymbol{r}_0}$	$1\,\mathrm{km}$
Initial velocity error standard deviation	$\sigma_{\boldsymbol{v}_0}$	$2\,\mathrm{m/s}$
Simulation time step	Δt_{sim}	$2\,\mathrm{min}$
Measurement frequency	f_z	1 measurement / $6\Delta t_{\mathrm{sim}}$
LRRR laser divergence	Θ_{LRRR}	7 arcseconds
Spacecraft laser divergence	Θ_{SC}	5 arcseconds

Since it is likely that a spacecraft on a trajectory to a libration point about L_1 will be tracked by ground based services like the DSN, the initial position and velocity error to start the simulation can be assumed to be small. Under this assumption, the simulation will begin as if the spacecraft has already made any approach maneuvers necessary to enter an orbit about L_1, plus some random orbit injection error. The measurement frequency represents how often measurements are scheduled to be taken. This was chosen to be once every six simulation time steps (once every 12 minutes) or equivalently, around 150 measurements during one period of the baseline orbit. The process noise values were adapted from [68],

where σ_{Q_v} represents three-sigma of 1 mm/s of velocity, accumulated over the course of an hour. The measurement noise is adapted from the standard deviation experienced by ground stations given in [43]. Ground stations experience measurement fluctuations on the order of 2 ns [43]. For a spacecraft equipped with presumably less sensitive equipment, it is reasonable to expect the onboard hardware to achieve a microsecond or better level of accuracy.

Additionally, it is expected that a on-board laser will transmit laser pulses with divergence angles between the maximum performance of the ground stations (1″) and LRRR (7″). For the simulation, 5″ is used. The assumed laser divergence value for spacecraft-based laser ranging dictates the required pointing accuracy of the attitude determination and control system (ADCS) of the spacecraft. The divergence angle of each transmitted laser pulse translates to a beam area at the target LRRR on the Moon's surface. This means that the projected surface area covered by the beam must include the location of the target LRRR. In order to ensure the laser hits the target, a spacecraft needs to achieve a pointing accuracy that is on the order of less than or equal to half the divergence angle of the laser transmitted by the spacecraft. For $\Theta_{\text{SC}} = 5''$, the ADCS must provide a pointing accuracy of approximately 2.5″ or better.

Because the initial conditions are computed prior to the simulation being ran, the ideal periodic orbit is also computed in the guidance module, prior to the main simulation. An ideal trajectory is then constructed by "stacking" single periodic orbits on top of each other until the combined periods are greater than or equal to the simulation duration. Here, the end states of each periodic become the starting states for each successive orbit.

Even with high precision numerical solvers, the end conditions of the calculated periodic orbit do not exactly match the initial conditions. There is some small offset between the orbits beginning and ending points which is illustrated in Figure 3.2. This becomes an issue when linking periodic orbits together for constructing the reference trajectory. A discontinuity is

created in the reference states when crossing from one orbit to the next. Each successive orbit continues from the end of the previous, which overwrites the true initial conditions for the periodic orbit with the end conditions that includes the offset error. This causes an abrupt jump in the reference trajectory because the second time step in each consecutive orbit does not have the correct states to follow the overwritten initial condition. In order to avoid this discontinuity, a corrected periodic orbit is used to make the reference trajectory. The calculated periodic orbit is mirrored across the $x-z$ plane and the time steps are flipped. The result is two calculated periodic orbits, one mirrored and the original which are are perfectly symmetric across $x-z$ axis when moving forward in time. The two sets of orbit states were then averaged over one period where more weight was placed on the original states during the first half of the orbit and the mirrored states were weighed more during the second half.

$$\boldsymbol{X}_{\text{corrected}} = \boldsymbol{X}_{\text{origional}}\left(1 - \frac{t_j}{T}\right) + \boldsymbol{X}_{\text{mirrored}}\left(\frac{t_j}{T}\right) \tag{3.2}$$

Equation 3.2 gives the weighting scheme for averaging the two periodic orbits. T is the period, and t_j is time time at time step j in the time step vector for the original periodic orbit. This generated a corrected periodic orbit with the end conditions exactly matching the initial conditions. Using this orbit in creating the reference trajectory removed the discontinuity and allowed for a smooth transition between the chained periodic orbits.

Since this is precomputed, the ideal trajectory states may be defined at different time steps from the simulated true and estimated states. During each propagation step, the reference trajectory states are found from interpolating the ideal trajectory at the simulation time steps. Both the true and estimated states are propagated each simulation step from k to $k+1$ and stored such that all three sets of states are defined at every simulation time step.

Then, the true states are propagated along with a state transition matrix, $\Phi_{\text{true}}(k+1,k)$, and the discrete time process noise covariance matrix, Q_{total}. The process noise vector, $\boldsymbol{\nu}$, is assumed to be sampled from a white Gaussian distribution with zero mean and constant, known covariance, Q_{total}. On the other hand, Q is the constant, known continuous time process noise covariance matrix, given by Equation 3.3 and values listed in Table 3.1.

$$Q = \begin{bmatrix} \sigma_{Q_r}^2 & 0 & 0 & 0 & 0 & 0 \\ 0 & \sigma_{Q_r}^2 & 0 & 0 & 0 & 0 \\ 0 & 0 & \sigma_{Q_r}^2 & 0 & 0 & 0 \\ 0 & 0 & 0 & \sigma_{Q_v}^2 & 0 & 0 \\ 0 & 0 & 0 & 0 & \sigma_{Q_v}^2 & 0 \\ 0 & 0 & 0 & 0 & 0 & \sigma_{Q_v}^2 \end{bmatrix} \tag{3.3}$$

The discrete process noise covariance, Q_{total}, represents the accumulated affect of the continuous process noise covariance Q over time and is calculated from numerically integrating the continuous Lyapunov equation, Eqn. 3.4, over time. After the propagation, the process noise vector, $\boldsymbol{\nu}$ is calculated from the resulting Q_{total}. The lower triangular matrix from a Cholesky decomposition of Q_{total} is used to scale a 6×1 vector of normally distributed random numbers to get $\boldsymbol{\nu}$. The process noise is then added to the stored true states at the next time step $(k+1)$.

$$\dot{Q}_{\text{total}} = AQ_{\text{total}} + Q_{\text{total}}A^T + Q \tag{3.4}$$

In Equation 3.4 and 3.5, A is the same Jacobian matrix used in propagating the STM, defined by Equation 2.18. The STM transforms the true states from the beginning, $\boldsymbol{X}_{\text{true}}(k)$, to the end of the propagation, $\boldsymbol{X}_{\text{true}}(k+1)$. The process noise covariance is included in the propagation to capture random noise accumulated during the propagation time and introduce

random errors in the true states which cause them to drift from the reference states. This is to account for any unmodeled dynamics and mimic the natural drifting of a spacecraft caused by environmental disturbances.

The estimated states are also propagated with a state transition matrix, $\Phi_{\text{estimate}}(k+1,k)$, and the state estimation error covariance, P. This STM transforms the estimated states from the beginning, $\boldsymbol{X}_{\text{estimate}}(k)$, to the end of the propagation, $\boldsymbol{X}_{\text{estimate}}(k+1)$. P is propagated instead of Q_{total} with Equation 3.5, which is the same formula for propagating Q_{total} (Eqn. 3.4). In the simulation, process noise is not added to the estimated states, however, they are subjected to measurement noise from the actual measurement. This is because the estimator assumes the process noise to be zero mean, and therefore the best estimate is that the average affect of the noise on the states is also zero. Although process noise does not change the the state estimate, it does affect the estimator's level of uncertainty behind the estimate. To account for this, process noise is added to the state estimation error covariance during the propagation of P.

$$\dot{P} = AP + PA^T + Q \tag{3.5}$$

In the code, the elements of the 6×6 STM are reshaped into a 36×1 vector and the and the upper triangle elements of a 6×6 covariance matrix (Q_{total} or P) are reshaped into a 21×1 vector. Because covariance matrices are symmetric, only the elements which make up upper or lower triangle need to be stored in order to reproduce the full matrix. An augmented 63×1 state vector can be constructed from stacking the original 6×1 position and velocity spacecraft states on the 36×1 STM vector and 21×1 covariance vector. The propagation is done by integrating Equations 2.17 and 3.5 or 3.4, given in [68], in tandem with the CR3BP equations of motion (Eqn. 2.9 or 2.6) as they are all functions of the spacecraft states.

For each propagation, Q_{total} starts as a zero matrix ($0_{6\times6}$) as the initial condition to account for the process noise that accumulates over each propagation. The state error covariance gets propagated from its value at the previous time step because it is needed as P evolves over time. It is useful to have the state transition matrix over each propagation, from k to $k+1$ rather than from the beginning of the simulation, $k=0$, to the latest time step, $k+1$. For this reason, the STM starts as an identity matrix ($I_{6\times6}$), the same as done for the monodromy matrix in Section 2.1.3.

3.4 Measurement Model

Laser ranging determines the distance from a lunar retroreflector array by measuring the time elapsed between a sent laser pulse and the received pulse that was reflected by the LRRR. Since the laser pulses travel at the speed of light and the passage of time is directly measured, distance is found from the measurement Equation 3.6.

$$\begin{aligned} c\Delta t &= \rho(t) + \rho(t+\Delta t) \\ &= \rho(t_{\text{sent}}) + \rho(t_{\text{received}}) \\ &= \rho_{\text{sent}} + \rho_{\text{received}} \end{aligned} \tag{3.6}$$

c is the speed of light, Δt is the time difference between the sent and received signals. ρ is the distance from a LRRR to a satellite's position at time, t, mathematically represented by Equation 3.7.

$$\begin{aligned} \rho_{\text{sent}} &= ||\boldsymbol{r}_{\text{sent}} - \boldsymbol{r}_{\text{LRRR}}||_2 \\ \rho_{\text{received}} &= ||\boldsymbol{r}_{\text{received}} - \boldsymbol{r}_{\text{LRRR}}||_2 \end{aligned} \tag{3.7}$$

The subscript LRRR is general and can represent any of the five retroreflectors. The known

positions in the synodic frame have been derived from [43, 61, 63, 64, 66, 69] and are listed in Table 3.2 .

Table 3.2: Positions of LRRR in the Earth-Moon Synodic Frame.

LRRR	x Position (DU)	y Position (DU)	z Position (DU)
Apollo 11	0.983764903941013	-0.001773715710147	0.000052342000053
Apollo 14	0.983608192061154	0.001335516281451	-0.000283193442533
Apollo 15	0.983859360428792	-0.000253026352650	0.001961526392743
Luna 17 (Lunokhod 1)	0.984988370208490	0.002003920724898	0.002760134242914
Luna 21 (Lunokhod 2)	0.984412472275165	-0.002058775194233	0.001939552224127

In practice, a spacecraft will measure Δt, so the actual scalar measurement function, $\underline{h}$ is given by Equation 3.8, where Δt and the states at t_{received} are a function of the states at t_{sent}.

$$\begin{aligned} \underline{h}(\boldsymbol{X}_{\text{sent}}) = \underline{h}(\boldsymbol{r}_{\text{sent}}, \boldsymbol{r}_{\text{received}}) &= \Delta t \\ &= \frac{\rho_{\text{sent}} + \rho_{\text{received}}}{c} \end{aligned} \tag{3.8}$$

Because the spacecraft is moving along its trajectory when the laser pulse is transmitted, it will be in a different position by the time the reflected pulse returns to the spacecraft's previous position at t_{sent}. This scenario is depicted in Figure 2.11. In navigation applications that use measurements such as radar, lidar, laser ranging, etc., the distances measured are often small relative to the speed of the transmitted electromagnetic radiation. In these cases, the change in the vehicle states during the measurement is typically ignored. In the case of spacecraft laser ranging, the distances traveled by the laser pulses are much larger where the measurement cannot be assumed to occur instantaneously. While the distance from the LRRR at $\boldsymbol{r}_{\text{sent}}$ versus $\boldsymbol{r}_{\text{received}}$ may be similar, the change in spacecraft position and velocity with respect to its orbit is significant and must be accounted for.

To compensate for the motion during the measurement, Δt is calculated by propagating the

spacecraft's state at t_{sent} until the spacecraft reaches the next point in its trajectory that satisfies the measurement equation. In other words, since the ρ_{sent} is defined when the pulse is transmitted, the spacecraft state vector is propagated until the distance covered by the laser in Δt is equivalent to the distance from the spacecraft (at t_{sent}) to the LRRR plus the distance from the LRRR to the spacecraft at some time in the future (t_{received}). The states at the end of the propagation where the measurement equation is satisfied become $\boldsymbol{X}_{\text{received}}$ and the time duration of the propagation becomes the measurement, Δt.

It is important to note that this propagation is separate from the main simulation propagation and only occurs within the measurement update navigation step. The measurement propagation also starts at the current simulation time step, k, when the simulation time (t_{sim}) at k is equivalent to one of the scheduled measurement times, $t_{\text{sent}} = k_{\text{sent}}\Delta t_{\text{sim}}$. The end of the measurement propagation, t_{received} occurs somewhere in between the simulation time steps k and $k+1$. Since t_{received} is not necessarily significant other than for the measurement update, $\boldsymbol{X}_{\text{received}}$ is only used to update the estimate at $\boldsymbol{X}_{\text{sent}}$, stored as $\boldsymbol{X}(k)$ in the main simulation. Then the updated $\boldsymbol{X}(k)$ is propagated by the simulation to the next step, and $\boldsymbol{X}_{\text{received}}$ is overwritten during the next measurement update.

Once the propagation is complete, the geometry between $\boldsymbol{r}_{\text{sent}}$, $\boldsymbol{r}_{\text{received}}$, and $\boldsymbol{r}_{\text{LRRR}}$ is checked to make sure that the geometric constraints described in Section 2.2.2 are not violated and verify that the measurement was physically possible. Two main checks are conducted to validate if the geometry of a spacecraft's orbit allows for a measurement to be made. The first check verifies that the angle between the line of sight from LRRR to spacecraft, and the direction normal to the LRRR panel (assumed to be pointing in the direction of Earth) is within the angle of incidence limit of the LRRR (assumed to be 45°). The second check mentioned in Section 2.2.2 verifies that the spacecraft does not move out of beam divergence cone during the time of flight of the laser. If the spacecraft travels too far from the center

line of the reflected beam, the spacecraft will not be able to detect the returned laser pulse and a measurement cannot be made.

The Jacobian matrix of the measurement equation will become important when estimating the spacecraft's states after each measurement. This is found by taking the derivative of the measurement equation (Equation 3.6) with respect to each of the states at t_{sent}. This matrix is given in Equation 3.9 and the full derivation can be found in Appendix A.

$$\begin{aligned} H &= \frac{\partial \underline{h}}{\partial \boldsymbol{X}_{\text{sent}}} \\ &= \frac{\partial}{\partial \boldsymbol{X}_{\text{sent}}} \left(\frac{\rho_{\text{sent}} + \rho_{\text{received}}}{c} \right) \\ &= \begin{bmatrix} \frac{\partial \Delta t}{\partial x_{\text{sent}}} & \frac{\partial \Delta t}{\partial y_{\text{sent}}} & \frac{\partial \Delta t}{\partial z_{\text{sent}}} & \frac{\partial \Delta t}{\partial \dot{x}_{\text{sent}}} & \frac{\partial \Delta t}{\partial \dot{y}_{\text{sent}}} & \frac{\partial \Delta t}{\partial \dot{z}_{\text{sent}}} \end{bmatrix} \\ &= \begin{bmatrix} \frac{\partial \Delta t}{\partial \boldsymbol{r}_{\text{sent}}} & \frac{\partial \Delta t}{\partial \dot{\boldsymbol{r}}_{\text{sent}}} \end{bmatrix} \\ &= \begin{bmatrix} \frac{\rho_{\text{received}} \boldsymbol{\rho}_{\text{sent}}^T + \rho_{\text{sent}} \boldsymbol{\rho}_{\text{received}}^T \Phi_{\boldsymbol{rr}}}{\rho_{\text{sent}} (c\rho_{\text{received}} - \boldsymbol{\rho}_{\text{received}}^T \boldsymbol{v}_{\text{received}})} & \frac{\boldsymbol{\rho}_{\text{received}}^T \Phi_{\boldsymbol{rv}}}{c\rho_{\text{received}} - \boldsymbol{\rho}_{\text{received}}^T \boldsymbol{v}_{\text{received}}} \end{bmatrix} \end{aligned} \tag{3.9}$$

The state transition matix and its sub-matrices are defined in Equation 2.15. In this case, the STM, $\Phi(t_{\text{received}}, t_{\text{sent}})$, transitions from t_{sent} to t_{received}. Each element of the resulting 1×6 H matrix represents the sensitivity in the Δt to changes in the states at t_{sent}. However, since Δt is a measured quantity, H really represents the sensitivity of the $\boldsymbol{X}_{\text{received}}$ states subject to changes in the $\boldsymbol{X}_{\text{sent}}$ states.

In the simulation code, this matrix is calculated by evaluating the last line of Equation 3.9 with the results of the measurement propagation. This propagation used to satisfy the measurement equation also yields the spacecraft states at t_{received} and the STM between the sent and received states. This method of numerically finding the $\boldsymbol{X}_{\text{received}}$ states during each measurement update to find the measurement Jacobian is necessary to emulate the process of a spacecraft making ranging measurements in the real cislunar environment. Once the

Jacobian matrix and the measurement are found, and the geometry checks are made, they are passed on to the extended Kalman filter or square root filter.

3.5 State Estimation: Extended Kalman Filter

The measurement is then ran through an Extended Kalman Filter (EKF) or a Square Root Filter (SRF) which provides an estimate of the state vector and state error covariance matrix at t_{sent}. This process is executed in two steps, the dynamic propagation or prediction step and measurement update step.

3.5.1 EKF Dynamic Propagation

An iteration of the algorithm starts with the estimated states and state error covariance at some time step, k, where the dynamics are propagated forward to get the state vector at time step $k+1$. This is characterized by traditional EKF Equations 3.10 and 3.11.

$$\bar{\boldsymbol{x}}(k+1) = \underline{\boldsymbol{f}}\big[\hat{\boldsymbol{x}}(k), \boldsymbol{u}(k)\big] \tag{3.10}$$

$\bar{\boldsymbol{x}}$ is the "*a priori*" (before measurement update) state estimate, $\hat{\boldsymbol{x}}$ is the "*a posteriori*" (after measurement update) state estimate, vector function $\underline{\boldsymbol{f}}$ represents the propagation of the nonlinear dynamics model from k to $k+1$, and $\boldsymbol{u}$ is the control input vector which in our case is zero. The assumption that the spacecraft is capable of accurately maintaining the reference trajectory is fulfilled in the simulation by forcing the true states equal to the reference states at each time step. Therefore additional control inputs are not necessary in

this case.

$$\bar{P}(k+1) = F(k)P(k)F^T(k) + \Gamma(k)Q(k)\Gamma^T(k) \tag{3.11}$$

Where $\bar{P}$ is the *a priori* state estimation error covariance matrix, P is the *a posteriori* state estimation error covariance matrix. Γ and F are Jacobian matrices of $\underline{\boldsymbol{f}}$ with respect to the spacecraft state and process noise vectors, defined by:

$$F(k) = \left.\frac{\partial \underline{\boldsymbol{f}}}{\partial \boldsymbol{x}(k)}\right|_{[\hat{\boldsymbol{x}}(k),\boldsymbol{u}(k)]} \tag{3.12}$$

$$\Gamma(k) = \left.\frac{\partial \underline{\boldsymbol{f}}}{\partial \boldsymbol{\nu}(k)}\right|_{[\hat{\boldsymbol{x}}(k),\boldsymbol{u}(k)]} \tag{3.13}$$

The function $\underline{\boldsymbol{f}}$ takes the most recent estimate of the state vector and control input at time step, k as inputs and returns the states at the next time step. Here, F follows the same definition as A in Equation 2.18 and the matrix, Γ maps or describes how the process noise components effect the states. In this application, Γ is the identity matrix because process noise covariance was defined to be a diagonal matrix. Thus, Equation 3.11 can be simplified.

$$\bar{P}(k+1) = A(k)P(k)A^T(k) + Q(k) \tag{3.14}$$

In this application, the traditional propagation step given by Equations 3.10 and 3.14 is replaced by the propagation process described in Section 3.3 which takes place outside the navigation module. It occurs every time step of the simulation, regardless if a measurement update is made or not. On a real spacecraft, it is unlikely that measurement updates will be performed continuously. Rather, it will take measurements at some frequency which maintains an acceptable level of accuracy and does not interfere with other on-board operations. Since the simulation is not propagating consecutive measurement updates, more accurate

notation for Equation 3.10 would be:

$$\bar{\boldsymbol{x}}(k+1) = \underline{\boldsymbol{f}}\big[\bar{\boldsymbol{x}}(k), \boldsymbol{u}(k)\big] \tag{3.15}$$

3.5.2 EKF Measurement Update

From the propagation step of the EKF, the most recent state estimate, $\bar{\boldsymbol{x}}(k)$, and corresponding error covariance, $\bar{P}(k+1)$, are known. Note that k and $k+1$ here are still used to distinguish between simulation time steps, while in traditional Kalman filter notation, k and $k+1$ are used to distinguish between measurement samples. The rate at which new measurement samples are available is not always the same as the rate of the simulation. In other words, measurement samples may not occur uniformly or regularly in time such as at the simulation time steps. In this implementation however, the measurement frequency or sample rate is chosen to be an integer multiple, b, of the simulation step size such that new measurement samples become available at every b^{th} time step. To reiterate from Section 3.4, when a measurement update is scheduled at simulation time step, $k = k_{\text{sent}}$ the update occurs prior to the simulation propagation to $k+1$. Therefore, when the EKF gets called, the measurement sample at the current time step k is the most recent.

The actual measurement taken by a spacecraft is simulated from the Δt found in the measurement propagation from t_{sent} to t_{received}, described in Section 3.4. This is given by evaluating the nonlinear measurement model function from Equation 3.8 at the true spacecraft states:

$$\begin{aligned} \boldsymbol{z}(k) &= \underline{h}\big[\boldsymbol{x}_{\text{true}}(k)\big] + w \\ &= \underline{h}\big[\boldsymbol{x}_{\text{true,sent}}\big] + w \\ &= \Delta t + w \end{aligned} \tag{3.16}$$

Because the propagation to find Δt and $\boldsymbol{x}_{\text{recieved}}$ is part of evaluating the measurement model, $\underline{h}$ is really just a function of the states at t_{sent}. w is the measurement or observation noise which is assumed to be sampled from a white Gaussian distribution with zero mean and known, constant covariance, R. The measurement is a scalar quantity, so the measurement covariance matrix is 1×1 in this case, given by Equation 3.17 and the standard deviation of the measurement error, σ_R, listed in Table 3.1. w is calculated by scaling a 1×1 normally distributed random number by the Cholesky of R, which in this case is just σ_R.

$$R = \left[\sigma_R^2\right] \tag{3.17}$$

The measurement prediction is then calculated from evaluating the measurement model at the *a priori* state estimate at $k+1$:

$$\begin{aligned} \bar{\boldsymbol{z}}(k) &= \underline{h}\left[\bar{\boldsymbol{x}}(k)\right] \\ &= \underline{h}\left[\boldsymbol{x}_{\text{estimate,sent}}\right] \end{aligned} \tag{3.18}$$

The innovation or measurement residual is then:

$$\tilde{\boldsymbol{\nu}}(k) = \boldsymbol{z}(k) - \bar{\boldsymbol{z}}(k) \tag{3.19}$$

Where $\boldsymbol{z}$ is the actual measurement and $\bar{\boldsymbol{z}}$ is the anticipated measurement at simulation time step k.

The covariance of the innovation is given by:

$$S(k) = H(k)\bar{P}(k)H^T(k) + R(k) \tag{3.20}$$

Where R is the covariance of the measurement noise, defined by Equation 3.17 and H is the Jacobian of the measurement model, given by Equation 3.9 and evaluated during the measurement propagation detailed in Section 3.4. Kalman Gain matrix is found using:

$$W(k) = \bar{P}(k)H^T(k)S^{-1}(k) \tag{3.21}$$

Then the *a posteriori* state estimate and *a posteriori* state estimation error covariance matrix are found:

$$\hat{\boldsymbol{x}}(k) = \bar{\boldsymbol{x}}(k) + W(k)\tilde{\boldsymbol{\nu}}(k) \tag{3.22}$$

$$P(k) = \bar{P}(k) - W(k)S(k)W^T(k) \tag{3.23}$$

$\hat{\boldsymbol{x}}(k)$ and $P(k)$ are the updated state estimate for $\hat{\boldsymbol{X}}_{\text{sent}}$ and P_{sent}, this will replace the previous state estimate, $\boldsymbol{X}_{\text{estimate}}(k)$, at the current time step, $k = k_{\text{sent}}$ in the simulation. The code will then propagate forward until the next scheduled measurement or correction maneuver.

3.6 State Estimation: Square Root Filter

An alternative formulation for an extended Kalman filter is the square root filter (SRF), adapted from [70]. This follows similar formulation to the EKF in Section 3.5 with the main difference being the use of the square root of the state estimation covariance, L instead of P. L is defined as the lower triangular matrix resulting from the Cholesky factorization of P, where $P = LL^T$. The implementation of the code is nearly identical. The set of equations that gets called in the code is dictated by the simulation input parameter specifying which filter to use. The SRF is sometimes used in favor of the EKF because employing L instead of

P can significantly reduce the numerical error accumulated during propagation and improve the accuracy of estimating the spacecraft states.

3.6.1 SRF Dynamic Propagation

In the dynamic propagation step described in Sections 3.3 and 3.5, Equation 3.24 from [71] replaces 3.5 such that L gets propagated with the state vector instead of P.

$$\begin{aligned}
\dot{L} &= L\left[L^{-1}\dot{P}L^{-T}\right] \\
&= L\left[L^{-1}\left(AP + PA^T + Q\right)L^{-T}\right] \\
&= L\left[L^{-1}\left(ALL^T + LL^TA^T + Q\right)L^{-T}\right] \\
&= L\left[L^{-1}ALL^TL^{-T} + L^{-1}LL^TA^TL^{-T} + L^{-1}QL^{-T}\right] \\
&= L\left[L^{-1}AL + L^TA^TL^{-T} + L^{-1}QL^{-T}\right] \\
&= LL^{-1}AL + LL^TA^TL^{-T} + LL^{-1}QL^{-T} \\
&= L^{-1}AL + LL^TA^TL^{-T} + QL^{-T}
\end{aligned} \tag{3.24}$$

In the second line of Equation 3.24, the definition for $\bar{P}$ (Eqn. 3.5) was substituted in. The third line made use of the definition $P = LL^T$.

3.6.2 SRF Measurement Update

The measurement update step of the SRF starts the same as the EKF, at $k = k_{\text{sent}}$ where $\bar{\boldsymbol{X}}(k)$ and $\bar{L}(k)$ are known.

The actual and predicted measurement as well as the innovation formulas are the same as the EKF, given by Equations 3.16, 3.18, and 3.19 respectively.

The square root of the innovation covariance is found by taking the QR decomposition of an augmented matrix:

$$\begin{bmatrix} O_1 & U_1 \end{bmatrix} = \text{qr}\left(\begin{bmatrix} \left(H(k)\bar{L}(k) \right)^T \\ \sqrt{R}^T(k) \end{bmatrix} \right) \tag{3.25}$$

The QR decomposition returns an upper-triangular matrix, U_1 and a square orthogonal matrix, O_1. The orthogonal matrix is ignored as it is not needed and the upper-triangular matrix becomes $\sqrt{S}(k)$. The diagonal elements of $\sqrt{S}(k)$ must be positive to follow standard Cholesky square-root form. This is to maintain positive definiteness in covariance matrices and prevent issues in subsequent calculations. A simple sign check and modification is applied in the code when necessary. $\sqrt{R}$ is the square root of the measurement covariance matrix. Since R here is a known constant 1×1, it is calculated by simply taking the square root of R such that $\sqrt{R} = \sigma_R$.

Kalman Gain matrix becomes:

$$W(k) = \left(\sqrt{S}^{-T} \sqrt{S}^{-1} H \bar{L}(k) \bar{L}^T(k) \right)^T \tag{3.26}$$

The updated square root matrix of the state estimation error covariance is calculated similarly to $\sqrt{S}$ with the QR factorization of a second augment matrix:

$$\begin{bmatrix} O_2 & U_2 \end{bmatrix} = \text{qr}\left(\begin{bmatrix} \left(\left(I_{6\times 6} - W(k)H(k) \right) \bar{L}(k) \right)^T \\ \left(W(k)\sqrt{R} \right)^T \end{bmatrix} \right) \tag{3.27}$$

Again, the orthogonal matrix, O_2 is ignored and the upper-triangular matrix, U_2, becomes $L(k)$. The diagonal elements of $L(k)$ must also be positive so the same check and manipulations are applied here as for $\sqrt{S}(k)$. Then, the state estimate update equation here is the

same as in the EKF (Eqn. 3.22).

Now, $\hat{\boldsymbol{x}}(k)$ and $L(k)$ are the updated state estimate for $\hat{\boldsymbol{X}}_{\text{sent}}$ and L_{sent}, which will replace the previous state estimate, $\boldsymbol{X}_{\text{estimate}}(k)$, at the current time step, $k = k_{\text{sent}}$ in the simulation. If necessary, the state error covariance matrix can be found using $P_{\text{sent}} = L_{\text{sent}} L_{\text{sent}}^T$. The code will then propagate forward until the next scheduled measurement or correction maneuver.

3.7 Trajectory Control

The simulations ran to analyze the performance of the measurement model and state estimation algorithms do not include any state control. Instead, the assumption is made that the spacecraft has the ability to accurately control its orbit with respect to the ideal states and follow the reference trajectory. In the code, this is accomplished by setting the true states equal to the reference and not adding process noise to the true state vector. Here the reference and true trajectory are identical and the true states do not drift over time. This is done to evaluate the state estimation performance without introducing errors or complications from implementing a controller. Future work can include pairing this navigation method with different state feedback control schemes and evaluate the feasibility and performance.

3.8 Verification

Given that the simulation code base was created from scratch, it is important to verify that the models are correct and the results generated are valid. The JPL Database, [5], served as the main resource for verifying calculations. Libration point locations and non-dimensional system parameters found in the code were consistent with the values listed on the database. Additionally, the initial conditions solver, dynamics models, and state propagation were

verified with the database by comparing specific orbits. Propagated orbit states are also available in the database which were downloaded and matched with the simulation output for the same initial conditions. Finite difference approximations were used to check Jacobian matrices in the dynamics and measurement models. The navigation algorithms were tested two main ways. A pseudo GPS measurement update was temporarily implemented in place of the derived laser ranging measurement model, which provided a full position and velocity state update similar to how actual GPS does. This allowed to test the functionality of the estimation algorithm itself by isolating any potential errors and performance issues from the laser ranging measurement model. Another method used was to implement two filters, an EKF and a SRF. The performance between the two filters is generally similar which allowed for comparison of results and identification of any anomalous behavior. Lastly, the simulation generates numerous plots of different performance metrics and other qualitative graphics help diagnose any issues that may arise.

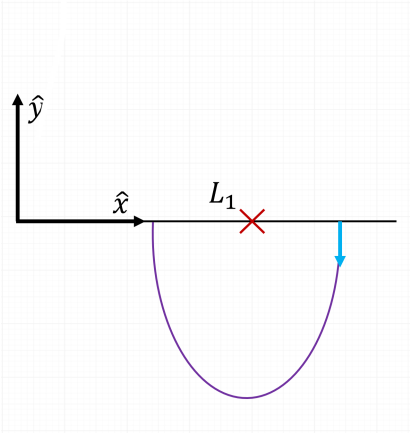

(a) Single shot of the first stage: initial guess of the periodic initial conditions (blue arrow) gets propagated to the first $x-z$ plane crossing (purple).

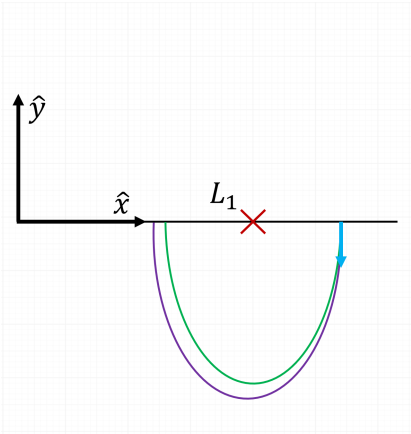

(b) Single shot of the first stage (purple) and adjusted initial guess propagated to the first $x-z$ plane crossing (green).

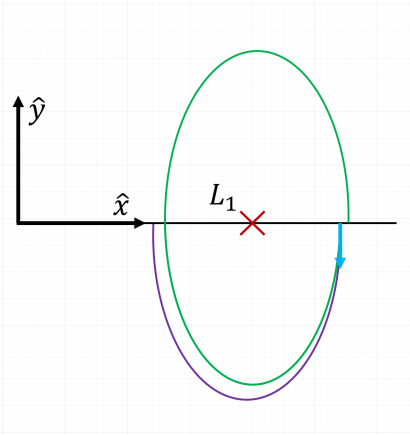

(c) Single shot of the second stage: adjusted initial guess gets propagated until the second $x-z$ plane crossing (green).

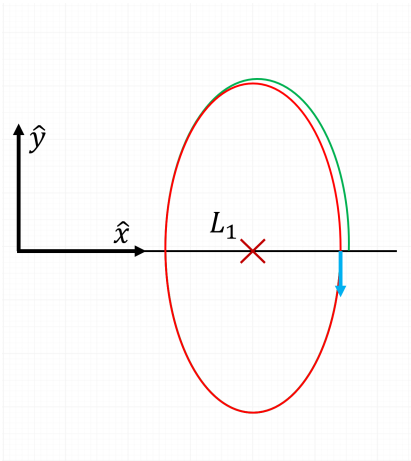

(d) Twice corrected initial guess gets propagated for a full period, giving the periodic solution (red).

Figure 3.1: Two-stage single shooting correction method broken up into individual stages and the resulting periodic solution.

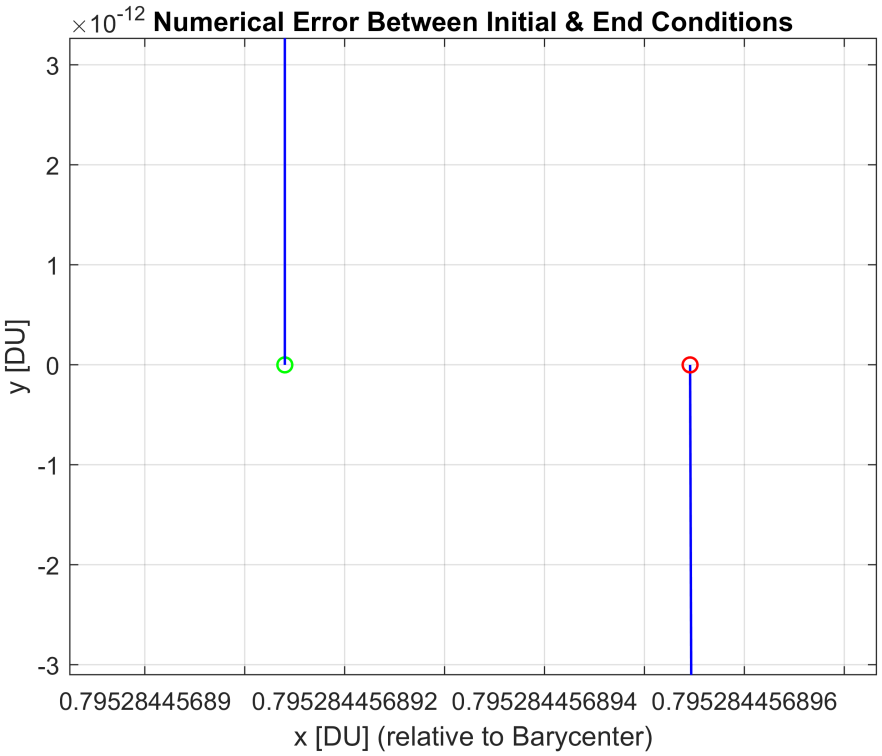

Figure 3.2: Example of numerical error between starting and ending conditions of a periodic solution. The offset is about 1.6 mm.

Chapter 4

Results

To analyze the performance of laser ranging to LRRR for navigating in cislunar space, a baseline halo orbit and simulation parameters are used for comparison in different studies conducted. The orbit initial conditions are given in values are listed in Section 2.2.2 and the simulation inputs are listed in Table 3.1. These values were used in for simulating spacecraft trajectories and evaluating results unless otherwise specified.

For the baseline halo orbit, the typical outcome where the estimator successfully estimates the true trajectory is illustrated in Figure 4.1. The three-dimensional halo orbit about L_1, marked by the red "X" is defined by the initial condition, marked by the red circle, and the blue line which represents the true states, which are the same as the ideal or reference states. The dashed green line represents the estimated states from the estimator. On the contrary, when the estimator is unsuccessful in estimating the true spacecraft states, the green line diverges from the blue line as shown in Figure 4.2 for an NHRO orbit.

One of the two metrics used for distinguishing between varying levels of success and com-

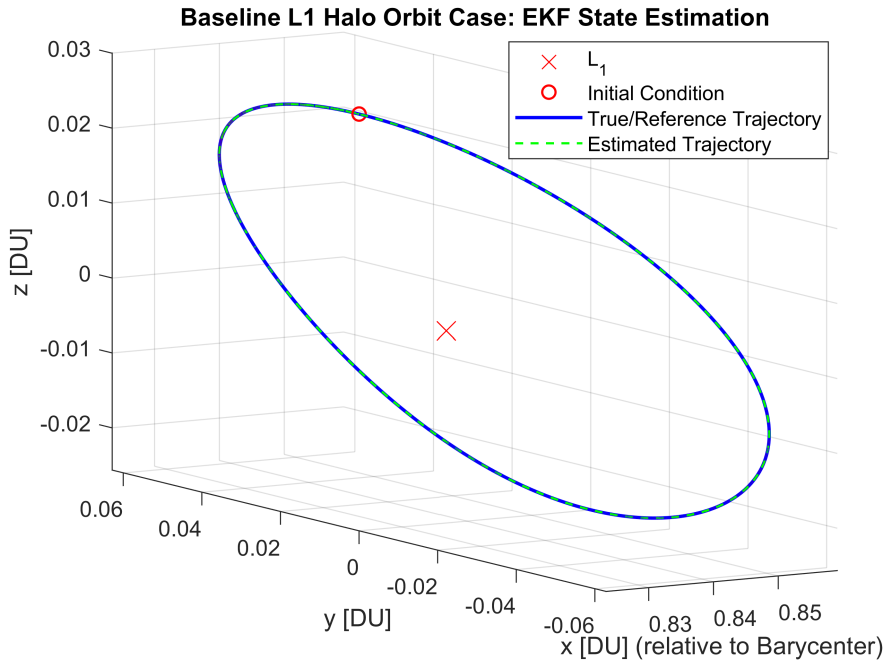

Figure 4.1: The EKF estimate of the true baseline halo trajectory.

paring performance is the actual position and velocity error, given by:

$$\boldsymbol{e}_{\boldsymbol{r},\text{actual}} = \boldsymbol{r}_{\text{estimate}} - \boldsymbol{r}_{\text{true}} \tag{4.1}$$

$$e_{\boldsymbol{r},\text{actual}} = \|\boldsymbol{r}_{\text{estimate}} - \boldsymbol{r}_{\text{true}}\|_2 \tag{4.2}$$

$$\boldsymbol{e}_{\boldsymbol{v},\text{actual}} = \boldsymbol{v}_{\text{estimate}} - \boldsymbol{v}_{\text{true}} \tag{4.3}$$

$$e_{\boldsymbol{v},\text{actual}} = \|\boldsymbol{v}_{\text{estimate}} - \boldsymbol{v}_{\text{true}}\|_2 \tag{4.4}$$

The actual error is then averaged over the period of the second orbit of the simulation. This metric was chosen because it represents the true deviation between the estimated and truth states. The second metric used is the “expected” error a metric which comes from the state

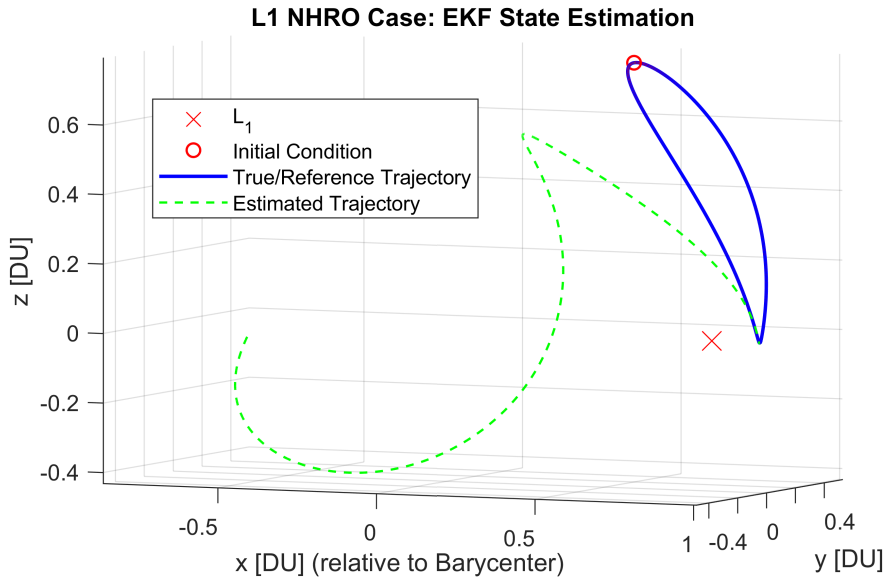

Figure 4.2: The EKF estimate of the true NHRO trajectory, diverging after a half orbit period.

estimation error covariance matrix, defined by:

$$\tilde{e}_{\boldsymbol{r},\text{expected}} = \sqrt{\mathbb{E}\left[x^2 + y^2 + z^2\right]} = \sqrt{\text{trace}\left(P_{\mathbf{rr}}\right)} \tag{4.5}$$

$$\tilde{e}_{\boldsymbol{v},\text{expected}} = \sqrt{\mathbb{E}\left[\dot{x}^2 + \dot{y}^2 + \dot{z}^2\right]} = \sqrt{\text{trace}\left(P_{\mathbf{vv}}\right)} \tag{4.6}$$

where $P_{\mathbf{rr}}$ is the upper right 3×3 of the state estimation error covariance matrix and $P_{\mathbf{vv}}$ is the lower left 3×3. This metric is an approximation of the actual expected error given by:

$$e_{\boldsymbol{r},\text{expected}} = \mathbb{E}\left[\sqrt{x^2 + y^2 + z^2}\right] \tag{4.7}$$

$$e_{\boldsymbol{v},\text{expected}} = \mathbb{E}\left[\sqrt{\dot{x}^2 + \dot{y}^2 + \dot{z}^2}\right] \tag{4.8}$$

This metric gives insight into the estimator's "confidence" of the update it provided. In other words, expected error is an indicator of how accurate the estimator (EKF or SRF) "thinks" its state estimates are. This is important because the confidence level comes from the

covariance matrix which dictates whether the updated state estimate will rely more heavily on the actual measurement, $\boldsymbol{z}$, or the anticipated measurement, $\bar{\boldsymbol{z}}$. The results presented in this thesis use the approximation: $\tilde{e}_{\boldsymbol{r},\text{expected}} \approx e_{\boldsymbol{r},\text{expected}}$ and $\tilde{e}_{\boldsymbol{v},\text{expected}} \approx e_{\boldsymbol{v},\text{expected}}$.

Both of these error quantities are averaged over the period of second orbit of the simulation. At this point in the simulation, the large initial errors at the beginning of the simulation from estimating the spacecraft states with insufficient information from only a few measurements have mostly dampened out and the filters start to converge to a steady state error. An example of the error behavior over time is illustrated in Figures 4.3 and 4.4. Both plots show the error between the EKF estimated position states and the true position states for the 7th test case in the cycling LRRR targets study (targets cycled every 25 measurements).

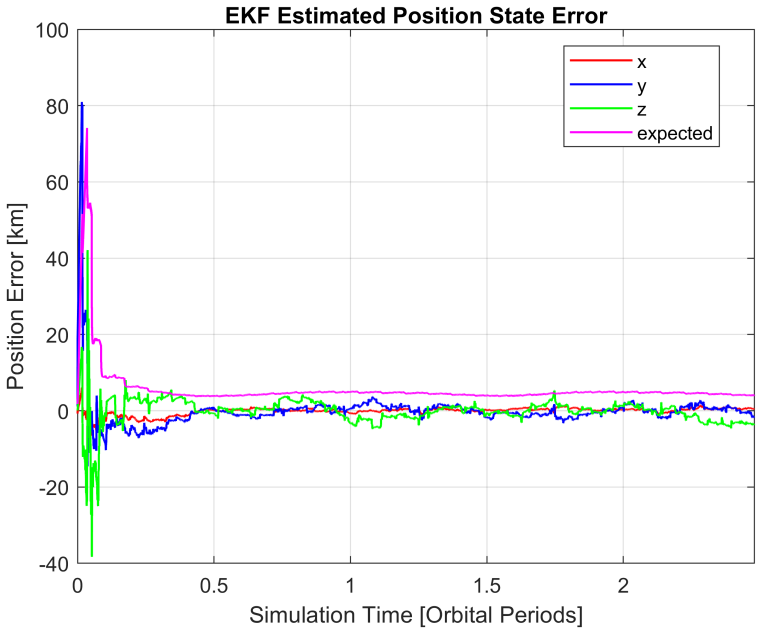

Figure 4.3: Error in estimated position states versus time.

The red, blue and green lines represent the actual error in position or velocity components while the pink line is the 2-norm of the expected position or velocity error. In both plots, we

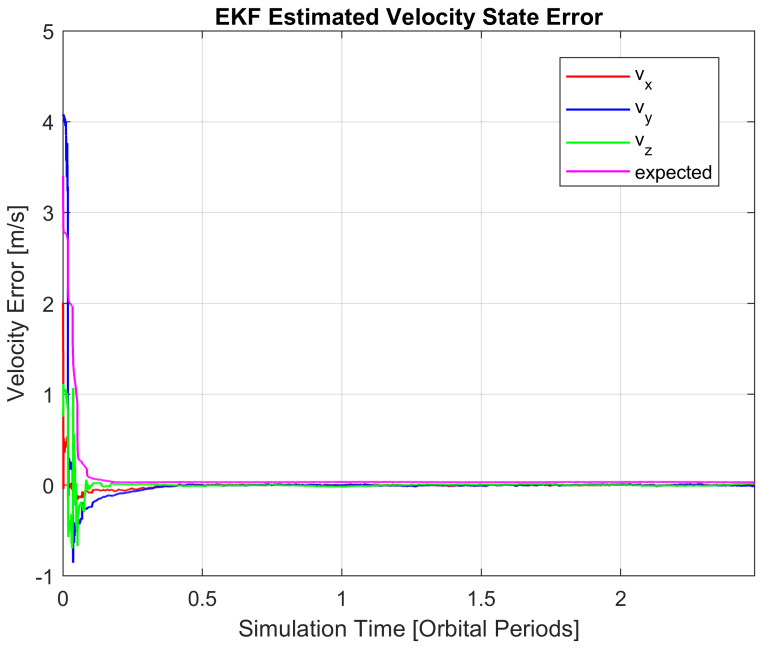

Figure 4.4: Error in estimated velocity states versus time.

can see that most of the initial spikes in error have settled out by the end of the first period. In many of the studies conducted in this section, the error shown between the periods one and two is averaged for comparing the resulting estimation performance. Note that these plots are not shown for each filter in every test case of each study because the differences in the plots from case to case may not provide significant insight or additional information to discuss. Rather, they are shown here to demonstrate how error typically changes over time and give some context as to why the performance metrics were chosen. For similar reasons, only the EKF results were shown in the example plots.

The discrepancy in accuracy between position and velocity estimates is because of the relative size of the units. Nondimesional units, DU and DU/TU are similarly scaled in context of spacecraft states in the dynamics of the CR3BP. On the other hand, kilometers and kilometers per second are not; however, they are more intuitive. For example, in a halo orbit, 1 km is not a large position error, however 1 km/s is a significant velocity error. The

distance covered by halo and Lyapunov orbits is also typically much larger than the change in velocity over the same orbit. Therefore, the estimation error for velocity relative to position will naturally be small because the value of the quantity being estimated is also small. Additionally, velocity errors in the present have implications in future states such that it is representative of how position error will change over time. The consequence of large estimation errors in velocity is much greater than estimation errors in position because they compound over time. Furthermore, the time span of many of the orbits in cislunar space are on the order of weeks. During these long simulation times, even small velocity errors grow into much larger errors, especially in the unstable regions of the collinear libration points. Thus, the velocity estimation error will be much smaller than the position errors.

4.1 Measurement Targets

A spacecraft orbiting L_1 making ranging measurements to LRRR has five different possible targets to chose from. For the baseline orbit, the navigation method was tested with ranging to the same LRRR for all of the measurements and also with selecting a different LRRR after some number of measurements. The progression of switching LRRR follows: A11 $\rightarrow$ A14 $\rightarrow$ A15 $\rightarrow$ L17 $\rightarrow$ L21 then from L21 $\rightarrow$ A11 and the cycle repeats. If an orbit does not have access to all LRRR over its trajectory, any inaccessible LRRR will be skipped in the cycle and reevaluated at the next target change. Furthermore, if a spacecraft does not have access to any of the LRRR at the current measurement update time step, the simulation will skip the update and proceed as if one was not scheduled. While not applicable for the baseline halo or other cases with full visibility, in later sections, accessibility to LRRR throughout an orbit will become important. Two groups of test cases in this study are simulated. The first group holds the target LRRR constant over the simulation for each of five LRRR. The

second group cycles the target LRRR and varies the frequency at which they are changed. The average error in estimated states during the second orbit is plotted for the first group of test cases in Figures 4.5 and 4.6. The target cycling group of test cases are plotted in Figures 4.7 and 4.8.

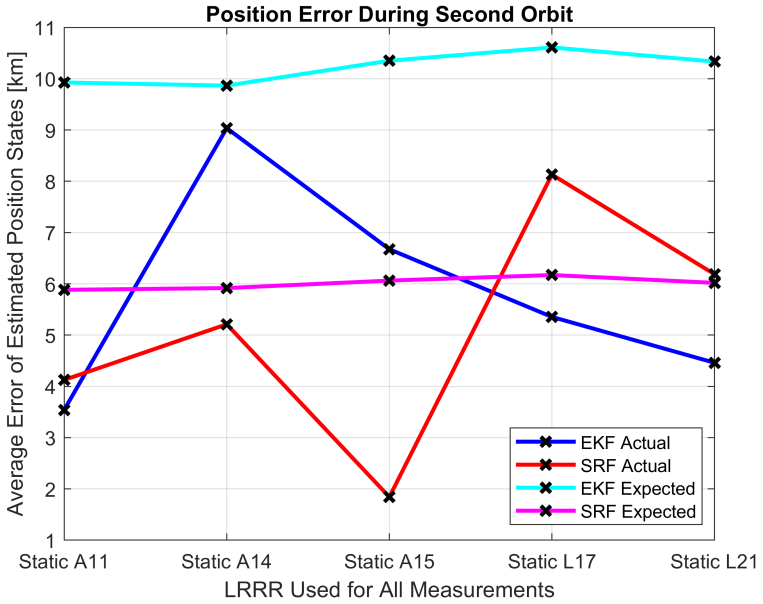

Figure 4.5: Average position estimation error when ranging to different static LRRR targets.

Looking at Figures 4.5 and 4.6, there are a few main results to point out. The actual error is much more variable between different LRRR targets than the expected error and shows that ranging to certain LRRR over others appears to provide more accurate state estimates. Random measurement noise error directly influences the estimated states which are used to calculate the actual error. Therefore, the actual error is sensitive to measurement noise and the corresponding data points vary with each simulation run. This causes the actual error to appear more noise-like where the data points do not always present a clear trend indicating how changing certain parameters affect estimation error. The expected error data points do not display this same behavior because they are not dependent on specific values of random measurement noise. Rather, the error is more consistent across the different LRRR targets.

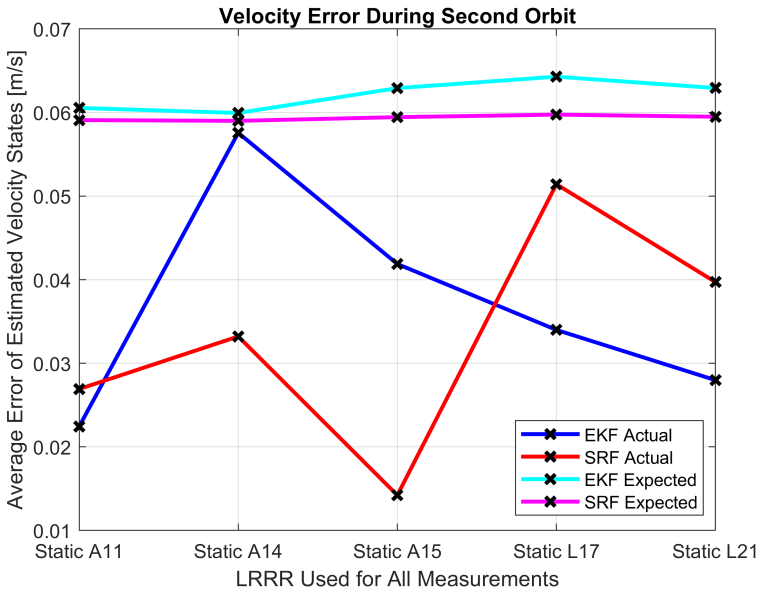

Figure 4.6: Average velocity estimation error when ranging to different static LRRR targets.

This is more in line with the expectation that accuracy should not change significantly when using one LRRR over another. The minor changes in expected error when ranging to different LRRR may come from reflectors like Apollo 11 and Apollo 14 being installed at more optimal locations for ranging measurements.

Aside from the trends shown, there is also a general discrepancy in the amount of error between actual and expected. This is more evident when looking at the velocity error (Fig. 4.6). The actual error being smaller is a consequence of the ideal control assumption made in Section 3.7. The spacecraft is following an ideal, predictable trajectory and the states are not influenced by process noise which would normally affect the actual error. When the spacecraft follows the reference periodic orbit perfectly, the estimated states are very accurate such that the filter's anticipated measurement and the *a priori* state estimate are very close to the actual measurement and *a posteriori* state estimate. This is true even in the absence of measurement updates which will be discussed in Section 4.3. On the other hand, the expected error comes from the state estimation error covariance which is only a

function of the measurement model and measurement accuracy, not the actual states. This means the expected error is not affected by the ideal control assumption or the noise added to each individual measurement. Since these characteristics of the simulated data consistent across all of the estimation error results in this section, more emphasis should be placed on the expected error. This performance metric provides a more realistic representation of the true trends and behaviors that the spacecraft state estimator will experience, even when not following an ideal trajectory.

Running a Monte Carlo simulation would be useful in averaging out the variability in the actual errors, but the it is anticipated that some discrepancy between expected and actual error would remain. To address this, a spacecraft state controller would need to be implemented in the simulation in order to relax the ideal control assumption. The assumption is used here because fixing the true states to follow the reference trajectory helps isolate the estimator performance with this measurement model by eliminating added complexity and influences from simulating navigation and control algorithms in tandem.

There is also some disagreement between the EKF and SRF in the simulated error data. This is expected as they differ in how each handles numerical error and rounding. In general, the SRF should be more accurate over the EKF. However, the expected errors represent how well the estimator thinks it is performing which may not always perfectly represent the actual estimation performance.

Figures 4.7 and 4.8 give the error of the estimated position and velocity for different rates of cycling target LRRR. Again in these plots, the actual error does not reveal a conclusive trend and the actual error appears to be smaller across the test cases than the expected error. Looking at both sets of figures for cycling and static targets, the cycling test cases outperformed the static test cases in enabling the estimator to more accurately estimate the spacecraft states. Also for both cycling and non-cycling LRRR targets, the expected error

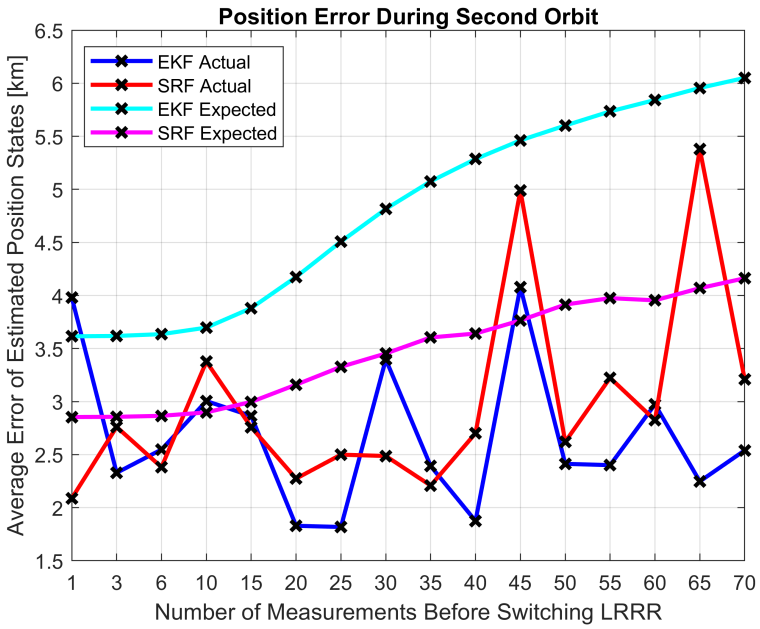

Figure 4.7: Average position estimation error when ranging to cycling LRRR targets.

matches the expected outcome of changing targets. It makes sense that using one LRRR over another for all of the measurements does not have much of an effect on estimation error. It also makes sense that frequently changing the measurement target allows for more accurate state estimation while error grows as the target is switched less often.

This expectation comes from considering the geometry of the problem. L_1 is roughly 57 000 km from the lunar surface while each of the LRRR are separated from each other by less than 1900 km. This gives an angular separation of the LRRR from L_1 of less than 4°. This means that the "bulk" of the measured Δt comes from the laser pulse traveling along the line of sight from L_1 to the Moon, and a small amount of the measured Δt comes from the distance traveled by the laser in the off-line of sight direction. Although angular separation is not large, it is enough to provide some amount of new information that can be used by the filter to improve the state estimate. The bulk of the measurement is approximately the same for a laser pulse returned from each LRRR since the distance between L_1 and the Moon make up the majority of the total distance that the reflected pulse covers. The new

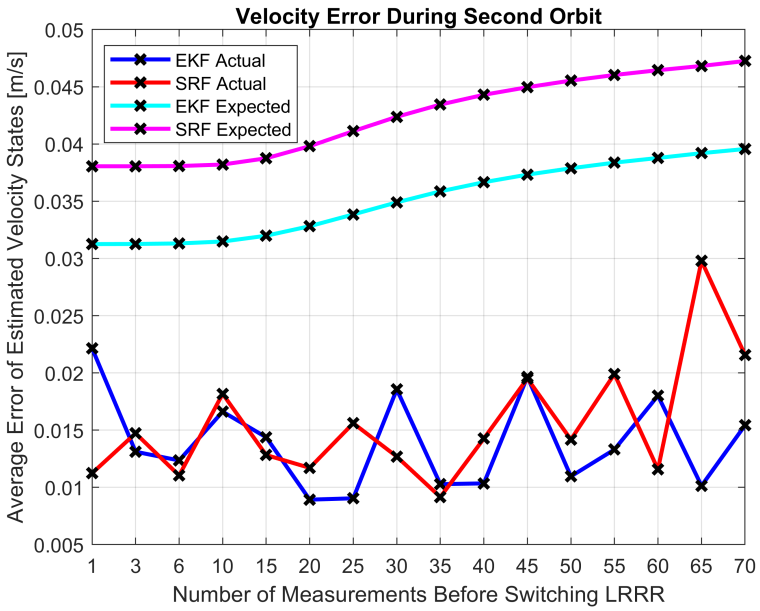

Figure 4.8: Average velocity estimation error when ranging to cycling LRRR targets.

information comes from the portion of the time delay where the light travels in the direction perpendicular to the line of sight between L_1 and the Moon.

Additionally, the expected error data points show that the SRF generally provides more precise results over the EKF. This is also expected because the square root filter is designed to be an improvement of the original Kalman filter in that it is better suited to produce results with higher numerical accuracy. The position and velocity errors follow a similar curve in both sets of plots, however, both the EKF and SRF estimate the velocity states much more accurately than the position states. This is due to the same reasons as described at the beginning of this chapter.

In effort to explore the upper accuracy limit of this navigation method, the following simulated results will employ switching LRRR targets after each measurement. This design choice may not be reasonable or feasible for a spacecraft depending on the control authority and how the spacecraft will handle pointing the laser and receiver towards the LRRR. If the laser or receiver pointing directions are fixed to the spacecraft body, this may require

immense attitude control effort and cycling LRRR less often may make more sense. Other configurations may consider a gimbal design where the transmitter and receiver are able to be directed independently of the spacecraft attitude; similar to pivoting solar panels for Sun tracking.

4.2 Measurement Accuracy

The accuracy of the position estimate is also heavily dependent on the accuracy of the time of flight measurement of the laser pulses. It is important to consider how the state estimation error changes as a function of measurement error. Because of how the measurement error covariance matrix is defined, the magnitude of the calculated measurement noise, is determined by the standard deviation of the measurement error, σ_R. Therefore, the effect of the measurement error on state estimation can be observed by running simulations of the baseline orbit case with test case values of σ_R: 2×10^{-5} s, 2 µs, 2×10^{-7} s, 2×10^{-8} s, and 2 ns. Based on the results of the previous study, the target LRRR will be changed after every measurement in these simulations. Figure 4.9 shows that the actual and expected position estimation error decreases as the standard deviation of measurement error decreases as anticipated. Similarly, in Figure 4.10, the velocity estimation error begins to decrease as σ_R gets smaller until $\sigma_R = 2 \times 10^{-8}$ s. Beyond this point, the actual velocity error for both EKF and SRF begin to grow, while the expected error continues to decrease. It is suspected that numerical error takes over in the actual error when σ_R is smaller than 2×10^{-7} s. This data shows that smaller measurement errors contribute to more accurate state estimations, however, even with larger measurement errors, this navigation method is still able to provide accurate state estimates. This is an important result for considering this navigation method on a future mission. In the event that there is a degradation in laser transmitter performance

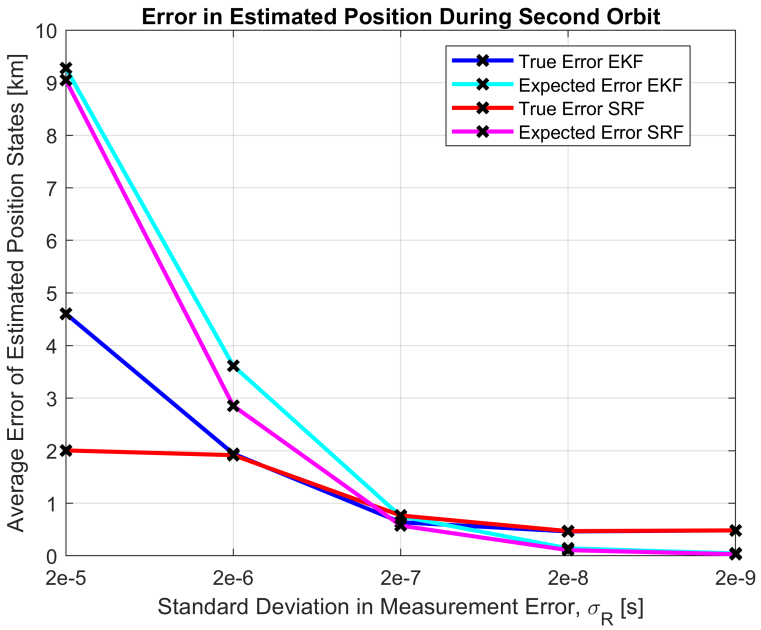

Figure 4.9: Average magnitude of expected and true error in estimated position states for different measurement errors.

or power output, the method is resilient in that it will still allow the spacecraft to determine its position and velocity some reduction in measurement accuracy. Additionally, the LRRR themselves are robust as they have been used for more than 50 years and are still operational.

For the remaining simulation results presented in this chapter, $\sigma_R = 2 \times 10^{-7}$ s will be used in place of the previously used $\sigma_R = 2 \times 10^{-6}$ s. This is still a reasonable assumption as it is two orders of magnitude less than the ground stations' ranging accuracy. A 2×10^{-7} s standard deviation in measurement error should be achievable for a future instrument package onboard a spacecraft. In addition to sub-kilometer position estimation accuracy, using $\sigma_R = 2 \times 10^{-7}$ s also avoids numerical instability in the simulation software.

An important note to make here is that changing the measurement accuracy has a similar affect as changing the measurement frequency. For example, doubling the measurement frequency is the same as halving the measurement error variance. Instead of running additional test cases to determine the impact of measuring less or more often, the consequence

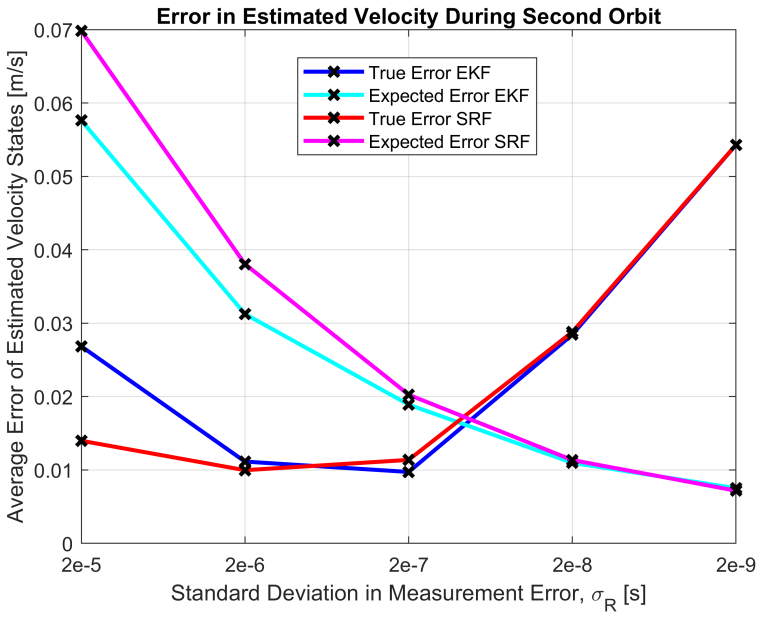

Figure 4.10: Average magnitude of expected and true velocity error in estimated states for different measurement errors.

of changing the measurement frequency is also captured in Figures 4.9 and 4.10.

4.3 LRRR Visibility

Another critical attribute of this navigation method that needs to be investigated is how well it applies to different orbits. The amount of access a spacecraft has to any of the LRRR over the course of a periodic orbit is plotted in Figure 4.11 for the Lyapunov family, and Figure 4.12 for the halo family. The portions of each orbit plotted in green indicate that range measurements to at least one LRRR are possible at that those points in the orbit. The positions in the green sections of the orbits fall within the LRRR field of view necessary in order for a reflected a laser pulse to return to the spacecraft. The portions plotted in red indicate that the spacecraft is unable to make a range measurement. At these points, a reflected laser pulse would not be visible to the spacecraft because its position is outside of

the conical 45 degree field of view, that is aligned with the normal direction of the LRRR array. This means that a spacecraft does not receive a measurement update during these sections of its orbit. The *a priori* state estimate at the current time step is propagated just like for time steps without measurement updates. The restricted field of view was assumed to be a geometric constraint of the corer reflectors that make up the LRRR.

A more quantitative way of looking at the visibility data is by plotting the percentage of an orbital period with measurement visibility versus a unique identifying parameter for each family of orbits. Specific orbits in the Lyapunov family are best distinguished by the initial x component of position, used in Figure 4.13. For the halo family, this parameter is the maximum z position component, or z amplitude of the halo orbit, used in Figure 4.14.

Figure 4.13 shows that access to LRRR for the L_1 Lyapunov family declines as the x initial condition is moved further from the libration point. Equivalently, access to LRRR generally declines for larger Lyapunov orbits which is illustrated in Figure 4.11. However, the curve shown in Figure 4.13 flattens out around 15%. This is because the size of the Lyapunov orbits grows proportionally to the amount of the orbit that lies within the 45° visibility field of the LRRR where laser ranging measurements are possible.

The curve shown in Figure 4.14 focuses on the limited subset of the L_1 halo family where the changes in LRRR access occur. The end behaviors of the curve are consistent for halos with z amplitudes beyond the portion of the family shown.

Figures 4.15 and 4.16 show the affect of losing access to LRRR on the performance of the SRF state estimator. During the non shaded blue regions of these plots, laser ranging measurements are unable to be made because the reflected pulse would not be visible to the spacecraft. Also in these regions, it is shown that the actual and expected error grow in the absence of measurement updates.

From the plots in Figures 4.13 and 4.14, 17 Lyapunov orbits and 18 halo orbits were selected as test cases and simulated to analyze the loss of LRRR access on the performance of the navigation method. The test cases were chosen to evenly sample LRRR visibility, however, orbits with less than 20% visibility were not included in the study as the resulting in errors are not practical for most spacecraft missions.

The subset of the L_1 Lyapunov family that has LRRR access for more than than 20% of the period include orbits with an initial x position component less than 0.812 46 DU (316 618 km). The initial conditions for the test cases used and their corresponding LRRR access percentage are listed in Table 4.1. The average error over the second orbit are plotted in Figures 4.17 and 4.18.

Table 4.1: Non-dimensional initial conditions for Lyapunov orbit test cases.

Case	x_0 (DU)	$\dot{y}_0$ (DU/TU)	Visibility
1	0.7513892778556	0.5246320354426	100 %
2	0.7771014202841	0.4576118429060	95 %
3	0.7887149429886	0.4165243990526	90 %
4	0.7952844568914	0.3856454851716	85 %
5	0.7994918983797	0.3608151962797	80 %
6	0.8024198839768	0.3403078128489	75 %
7	0.8046097219444	0.3229144262602	70 %
8	0.8062828565713	0.3083590519232	65 %
9	0.8075869173835	0.2962580000056	60 %
10	0.8086449289858	0.2859773477935	55 %
11	0.8095061012202	0.2773262218139	50 %
12	0.8101950390078	0.2702384890911	45 %
13	0.8107117423485	0.2648341917636	40 %
14	0.8111054210842	0.2606700498104	35 %
15	0.8113760752150	0.2577855314790	30 %
16	0.8115483096619	0.2559412626194	25 %
17	0.8124586917383	0.2460923697331	20 %

The actual error data in Figures 4.17 and 4.18 show that the position state estimation accuracy is mostly unaffected until LRRR visibility drops below 30%. The actual velocity

error gets smaller as the access to LRRR decreases. Meanwhile, the expected error grows more uniformly as anticipated when measurement target visibility is reduced for both position and velocity. The state error covariance, and consequentially the expected error, grow over time until a measurement update is made. The covariance typically gets smaller after a measurement update because the estimator's confidence in its performance increases when a measurement is used to update the state estimate rather than propagating *a priori* estimate from the previous time step. This is demonstrated in Figures 4.15 and 4.16. Orbits with less visibility limit the amount of measurements that can be made, so the estimator will have an overall lower confidence in its predictions. The error covariance will grow more with fewer measurement updates therefore the expected error should also grow as visibility decreases.

On the contrary, the behavior of the actual error in Figures 4.17 and 4.18 goes against against intuition. It would make sense for the error to increase as there is less access to information. However, this is not the case, and is once again a consequence of the ideal control assumption. Because the spacecraft is following the ideal trajectory in the simulation, there is no process noise error trickling into the true states, which in turn, does not cause any deviation or drifting between the true and estimated states. In other words, random noise is not added to the true states, so the estimator's guess of the truth states is more accurate then expected. Because of the assumption, the estimated states represent the true states more accurately than usual. Under normal circumstances where there is process noise and other disturbances, fewer or less frequent measurements made during an orbit would causes more error to accumulate in the estimated states before it is detected during the next measurement update. However, under the ideal control assumption, error does not accumulate over time, regardless of how often measurements are made. This is why the actual error appears to be minimally affected as the LRRR visibility changes. Therefore, the actual error is smaller than what the estimator expects there to be, and what there would normally be if process

noise was included.

This is also observed in Figures 4.15 and 4.16. The expected error accumulated is much larger and grows faster than the actual error in the non-shaded regions where measurements are unavailable. Additionally, during the first orbit, the growth in actual error is larger than during the second orbit. Once the initial errors at the beginning of the simulation are settled out the estimator does a better job at maintaining accurate state predictions, even when measurement updates are not available. This is due to the ideal control assumption and the lack of random errors that would normally cause the state estimation error to grow more like the expected.

Considering the expected error, Figures 4.17 and 4.18 show that this navigation method can provide a spacecraft with accurate state estimates for a variety of different Lyapunov orbits, even with less than 100% access to LRRR. For orbits with 55% access or better, the navigation method is capable of providing estimates with less than 4.0 km in position error, and 3.0 cm/s in velocity error. For 70% visibility state estimation errors fall below 1.75 km and 2.5 cm/s. If an orbit has 100% visibility to at least one LRRR throughout its orbit, the state estimate errors are below 1.5 km and 2.0 cm/s.

A few halo orbits were sampled from the L_1 family and plotted in Figures 2.5b and 4.12. The corresponding initial conditions for 18 different test cases are listed in Table 4.2 with their respective visibility, as a percentage of orbital period. The test cases are used to test navigation performance in non-optimal conditions and analyze the method's applicability to different halo orbits.

The baseline case and case 1 are halo orbits with full access to at least one LRRR at every point in its trajectory. Case 2 through 17 are increasingly larger halo orbits which lose access to LRRR for some part of the trajectory. Only orbits with access to LRRR for 20% or more

Table 4.2: Non-dimensional initial conditions for halo orbit test cases.

Case	x_0 (DU)	z_0 (DU)	$\dot{y}_0$ (DU/TU)	Visibility
Baseline	0.8234231844314	0.0299810784117	0.1405412786918	100 %
1	0.8271725310488	0.0934432125879	0.2085260810807	100 %
2	0.8289453945292	0.1070349470532	0.2225857722118	95 %
3	0.8289854510712	0.1073141314464	0.2228625563956	90 %
4	0.8290607672409	0.1078362703426	0.2233788042685	85 %
5	0.8291668222942	0.1085654221630	0.2240966485830	80 %
6	0.8292967781290	0.1094494087456	0.2249620619646	75 %
7	0.8294465835990	0.1104558000008	0.2259407378921	70 %
8	0.8295918255063	0.1114189976201	0.2268707713523	65 %
9	0.8297098952135	0.1121931424185	0.2276134961969	60 %
10	0.8297610546680	0.1125261598336	0.2279316791174	55 %
11	0.8302245687223	0.1154157800057	0.2307177418537	50 %
12	0.8309253134635	0.1197366770998	0.2346192157609	45 %
13	0.8317661715021	0.1245436410515	0.2388512240651	40 %
14	0.8327010939360	0.1295306219948	0.2430347131723	35 %
15	0.8336990711063	0.1344635871573	0.2469485113526	30 %
16	0.8346887691181	0.1389770638417	0.2503150669236	25 %
17	0.8356008594457	0.1428173735216	0.2530005598574	20 %

of its orbit were considered. LRRR Visibility for less than 20% of an orbit typically resulted in average errors that were too large for any practical use. This includes any halo orbit with a maximum z position component less than 0.2530 DU (98 595 km). LRRR access for orbits with a z amplitude larger than case 17 continues to decrease to zero. The NHRO sub set of halos falls into this category where they have zero access due to their orientation and proximity to the Moon.

Simulations were ran for each test case and the average error over the second orbit was calculated. Figures 4.19 and 4.20 show the estimated position and velocity error with respect to the true states during the second orbit in the simulation.

Figures 4.19 and 4.20 show that the general trend, given by both actual and expected error data, is that more access yields more accurate state estimation. Similar to the visibility plots

for the Lyapunov orbits, the actual error is smaller than the expected for the same reasons as discussed previously. There is also more variability in the actual error data which comes from the prior discussion on noise sensitivity due to dependencies on spacecraft states.

Between the data points for 100% and 55% access, the expected and actual errors agree and the increase in error for these data points is more gradual. After the case 10 (55%) data point, the expected error trend lines make an abrupt change in slope, where the error increases more for the same incremental changes in visibility.

Figure 4.14 features a similar sharp change in slope around 55% visibility. In this plot, between approximately 0.105 DU and 0.115 DU, the visibility changes more significantly with max z position. Beyond $z_{\max} = 0.113$ DU or 55% visibility, the slope changes and the visibility decreases more gradually as z amplitude increases. This portion of the halo family where visibility changes the most rapidly is also noticeable in Figure 4.12. The halos plotted in this figure are approximately evenly separated in space. Considering the 16 orbits shown in the figure, all of the visibility changes occur in the first 8 halos plotted. The first four halos have LRRR access for most of their periods, then the transition from green to fully red in the following three orbits as z amplitude increases in the plot. The rest of the orbits have zero visibility to the LRRR, so all of the visibility changes occur within the first section of plotted orbits in Figure 4.12, which corresponds to the subset represented in Figure 4.14.

It is suspected that measurements during certain sections of halo orbits are more critical than others. Furthermore, the parts of the halos where access is lost in the baseline through case 10 halos are speculated to be areas where measurement updates are less critical. Similarly, for case 11 and beyond, the orbits begin to lose access in areas where measurement updates are more important. For halos that have less than 55% visibility to LRRR, the portion of the orbits without access begin to overlap with the portions of the orbits where measurement updates are the most critical. This causes the abrupt change in slope of the expected error

shown in Figures 4.19 and 4.20.

The discussion of the Lyapunov visibility results regarding variability and behavior of the actual error compared to the expected error is directly applicable to halos. The performance of the navigation method is also very similar between both orbit families. With spacecraft laser ranging, a spacecraft can navigate in orbits with 55% LRRR visibility and achieve errors less than 5.0 km in position and 5.5 cm/s in velocity. For 70% visibility or better, the errors drop below 2.25 km and 2.5 cm/s. Under the optimal condition, 100% access, it is possible to achieve position accuracies below 1.0 km and 2.0 cm/s.

The presented data for LRRR access in halo obits show that spacecraft laser ranging navigation is capable of providing accurate state estimates, even in halos that do not have visibility to the LRRRs for 100% of the nominal trajectory. Although this method is not effective for the whole halo family, the results show acceptable performance for the subset with LRRR visibility better than 55% or, equivalently, a maximum z position components less than 0.1125 DU.

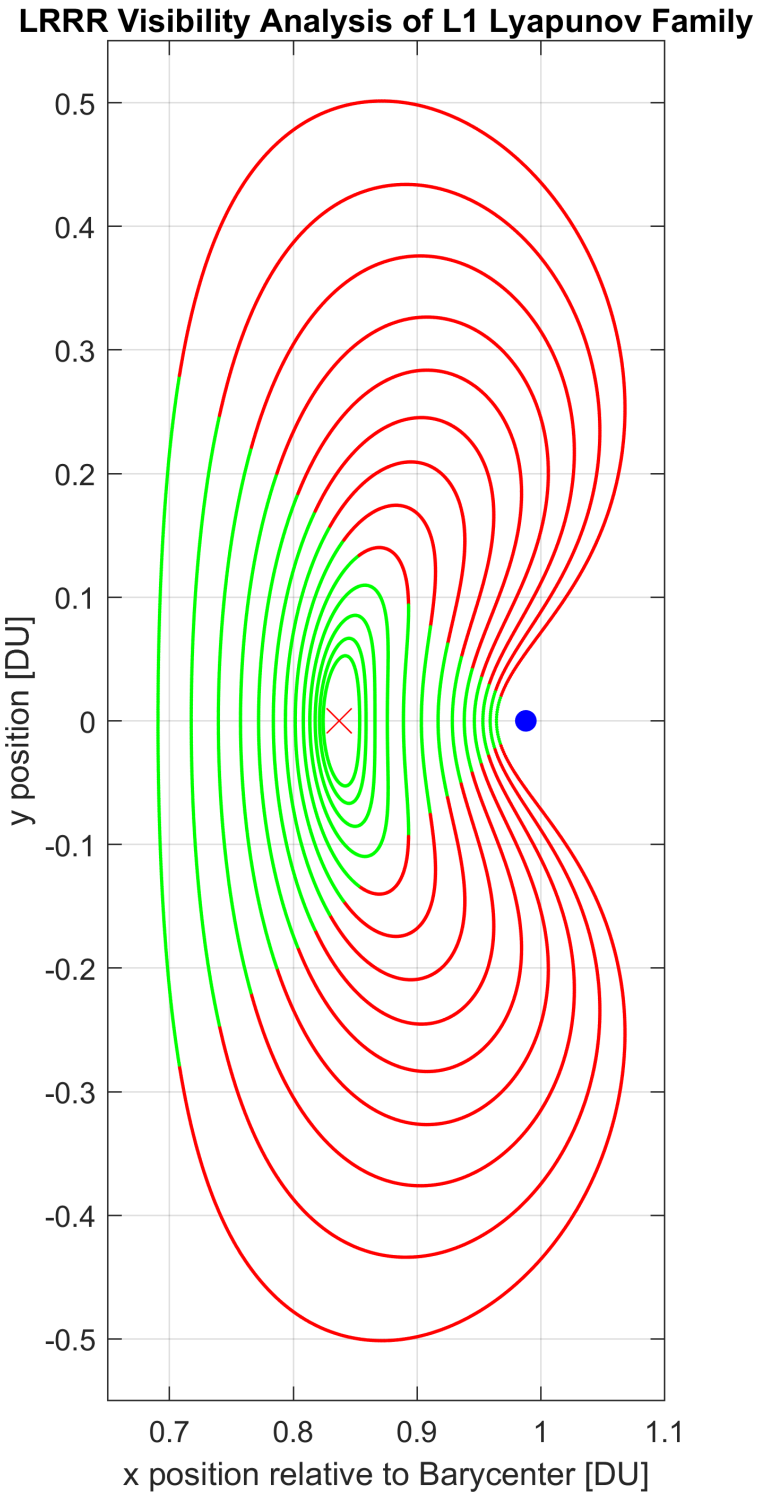

Figure 4.11: LRRR access projected in green on a portion of the L_1 Lyapunov family orbits. Sections of orbit with no access are plotted in red, the Moon is marked in blue, and the red "X" is L_1.

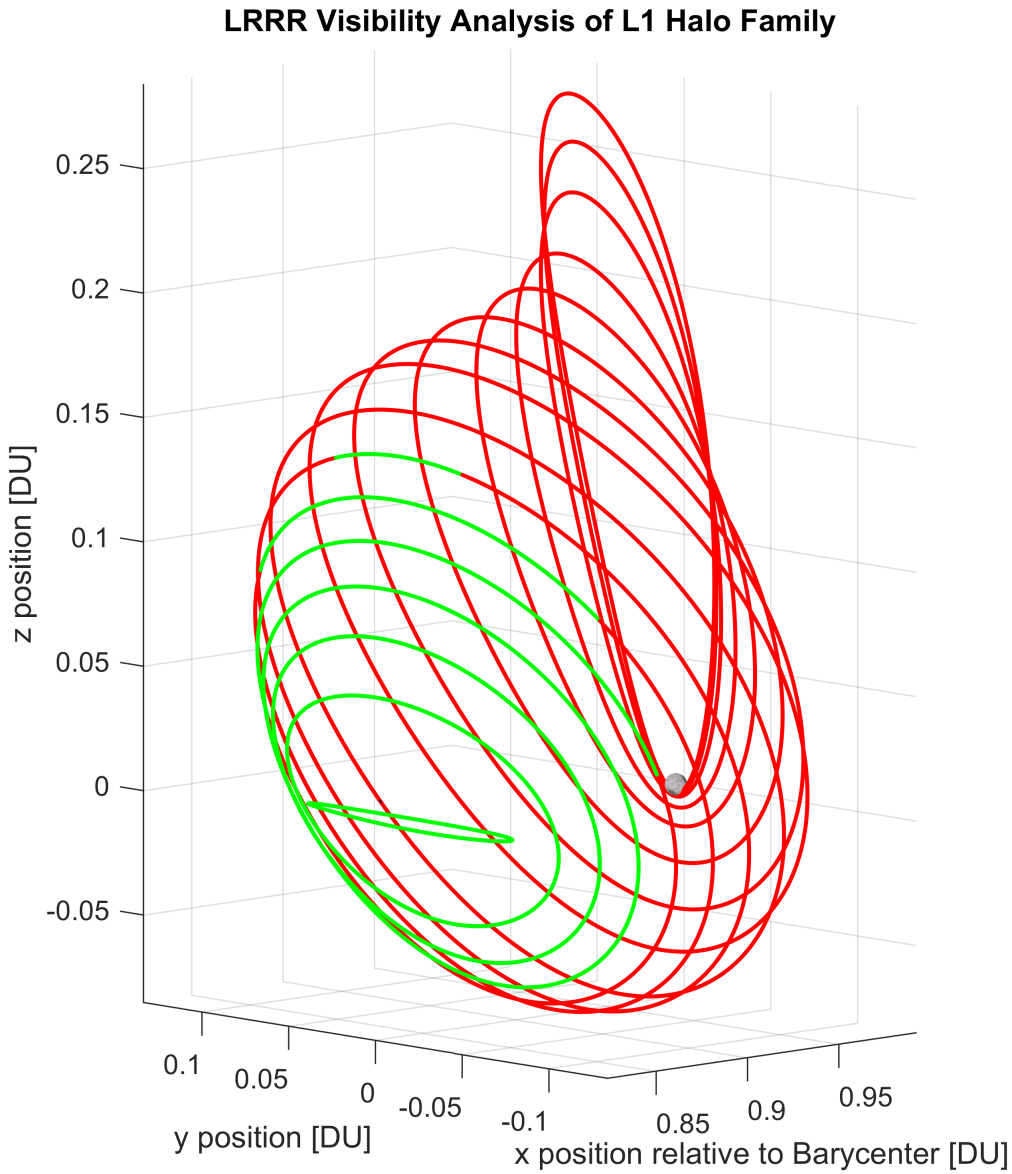

Figure 4.12: LRRR access projected in green on a portion of the L_1 halo family orbits. Sections of orbit with no access are plotted in red, the Moon is marked by the gray sphere, and the red "X" is L_1.

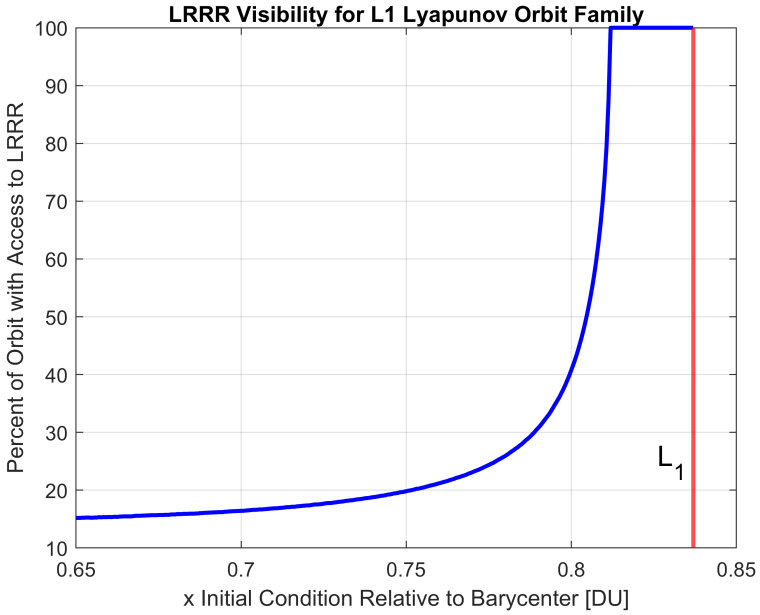

Figure 4.13: Percent of orbital period where laser ranging measurements are available for orbits sampled from the L_1 Lyapunov family.

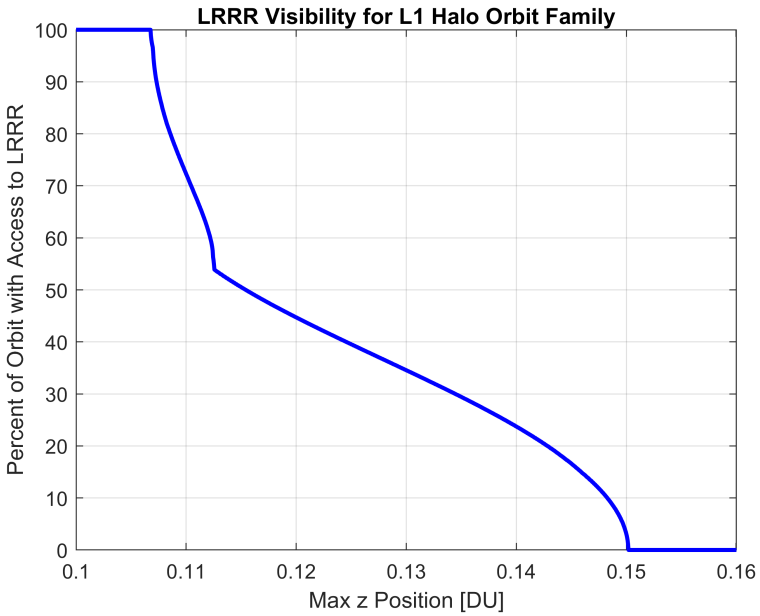

Figure 4.14: Percent of orbital period where laser ranging measurements are available for orbits sampled from the L_1 halo family.

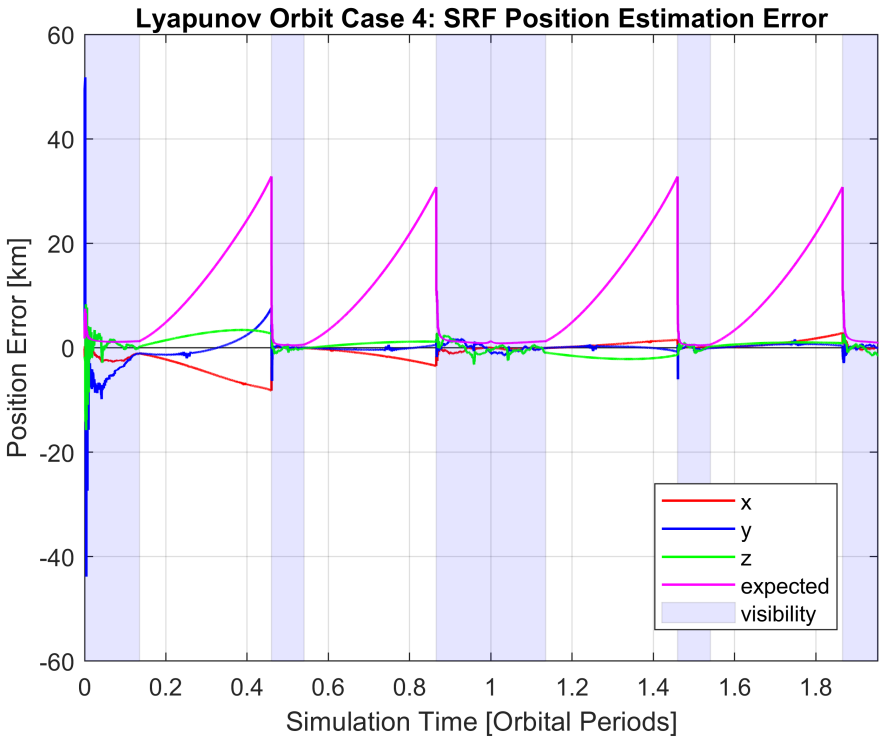

Figure 4.15: SRF position estimation errors over two Lyapunov orbit periods where access to LRRR is lost during parts of the orbit. The light blue highlighted areas of the plot indicate when the spacecraft has access to LRRR and is able to make range measurements.

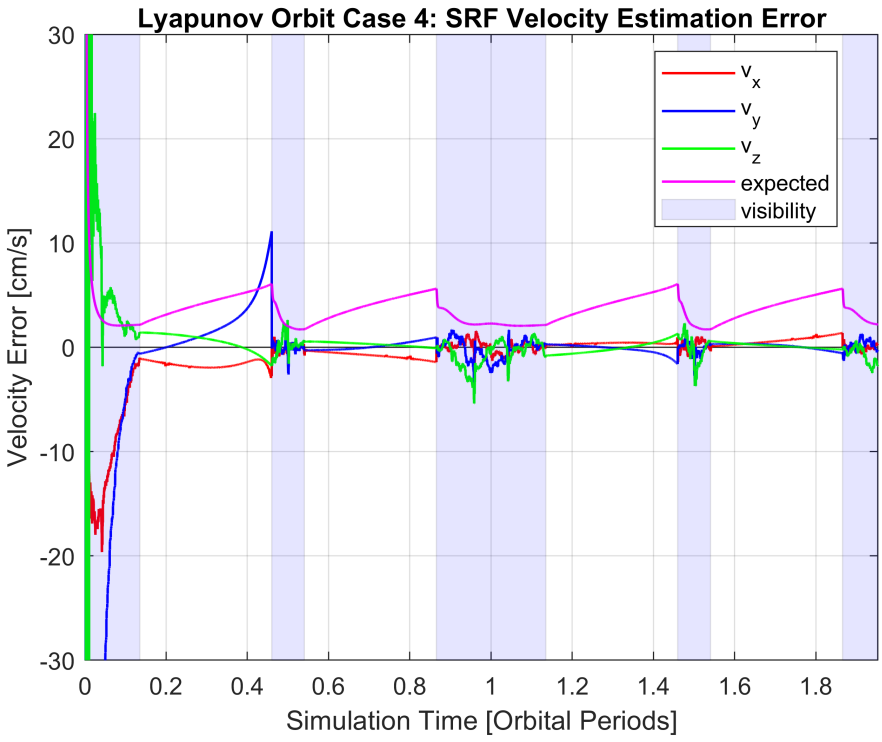

Figure 4.16: SRF velocity estimation errors over two Lyapunov orbit periods where access to LRRR is lost during parts of the orbit. The light blue highlighted areas of the plot indicate when the spacecraft has access to LRRR and is able to make range measurements. Note: the initial spikes in error at the beginning of the simulation are much larger than the bounds of the plot. These sections of data were cut off to zoom in on the error growth during periods of zero LRRR visibility.

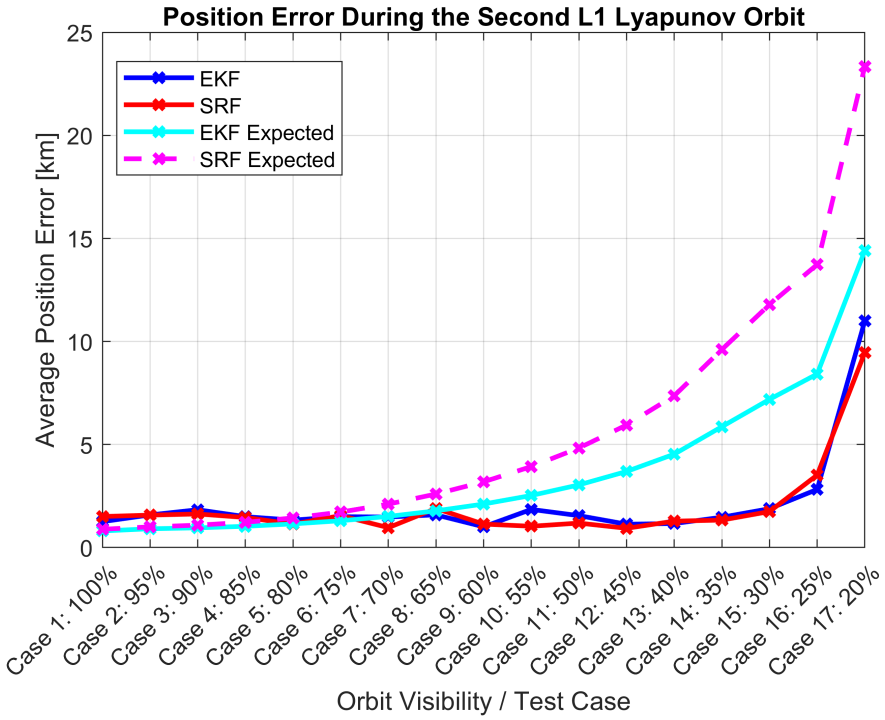

Figure 4.17: Position state estimation error versus access to LRRR during Lyapunov orbits.

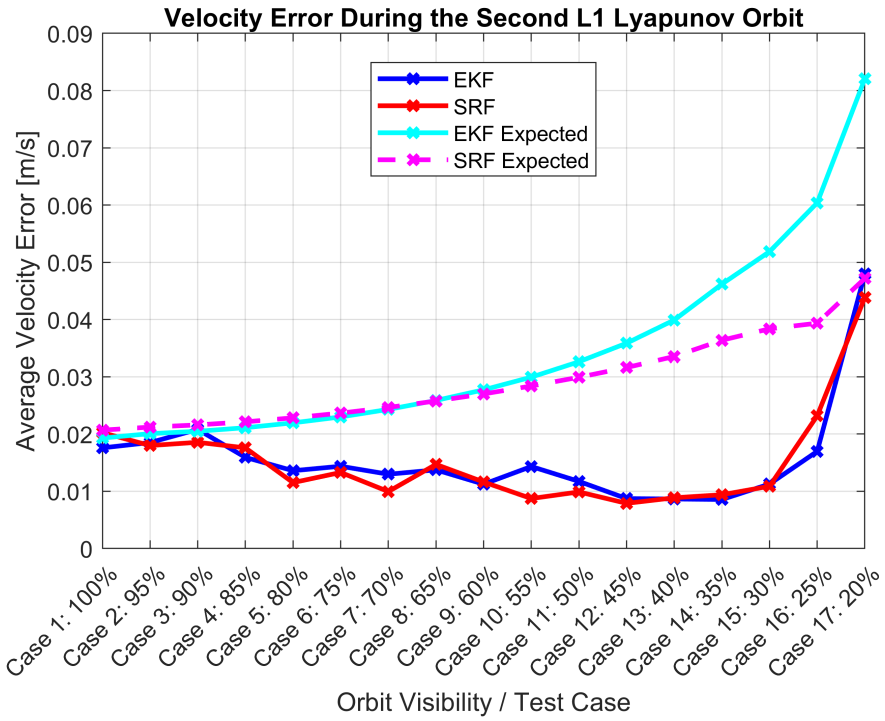

Figure 4.18: Velocity state estimation error versus access to LRRR during Lyapunov orbits.

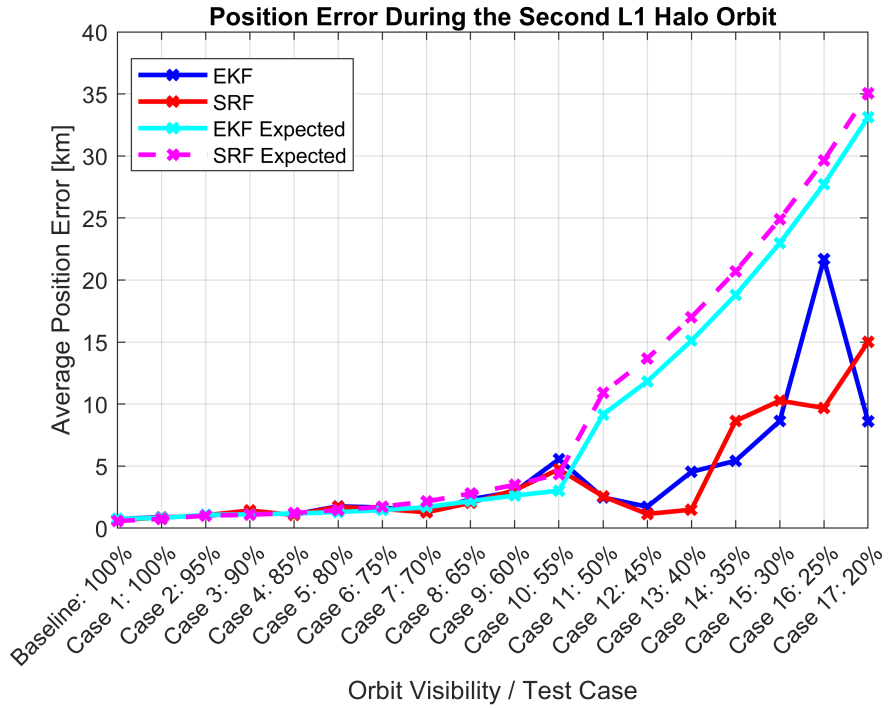

Figure 4.19: Position state estimation error versus access to LRRR during halo orbits.

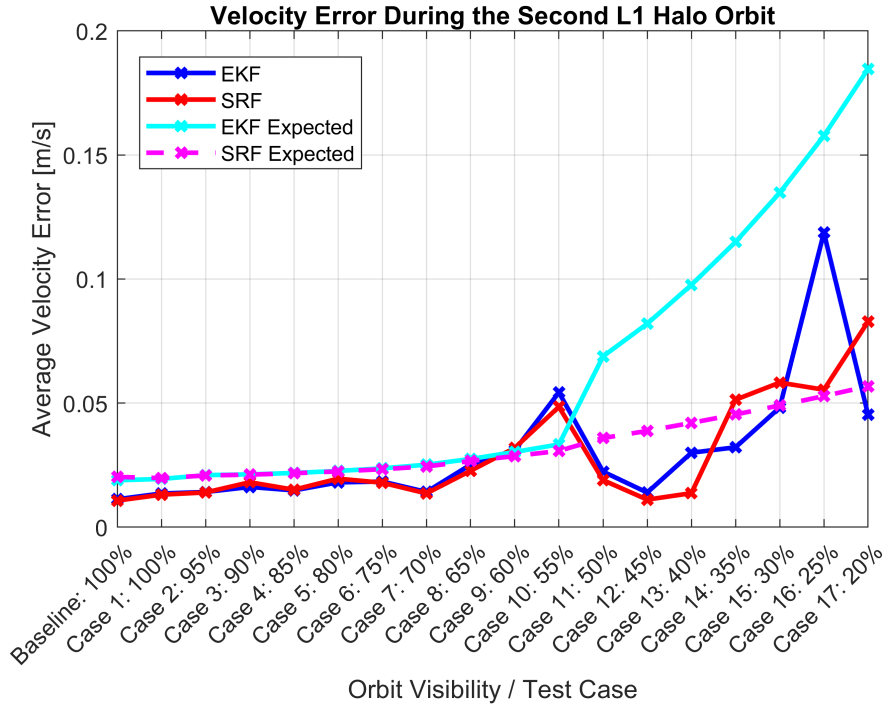

Figure 4.20: Velocity state estimation error versus access to LRRR during halo orbits.

Chapter 5

Conclusions

A new method for autonomous spacecraft navigation in cislunar space was proposed and developed. In order to evaluate the feasibility and analyze the performance of lunar laser ranging for spacecraft navigation in cislunar space, a simulation platform was built in Matlab. The simulation software was designed to test the applicability and feasibility of an estimation algorithm using the developed laser ranging measurement model to estimate a spacecraft trajectories about L_1. 35 different Lyapunov and halo orbits were chosen as test cases due to their historical usage, popularity, and potential for future missions. Simulations with different input parameters were also ran to evaluate and select the best operating conditions for the navigation method. It was found that a measurement error standard deviation of 2×10^{-7} s resulted in the highest accuracy while not exceeding simulation limitations or the realistic capabilities of a future cislunar spacecraft mission. Additionally simulation data showed that cycling the five Lunar ranging retroreflector measurement targets as often as possible resulted in more accurate state estimates over switching targets less frequently or not switching at all. It was then shown how access to LRRR changes for different orbits within the halo and Lyapunov families. In orbits that had fewer measurement opportunities, the state estimation accuracy was reduced. However, simulation results showed that this navigation method is capable of accurately estimating a spacecraft's states even without complete access to the LRRR throughout the orbit. Orbit test cases with more than 55% access to LRRR were shown to provide position estimation with error less than 5 km, and

velocity estimation error less than 5.5 cm/s. For orbits with 70% or better, estimation error drops below 2.25 km in position and 2.5 cm/s in velocity. For test cases where orbits with 100% access to LRRR were simulated, sub 1 km and 2 cm/s errors in absolute position and velocity estimation were achieved.

5.1 Improving Limitations & Future Work

The preliminary development and proof of concept of this navigation method has the potential to build in many different directions on its path to become a viable option for future cislunar spacecraft.

To eventually implement lunar laser ranging on a cislunar spacecraft mission, an investigation feasibility of this concept from a hardware perspective is critical. Analyses will need to be conducted on necessary flight capable instrumentation and hardware. This will include deriving mission requirements from supporting subsystems and sizing spacecraft components. For example, power supply and pointing accuracy have large impacts on the overall performance of this navigation method. A study looking at the amount of protons captured at L_1 orbits from the returned laser pulse will determine the achievable measurement accuracy and provide the minimum dimensions and sensitivities for scaling photon sensors. One could also investigate miniaturization of ground station equipment, or design system requirements for generating a laser beam with necessary properties for spacecraft-based laser ranging. NASA's Laser Communications Relay Demonstration (LCRD [72]) and other missions that employ space-based lasers may serve as a good starting point for exploring a transmitter design and taking advantage of previously developed, heritage components.

Alternatively, it would be interesting to study the hardware on the moon in order to expand the restrictive field of view. 3-dimensional LRRR panel arrangements or a polyhedral dome

design could be used to accommodate a wider variety of incoming laser incident angles to provide a larger service area for spacecraft laser ranging measurements.

Given that the investigation conducted in this thesis is limited to Lyapunov and halo orbits about L_1, it would be interesting to evaluate the applicability spacecraft lunar laser ranging for trans-lunar trajectories and for spacecraft approaching L_1 or the Moon.

Additionally, one could design the optimal placement of a new set of lunar reflectors to replace or expand the current set. The design could target serving a broader range of periodic orbits. Alternatively, the design could aim at providing optimal accuracy for a subset of the cislunar region or family of orbits such as NHROs since they have zero access to the existing LRRR. A similar design study could be conducted to install a set of LRRR on far side of Moon to enable spacecraft-based laser ranging navigation to be used on trajectories in the vicinity of L_2.

As mentioned earlier, it is critical to implement this navigation method with different controllers to emulate a more realistic scenario to analyze navigation performance. Testing a spacecraft's ability to maintain its trajectory from the estimated states will further demonstrate the concept's feasibility on future cislunar missions. This will also alleviate the discrepancies between the actual and expected errors discussed in Chapter 4. Another way of removing the discrepancies between these performance metrics and quantifying the error variability is to implement a Monte Carlo simulation. It is anticipated that the average of the actual errors over a large number of simulation runs will be much more commensurable with the expected error. Furthermore, improvements can be made to the simulation by relaxing some of the assumptions made and including affects from additional bodies and perturbation sources. For example, one could use a higher fidelity dynamical model to propagate the truth states for a more realistic analysis of the navigation and control algorithms.

Overall, the simulation results presented in this thesis shows that spacecraft laser ranging to LRRR is a viable method for autonomously navigating in some halo and Lyapunov orbits about L_1. Because orbit selection directly affects LRRR visibility, the amount of measurement opportunity is predictable, thus the navigation performance is also governed by the chosen orbit. This means that the required navigation accuracy for specific spacecraft missions will limit orbit design options. In general, orbits with 55% access or better to LRRR will provide the best state estimation performance. In all test cases simulated, laser ranging measurements to LRRR on the Moon were the only source of information for the EKF or SRF to provide updated state estimates. This method enables a spacecraft to be self reliant for trajectory determination as it employs a heritage measurement technique with redundant targets and only relies on existing, passive lunar infrastructure. Updates from active Earth-based ground or space tracking services were not required to achieve the level of state estimation accuracy demonstrated in Chapter 4. Spacecraft lunar laser ranging may provide future missions with a method of resilient navigation in cislunar space and enable future spacecraft to operate independently of any Earth-based resources beyond geosynchronous orbit.

Bibliography

[1] The locations of lunar retroreflectors left by apollo and luna missions, 5 2004. Accessed: 05/18/2023.

[2] Apollo 11 lunar laser ranging retroreflector, 7 1969. Accessed: 05/18/2023.

[3] Tom Zagwodzki. Goddard's laser ranging facility. Accessed: 04/19/2023.

[4] Dave Scott. Close-up of apollo 15 retroreflector, 8 1971. Accessed: 05/18/2023.

[5] Solar System Dynamics. Jpl three-body periodic orbit catalog. Accessed: 04/19/2023.

[6] Daniel J. Grebow. Generating periodic orbits in the circular restricted three-body problem with applications to lunar south pole coverage. Master's thesis, Purdue University, West Lafayette, IN, USA, May 2006.

[7] Jacob K. Vendl and Marcus J. Holzinger. Cislunar periodic orbit analysis for persistent space object detection capability. *Journal of Spacecraft and Rockets*, 58(4):1174–1185, 2021.

[8] Marc Sanchez Net, Jay Wyatt, Rebecca Castano, Stephen A. Townes, T. Joseph W. Lazio, Benjamin K. Malphrus, Jeffrey A. Kruth, Chloe Hart, and Emily Mattle. Enabling a larger deep space mission suite: A deep space network queuing antenna for demand access. In *2022 IEEE Aerospace Conference (AERO)*, pages 1–13, 2022.

[9] Dylan J. Thomas, Kevin M. Nastasi, Kevin Schroeder, and Jonathan T. Black. Autonomous multi-phenomenology space domain sensor tasking and adaptive estimation. In *2018 21st International Conference on Information Fusion (FUSION)*, pages 1331–1338, 2018.

[10] M. J. Holzinger, C. C. Chow, and P. Garretson. A primer on cislunar space. Technical report, Air Force Research Laboratory, Wright-Patterson Air Force Base, Dayton, Ohio, March 2021.

[11] Erin E. Fowler, Stella B. Hurtt, and Derek A. Paley. 2nd iaa conference on space situational awareness (icssa) washington, dc, usa iaa-icssa-20-0x-xx orbit design for cislunar space domain awareness. 2019.

[12] John A. Christian and E. Glenn Lightsey. Review of options for autonomous cislunar navigation. *Journal of Spacecraft and Rockets*, 46(5):1023–1036, 2009.

[13] Joseph H. Yuen. *Deep Space Communications*, chapter 1, pages 1–13. John Wiley & Sons, Ltd, 2016.

[14] Rachit Bhatia, David Geller, and David Geller. Autonomous navigation using gravity gradient measurements. 10 2017.

[15] Mark Beckman. Orbit determination issues for libration point orbits. pages 1–17, 05 2003.

[16] Kevin Michael Nastasi. *Autonomous and Responsive Surveillance Network Management for Adaptive Space Situational Awareness*. Phd dissertation, Virginia Polytechnic Institute and State University, Blacksburg, VA, USA, June 2018.

[17] Keric A. Hill. *Autonomous Navigation in Libration Point Orbits*. Phd dissertation, Purdue University, West Lafayette, IN, USA, August 2019.

[18] Howard Hu and Tim Straube. *Orion GN&C Overview and Architecture*. 2007.

[19] Jo Yim, John Crassidis, and John Junkins. *Autonomous orbit navigation of interplanetary spacecraft*. 2000.

[20] Matthew Wilkinson, Ulrich Schreiber, Ivan Procházka, Christopher Moore, John Degnan, Georg Kirchner, Zhang Zhongping, Peter Dunn, Victor Shargorodskiy, Mikhail Sadovnikov, et al. The next generation of satellite laser ranging systems. *Journal of Geodesy*, 93:2227–2247, 2019.

[21] M. J. Holzinger and M. K. Jah. Challenges and potential in space domain awareness. *Journal of Guidance, Control, and Dynamics*, 41(1):15–18, 2018.

[22] Mark L. Psiaki. Autonomous orbit and magnetic field determination using magnetometer and star sensor data. *Journal of Guidance, Control, and Dynamics*, 18(3):584–592, 1995.

[23] Mark L. Psiaki. Autonomous low-earth-orbit determination from magnetometer and sun sensor data. *Journal of Guidance, Control, and Dynamics*, 22(2):296–304, 1999.

[24] Chao Xu, Xiangyu Huang, Maodeng Li, and Dayi Wang. Autonomous navigation using natural landmark measurements for earth orbit satellites. In *2019 Chinese Control Conference (CCC)*, pages 4078–4082, 2019.

[25] D.J. Mudgway, United States. National Aeronautics, and Space Administration. Office of External Relations. *Uplink-downlink: A History of the NASA Deep Space Network, 1957-1997*. NASA SP. National Aeronautics and Space Administration, 2001.

[26] Keric Hill and George H. Born. Autonomous interplanetary orbit determination using satellite-to-satellite tracking. *Journal of Guidance, Control, and Dynamics*, 30(3):679–686, 2007.

[27] Keric Hill, Martin Lo, and George Born. Liaison navigation in the sun-earth-moon four-body problem. 04 2023.

[28] Bradley Cheetham. *Cislunar Autonomous Positioning System Technology Operations and Navigation Experiment (CAPSTONE).* 2020.

[29] Michael Thompson, Alec Forsman, Brian Peters, Todd Ely, Dana Sorensen, and Brad Cheetham. Cislunar navigation technology demonstrations on the capstone mission. 01 2022.

[30] John Christian. Starnav: Autonomous optical navigation of a spacecraft by the relativistic perturbation of starlight. *Sensors*, 19:4064, 09 2019.

[31] Nasa laser reflector for esa satnav on lunar pathfinder. https://www.esa.int/Applications/Navigation/NASA_laser_reflector_for_ESA_satnav_on_Lunar_Pathfinder, October 2022. Accessed: 04/04/2023.

[32] Pietro Giordano, Floor Malman, Richard Swinden, Paolo Zoccarato, and Javier Ventura-Traveset. The lunar pathfinder pnt experiment and moonlight navigation service: The future of lunar position, navigation and timing. In *Proceedings of the 2022 International Technical Meeting of The Institute of Navigation*, pages 632–642, 2022.

[33] Suneel I. Sheikh, Darryll J. Pines, Paul S. Ray, Kent S. Wood, Michael N. Lovellette, and Michael T. Wolff. Spacecraft navigation using x-ray pulsars. *Journal of Guidance, Control, and Dynamics*, 29(1):49–63, 2006.

[34] M. V. Sazhin, V. E. Zharov, V. K. Milyukov, M. S. Pshirkov, V. N. Sementsov, and O. S. Sazhina. Space navigation by x-ray pulsars. *Moscow University Physics Bulletin*, 73(2):141–153, Mar 2018.

[35] Greg N. Holt, Christopher N. D'Souza, and David W. Saley. *Orion Optical Navigation Progress Toward Exploration Mission 1.* 2018.

[36] Kenneth Williams, Anthony Taylor, Brian Page, Peter Wolff, Bobby Williams, Dale Stanbridge, and James McAdams. *Navigation for the MESSENGER Mission's First Mercury Encounter*. June 2012.

[37] CHARLES H. ACTON. Processing onboard optical data for planetary approach navigation. *Journal of Spacecraft and Rockets*, 9(10):746–750, 1972.

[38] Mark Psiaki and Joanna Hinks. *Autonomous Lunar Orbit Determination Using Star Occultation Measurements*. August 2007.

[39] Keric A. Hill. *Star occultation measurements as an aid to navigation in cis-lunar space*. Phd dissertation, Massachusetts Institute of Technology, Cambridge, MA, USA, June 1962.

[40] Aerospace develops a low cost cislunar navigation approach. https://aerospace.org/article/aerospace-develops-low-cost-cislunar-navigation-approach, December 2022. Accessed: 04/04/2023.

[41] Jam: Jervis autonomy module. https://www.rheaspaceactivity.com/. Accessed: 04/04/2023.

[42] Jared Frank and Ahmad Bani Younes. New orbit determination techniques using lunar reflectors. In *33rd AAS/AIAA Space Flight Mechanics Meeting*, 2023. Paper AAS 23-239.

[43] P. L. Bender, D. G. Currie, S. K. Poultney, C. O. Alley, R. H. Dicke, D. T. Wilkinson, D. H. Eckhardt, J. E. Faller, W. M. Kaula, J. D. Mulholland, H. H. Plotkin, E. C. Silverberg, and J. G. Williams. The lunar laser ranging experiment. *Science*, 182(4109):229–238, 1973.

[44] TW Murphy Jr, JD Strasburg, CW Stubbs, EG Adelberger, J Angle, K Nordtvedt, JG Williams, JO Dickey, and B Gillespie. The apache point observatory lunar laser-ranging operation (apollo). In *Proceedings of 12th International Workshop on Laser, Ranging, Matera, Italy*. Citeseer, 2000.

[45] David Folta, Natasha Bosanac, Ian Elliott, Laurie Mann, Rebecca Mesarch, and Jose Rosales. Astrodynamics convention and modeling reference for lunar, cislunar, and libration point orbits. Technical publication, NASA Goddard Space Flight Center, Greenbelt, Maryland 20771, December 2022.

[46] Brent A. Archinal. Lunar coordinates and cartography: Coordinate system establishment, improvement, and control (registration) of lunar datasets, from past, present and future u. s. and foreign missions. Technical report, U.S. Geological Survey, 2255 N. Gemini Drive, Flagstaff, AZ 86004, May 2006.

[47] Howard D. Curtis. *Orbital Mechanics for Engineering Students*, chapter 2.12, pages 123–144. Elsevier, 3rd edition, 2014.

[48] Matthew J. Bolliger. Cislunar mission design: Transfers linking near rectilinear halo orbits and the butterfly family. Master's thesis, Purdue University, West Lafayette, IN, USA, August 2019.

[49] W.S. Koon, M.W. Lo, J.E. Marsden, and S.D. Ross. *Dynamical Systems, the Three-Body Problem and Space Mission Design*, chapter 2.2, pages 24–34. Mardsen Books, 2011.

[50] Kathleen C. Howell. Three-dimensional periodic halo orbits. *Celestial Mechanics and Dynamical Astronomy*, 32:53–71, 1981.

[51] Adam Wilmer, Robert A. Bettinger, and Bryan Little. *Cislunar Periodic Orbit Constellation Assessment for Space Domain Awareness of L1 and L2 Halo Orbits*. 2021.

[52] David A. Vallado. *Fundamentals of Astrodynamics and Applications*, chapter 12.7, pages 967–982. Space Technology Library. Microcosm Press, Hawthorne, CA, 4th edition, 2013.

[53] Kathleen Howell and E.T. Campbell. Three-dimensional periodic solutions that bifurcate from halo families in the circular restricted three-body problem. *Advances in the Astronautical Sciences*, 102:891–910, 01 1999.

[54] Adam P. Wilmer and Robert A. Bettinger. Lagrangian dynamics and the discovery of cislunar periodic orbits. *Nonlinear Dynamics*, 111(1):155–178, Jan 2023.

[55] John V. Breakwell and J. V. Brown. The 'halo' family of 3-dimensional periodic orbits in the earth-moon restricted 3-body problem. *Celestial mechanics*, 20:389–404, 1979.

[56] Jeffrey S Parker and Rodney L Anderson. *Low-energy lunar trajectory design*, volume 12. John Wiley & Sons, 2014.

[57] Gerard Gomez, Wang S Koon, Martin W Lo, Jerrold E Marsden, J Masdemont, and Shane D Ross. *Invariant manifolds, the spatial three-body problem and space mission design*. Number 109. American Astronautical Society, 2001.

[58] Gerard Gómez, Wang S Koon, MW Lo, Jerrold E Marsden, Josep Masdemont, and Shane D Ross. Connecting orbits and invariant manifolds in the spatial restricted three-body problem. *Nonlinearity*, 17(5):1571, 2004.

[59] Wang Sang Koon, MARTIN W Lo, JERROLD E Marsden, and SHANE D Ross. Low energy transfer to the moon. *Celestial Mechanics and Dynamical Astronomy*, 81(1-2):63–73, 2001.

[60] J. Dickey, P Bender, J. Faller, X Newhall, Randall Ricklefs, J Ries, P Shelus, Christian Veillet, AL Whipple, J Wiant, James Williams, and C Yoder. Lunar laser ranging: A continuing legacy of the apollo program. *Science (New York, N.Y.)*, 265:482–90, 08 1994.

[61] A standardized lunar coordinate system for the lunar reconnaissance orbiter and lunar datasets. Technical report, Goddard Space Flight Center, Greenbelt, Maryland, October 2008.

[62] Andrea Colagrossi, Stefano Silvestrini, and Vincenzo Pesce. Chapter two - reference systems and planetary models. In Vincenzo Pesce, Andrea Colagrossi, and Stefano Silvestrini, editors, *Modern Spacecraft Guidance, Navigation, and Control*, pages 45–75. Elsevier, 2023.

[63] J.G. Williams, D.H. Boggs, and W.M. Folkner. De421 lunar orbit, physical librations, and surface coordinates. Interoffice memorandum, Jet Propulsion Laboratory, California Institute of Technology, March 2008.

[64] Ryan S. Park, William M. Folkner, James G. Williams, and Dale H. Boggs. The jpl planetary and lunar ephemerides de440 and de441. *The Astronomical Journal*, 161(3):105, feb 2021.

[65] Chengli Huang, W. Jin, and H. Xu. The terrestrial and lunar reference frame in lunar laser ranging. *Journal of Geodesy*, 73:125–129, 04 1999.

[66] R. V. Wagner, E. J. Speyerer, K. N. Burns, J. Danton, and Mark Robinson. Revised coordinates for apollo hardware. In *International Archives of the Photogrammetry, Remote Sensing and Spatial Information Sciences - ISPRS Archives*, volume 39, pages 517–521. International Society for Photogrammetry and Remote Sensing, 2012. 22nd

Congress of the International Society for Photogrammetry and Remote Sensing, ISPRS 2012 ; Conference date: 25-08-2012 Through 01-09-2012.

[67] Frank L. Pedrotti and Leno S. Pedrotti. *Introduction to Optics*, chapter 22-4, pages 461–476. Prentice Hall, Englewood Cliffs, NJ, 2nd edition, 1993.

[68] C. D'Souza, G. Holt, R. Gay, and Renato Zanetti. Navigation design and analysis for the orion cislunar exploration missions. volume 151, pages 543–556, 01 2014.

[69] James G. Williams, Dale H. Boggs, and William M. Folkner. De430 lunar orbit, physical librations, and surface coordinates. Interoffice memorandum, Jet Propulsion Laboratory, California Institute of Technology, July 2013.

[70] Kevin Tracy. A square-root kalman filter using only qr decompositions, 08 2022.

[71] Iain Murray. Differentiation of the cholesky decomposition, 02 2016.

[72] Bernard Edwards. *Overview of the Laser Communications Relay Demonstration Project.* 2012.

Appendices

Appendix A

Derivation of Measurement Model

Starting with the measurement model given in Section 3.4, Equations 3.6 and 3.7 are repeated here.

$$\begin{aligned} c\Delta t &= \rho(t) + \rho(t + \Delta t) \\ &= \rho(t_{\text{sent}}) + \rho(t_{\text{received}}) \\ &= \rho_{\text{sent}} + \rho_{\text{received}} \end{aligned} \tag{A.1}$$

$$\begin{aligned} \rho_{\text{sent}} &= ||\boldsymbol{r}_{\text{sent}} - \boldsymbol{r}_{\text{LRRR}}||_2 \\ \rho_{\text{received}} &= ||\boldsymbol{r}_{\text{received}} - \boldsymbol{r}_{\text{LRRR}}||_2 \end{aligned} \tag{A.2}$$

Again, c is the speed of light, and ρ is the distance from a satellite's position at time, t, to a LRRR. $\boldsymbol{r}$ is a position vector, $\boldsymbol{v}$ is a velocity vector. and $\boldsymbol{X}$ is the spacecraft state vector given in Equation 2.2. Because the spacecraft is moving along its trajectory when the laser pulse is transmitted, it will be in a different position when the reflected pulse is received by the satellite. Δt is the time delay between instances when the laser pulses are sent and received. Subscripts, "sent" and "recieved" are introduced to distinguish between these two points in time. Additionally, the spacecraft can make laser ranging measurements to any of the five available LRRR. The subscript, "LRRR" is used to generalize quantities describing LRRR such that the corresponding values for any of them can be used. ρ can be written

more explicitly as:

$$\boldsymbol{\rho} = \begin{bmatrix} (x - x_{\text{LRRR}}) \\ (y - y_{\text{LRRR}}) \\ (z - z_{\text{LRRR}}) \end{bmatrix} \tag{A.3}$$

$$\rho = ||\boldsymbol{\rho}||_2 = ||\boldsymbol{r} - \boldsymbol{r}_{\text{LRRR}}||_2 = \left[(x - x_{\text{LRRR}})^2 + (y - y_{\text{LRRR}})^2 + (z - z_{\text{LRRR}})^2\right]^{1/2} \tag{A.4}$$

To find the Jacobian of the measurement model, measurement equation (Eqn. A.1) can be rearranged and differentiated with respect to the position states, $\boldsymbol{r}_{\text{sent}}$, of independent variable, $\boldsymbol{X}_{\text{sent}}$. Δt and $\boldsymbol{X}_{\text{received}}$ are both a function of $\boldsymbol{X}_{\text{sent}}$.

$$\begin{aligned} 0 &= \rho_{\text{sent}} + \rho_{\text{recieved}} - c\Delta t \\ 0 &= \frac{\partial \rho_{\text{sent}}}{\partial \boldsymbol{r}_{\text{sent}}} + \frac{\partial \rho_{\text{recieved}}}{\partial \boldsymbol{r}_{\text{sent}}} + \frac{\partial \rho_{\text{recieved}}}{\partial \Delta t}\frac{\partial \Delta t}{\partial \boldsymbol{r}_{\text{sent}}} - c\frac{\partial \Delta t}{\partial \boldsymbol{r}_{\text{sent}}} \\ 0 &= \frac{\partial \rho_{\text{sent}}}{\partial \boldsymbol{r}_{\text{sent}}} + \frac{\partial \rho_{\text{recieved}}}{\partial \boldsymbol{r}_{\text{sent}}} + \left[\frac{\partial \rho_{\text{recieved}}}{\partial \Delta t} - c\right]\frac{\partial \Delta t}{\partial \boldsymbol{r}_{\text{sent}}} \end{aligned} \tag{A.5}$$

Since Δt is the actual parameter which is being measured, we can rearrange Equation A.5 and and solve for the derivative of the measurement with respect to the position states at t_{sent}. This gives a 1×3 array:

$$\frac{\partial \Delta t}{\partial \boldsymbol{r}_{\text{sent}}} = \frac{\frac{\partial \rho_{\text{sent}}}{\partial \boldsymbol{r}_{\text{sent}}} + \frac{\partial \rho_{\text{recieved}}}{\partial \boldsymbol{r}_{\text{sent}}}}{c - \frac{\partial \rho_{\text{recieved}}}{\partial \Delta t}} \tag{A.6}$$

Following a similar process for velocity also gives a 1×3 array:

$$\frac{\partial \Delta t}{\partial \boldsymbol{v}_{\text{sent}}} = \frac{\frac{\partial \rho_{\text{sent}}}{\partial \boldsymbol{v}_{\text{sent}}} + \frac{\partial \rho_{\text{recieved}}}{\partial \boldsymbol{v}_{\text{sent}}}}{c - \frac{\partial \rho_{\text{recieved}}}{\partial \Delta t}} \tag{A.7}$$

Equations A.6 and A.7 can be broken down into the derivatives of Δt with respect to each individual state. Starting with the x position component:

$$\frac{\partial \Delta t}{\partial x_{\text{sent}}} = \frac{\frac{\partial \rho_{\text{sent}}}{\partial x_{\text{sent}}} + \frac{\partial \rho_{\text{recieved}}}{\partial x_{\text{sent}}}}{c - \frac{\partial \rho_{\text{recieved}}}{\partial \Delta t}} \tag{A.8}$$

Evaluating each derivative term individually, starting with:

$$\frac{\partial \rho_{\text{sent}}}{\partial x_{\text{sent}}} = \frac{\partial}{\partial x_{\text{sent}}} \Big[(x_{\text{sent}} - x_{\text{LRRR}})^2 + (y_{\text{sent}} - y_{\text{LRRR}})^2 + (z_{\text{sent}} - z_{\text{LRRR}})^2 \Big]^{1/2}$$

$$\begin{aligned} \frac{\partial \rho_{\text{sent}}}{\partial x_{\text{sent}}} = \frac{1}{2} \Big[(x_{\text{sent}} - x_{\text{LRRR}})^2 + (y_{\text{sent}} - y_{\text{LRRR}})^2 + (z_{\text{sent}} - z_{\text{LRRR}})^2 \Big]^{-1/2} \times \\ \Big[\frac{\partial}{\partial x_{\text{sent}}} (x_{\text{sent}} - x_{\text{LRRR}})^2 + \frac{\partial}{\partial x_{\text{sent}}} (y_{\text{sent}} - y_{\text{LRRR}})^2 + \frac{\partial}{\partial x_{\text{sent}}} (z_{\text{sent}} - z_{\text{LRRR}})^2 \Big] \end{aligned}$$

$$\begin{aligned} \frac{\partial \rho_{\text{sent}}}{\partial x_{\text{sent}}} = \frac{1}{2} \Big[(x_{\text{sent}} - x_{\text{LRRR}})^2 + (y_{\text{sent}} - y_{\text{LRRR}})^2 + (z_{\text{sent}} - z_{\text{LRRR}})^2 \Big]^{-1/2} \times \\ \Big[2(x_{\text{sent}} - x_{\text{LRRR}}) + 2(y_{\text{sent}} - y_{\text{LRRR}}) \cancel{\frac{\partial y_{\text{sent}}}{\partial x_{\text{sent}}}} + 2(z_{\text{sent}} - z_{\text{LRRR}}) \cancel{\frac{\partial z_{\text{sent}}}{\partial x_{\text{sent}}}} \Big] \end{aligned}$$

$$\begin{aligned} \frac{\partial \rho_{\text{sent}}}{\partial x_{\text{sent}}} &= \Big[(x_{\text{sent}} - x_{\text{LRRR}})^2 + (y_{\text{sent}} - y_{\text{LRRR}})^2 + (z_{\text{sent}} - z_{\text{LRRR}})^2 \Big]^{-1/2} (x_{\text{sent}} - x_{\text{LRRR}}) \\ &= \rho_{\text{sent}}^{-1} (x_{\text{sent}} - x_{\text{LRRR}}) \\ &= \rho_{\text{sent}}^{-1} \boldsymbol{\rho}_{\text{sent}}(1) \end{aligned} \tag{A.9}$$

Where $\boldsymbol{\rho}_{\text{sent}}(1)$ represents the x component of $\boldsymbol{\rho}_{\text{sent}}$.

The second term:

$$\frac{\partial \rho_{\text{recieved}}}{\partial x_{\text{sent}}} = \frac{\partial}{\partial x_{\text{sent}}}\Big[(x_{\text{recieved}} - x_{\text{LRRR}})^2 + (y_{\text{recieved}} - y_{\text{LRRR}})^2 + (z_{\text{recieved}} - z_{\text{LRRR}})^2\Big]^{1/2}$$

$$\frac{\partial \rho_{\text{recieved}}}{\partial x_{\text{sent}}} = \frac{1}{2}\Big[(x_{\text{recieved}} - x_{\text{LRRR}})^2 + (y_{\text{recieved}} - y_{\text{LRRR}})^2 + (z_{\text{recieved}} - z_{\text{LRRR}})^2\Big]^{-1/2} \times \Big[\frac{\partial}{\partial x_{\text{sent}}}(x_{\text{recieved}} - x_{\text{LRRR}})^2 + \frac{\partial}{\partial x_{\text{sent}}}(y_{\text{recieved}} - y_{\text{LRRR}})^2 + \frac{\partial}{\partial x_{\text{sent}}}(z_{\text{recieved}} - z_{\text{LRRR}})^2\Big]$$

$$\frac{\partial \rho_{\text{recieved}}}{\partial x_{\text{sent}}} = \frac{1}{2}\Big[(x_{\text{recieved}} - x_{\text{LRRR}})^2 + (y_{\text{recieved}} - y_{\text{LRRR}})^2 + (z_{\text{recieved}} - z_{\text{LRRR}})^2\Big]^{-1/2} \times \Big[2(x_{\text{recieved}} - x_{\text{LRRR}})\frac{\partial x_{\text{recieved}}}{\partial x_{\text{sent}}} + 2(y_{\text{recieved}} - y_{\text{LRRR}})\frac{\partial y_{\text{recieved}}}{\partial x_{\text{sent}}} + 2(z_{\text{recieved}} - z_{\text{LRRR}})\frac{\partial z_{\text{recieved}}}{\partial x_{\text{sent}}}\Big]$$

$$\frac{\partial \rho_{\text{recieved}}}{\partial x_{\text{sent}}} = \Big[(x_{\text{recieved}} - x_{\text{LRRR}})^2 + (y_{\text{recieved}} - y_{\text{LRRR}})^2 + (z_{\text{recieved}} - z_{\text{LRRR}})^2\Big]^{-1/2} \times \Big[(x_{\text{recieved}} - x_{\text{LRRR}})\frac{\partial x_{\text{recieved}}}{\partial x_{\text{sent}}} + (y_{\text{recieved}} - y_{\text{LRRR}})\frac{\partial y_{\text{recieved}}}{\partial x_{\text{sent}}} + (z_{\text{recieved}} - z_{\text{LRRR}})\frac{\partial z_{\text{recieved}}}{\partial x_{\text{sent}}}\Big]$$

$$\frac{\partial \rho_{\text{recieved}}}{\partial x_{\text{sent}}} = \Big[(x_{\text{recieved}} - x_{\text{LRRR}})^2 + (y_{\text{recieved}} - y_{\text{LRRR}})^2 + (z_{\text{recieved}} - z_{\text{LRRR}})^2\Big]^{-1/2} \times \Big[(x_{\text{recieved}} - x_{\text{LRRR}})\Phi(1,1) + (y_{\text{recieved}} - y_{\text{LRRR}})\Phi(2,1) + (z_{\text{recieved}} - z_{\text{LRRR}})\Phi(3,1)\Big]$$

$$\frac{\partial \rho_{\text{recieved}}}{\partial x_{\text{sent}}} = \rho_{\text{recieved}}^{-1}\boldsymbol{\rho}_{\text{received}}^{T}\Phi(1:3,1) \tag{A.10}$$

Where $\Phi(1:3,1)$ represents the first three element in the first column of the state transition matrix Φ.

The third term:

$$\frac{\partial \rho_{\text{recieved}}}{\partial \Delta t} = \frac{\partial \rho_{\text{recieved}}}{\partial x_{\text{recieved}}} \frac{\partial x_{\text{recieved}}}{\partial \Delta t}$$

$$\frac{\partial \rho_{\text{recieved}}}{\partial \Delta t} = \frac{\partial}{\partial x_{\text{recieved}}} \Big[(x_{\text{recieved}} - x_{\text{LRRR}})^2 + (y_{\text{recieved}} - y_{\text{LRRR}})^2 + (z_{\text{recieved}} - z_{\text{LRRR}})^2 \Big]^{1/2} \frac{\partial x_{\text{recieved}}}{\partial \Delta t}$$

$$\frac{\partial \rho_{\text{recieved}}}{\partial \Delta t} = \frac{1}{2} \Big[(x_{\text{recieved}} - x_{\text{LRRR}})^2 + (y_{\text{recieved}} - y_{\text{LRRR}})^2 + (z_{\text{recieved}} - z_{\text{LRRR}})^2 \Big]^{-1/2} \times$$
$$\Big[\frac{\partial}{\partial x_{\text{recieved}}} (x_{\text{recieved}} - x_{\text{LRRR}})^2 + \frac{\partial}{\partial x_{\text{recieved}}} (y_{\text{recieved}} - y_{\text{LRRR}})^2 + \frac{\partial}{\partial x_{\text{recieved}}} (z_{\text{recieved}} - z_{\text{LRRR}})^2 \Big] \frac{\partial x_{\text{recieved}}}{\partial \Delta t}$$

$$\frac{\partial \rho_{\text{recieved}}}{\partial \Delta t} = \frac{1}{2} \Big[(x_{\text{recieved}} - x_{\text{LRRR}})^2 + (y_{\text{recieved}} - y_{\text{LRRR}})^2 + (z_{\text{recieved}} - z_{\text{LRRR}})^2 \Big]^{-1/2} \times$$
$$\Big[2(x_{\text{recieved}} - x_{\text{LRRR}}) + 2(y_{\text{recieved}} - y_{\text{LRRR}}) \frac{\partial y_{\text{recieved}}}{\partial x_{\text{recieved}}} + 2(z_{\text{recieved}} - z_{\text{LRRR}}) \frac{\partial z_{\text{recieved}}}{\partial x_{\text{recieved}}} \Big] \frac{\partial x_{\text{recieved}}}{\partial \Delta t}$$

$$\frac{\partial \rho_{\text{recieved}}}{\partial \Delta t} = \Big[(x_{\text{recieved}} - x_{\text{LRRR}})^2 + (y_{\text{recieved}} - y_{\text{LRRR}})^2 + (z_{\text{recieved}} - z_{\text{LRRR}})^2 \Big]^{-1/2} \times$$
$$\Big[(x_{\text{recieved}} - x_{\text{LRRR}}) + (y_{\text{recieved}} - y_{\text{LRRR}}) \frac{\partial y_{\text{recieved}}}{\cancel{\partial x_{\text{recieved}}}} + (z_{\text{recieved}} - z_{\text{LRRR}}) \frac{\partial z_{\text{recieved}}}{\cancel{\partial x_{\text{recieved}}}} \Big] \frac{\partial x_{\text{recieved}}}{\partial \Delta t}$$

$$\frac{\partial \rho_{\text{recieved}}}{\partial \Delta t} = \Big[(x_{\text{recieved}} - x_{\text{LRRR}})^2 + (y_{\text{recieved}} - y_{\text{LRRR}})^2 + (z_{\text{recieved}} - z_{\text{LRRR}})^2\Big]^{-1/2} \times (x_{\text{recieved}} - x_{\text{LRRR}}) v_{x,\text{recieved}}$$

$$\frac{\partial \rho_{\text{recieved}}}{\partial \Delta t} = \rho_{\text{recieved}}^{-1} \boldsymbol{\rho}_{\text{recieved}}(1) v_{x,\text{recieved}} \tag{A.11}$$

Combining all three terms, yielding a scalar value:

$$\begin{aligned} \frac{\partial \Delta t}{\partial x_{\text{sent}}} &= \frac{\boldsymbol{\rho}_{\text{sent}}(1)\rho_{\text{sent}}^{-1} + \rho_{\text{recieved}}^{-1}\boldsymbol{\rho}_{\text{recieved}}^{T}\Phi(1:3,1)}{c - \rho_{\text{recieved}}^{-1}\boldsymbol{\rho}_{\text{recieved}}(1)v_{x,\text{recieved}}} \\ &= \frac{\rho_{\text{sent}}^{-1}\big(\boldsymbol{\rho}_{\text{sent}}(1) + \rho_{\text{sent}}\rho_{\text{recieved}}^{-1}\boldsymbol{\rho}_{\text{recieved}}^{T}\Phi(1:3,1)\big)}{\rho_{\text{recieved}}^{-1}\big(\rho_{\text{recieved}}c - \boldsymbol{\rho}_{\text{recieved}}(1)v_{x,\text{recieved}}\big)} \\ &= \frac{\rho_{\text{recieved}}\boldsymbol{\rho}_{\text{sent}}(1) + \rho_{\text{sent}}\boldsymbol{\rho}_{\text{recieved}}^{T}\Phi(1:3,1)}{\rho_{\text{sent}}\rho_{\text{recieved}}c - \rho_{\text{sent}}\boldsymbol{\rho}_{\text{recieved}}(1)v_{x,\text{recieved}}} \end{aligned} \tag{A.12}$$

Repeating the same process for the y component:

$$\frac{\partial \Delta t}{\partial y_{\text{sent}}} = \frac{\frac{\partial \rho_{\text{sent}}}{\partial y_{\text{sent}}} + \frac{\partial \rho_{\text{recieved}}}{\partial y_{\text{sent}}}}{c - \frac{\partial \rho_{\text{recieved}}}{\partial \Delta t}} \tag{A.13}$$

All three derivative terms are evaluated individually:

$$\frac{\partial \rho_{\text{sent}}}{\partial y_{\text{sent}}} = \frac{\partial}{\partial y_{\text{sent}}}\Big[(x_{\text{sent}} - x_{\text{LRRR}})^2 + (y_{\text{sent}} - y_{\text{LRRR}})^2 + (z_{\text{sent}} - z_{\text{LRRR}})^2\Big]^{1/2}$$

$$\frac{\partial \rho_{\text{sent}}}{\partial y_{\text{sent}}} = \frac{1}{2}\Big[(x_{\text{sent}} - x_{\text{LRRR}})^2 + (y_{\text{sent}} - y_{\text{LRRR}})^2 + (z_{\text{sent}} - z_{\text{LRRR}})^2\Big]^{-1/2} \times \Big[\frac{\partial}{\partial y_{\text{sent}}}(x_{\text{sent}} - x_{\text{LRRR}})^2 + \frac{\partial}{\partial y_{\text{sent}}}(y_{\text{sent}} - y_{\text{LRRR}})^2 + \frac{\partial}{\partial y_{\text{sent}}}(z_{\text{sent}} - z_{\text{LRRR}})^2\Big]$$

$$\frac{\partial \rho_{\text{sent}}}{\partial y_{\text{sent}}} = \frac{1}{2}\Big[(x_{\text{sent}} - x_{\text{LRRR}})^2 + (y_{\text{sent}} - y_{\text{LRRR}})^2 + (z_{\text{sent}} - z_{\text{LRRR}})^2\Big]^{-1/2} \times \Big[2(x_{\text{sent}} - x_{\text{LRRR}})\frac{\partial \cancel{x_{\text{sent}}}}{\partial \cancel{y_{\text{sent}}}} + 2(y_{\text{sent}} - y_{\text{LRRR}}) + 2(z_{\text{sent}} - z_{\text{LRRR}})\frac{\partial \cancel{z_{\text{sent}}}}{\partial \cancel{x_{\text{sent}}}}\Big]$$

$$\begin{aligned}\frac{\partial \rho_{\text{sent}}}{\partial y_{\text{sent}}} &= \Big[(x_{\text{sent}} - x_{\text{LRRR}})^2 + (y_{\text{sent}} - y_{\text{LRRR}})^2 + (z_{\text{sent}} - z_{\text{LRRR}})^2\Big]^{-1/2}(y_{\text{sent}} - y_{\text{LRRR}}) \\ &= \rho_{\text{sent}}^{-1}(y_{\text{sent}} - y_{\text{LRRR}}) \\ &= \rho_{\text{sent}}^{-1}\boldsymbol{\rho}_{\text{sent}}(2)\end{aligned}$$

The second term:

$$\frac{\partial \rho_{\text{recieved}}}{\partial y_{\text{sent}}} = \frac{\partial}{\partial y_{\text{sent}}}\Big[(x_{\text{recieved}} - x_{\text{LRRR}})^2 + (y_{\text{recieved}} - y_{\text{LRRR}})^2 + (z_{\text{recieved}} - z_{\text{LRRR}})^2\Big]^{1/2}$$

$$\frac{\partial \rho_{\text{recieved}}}{\partial y_{\text{sent}}} = \frac{1}{2}\Big[(x_{\text{recieved}} - x_{\text{LRRR}})^2 + (y_{\text{recieved}} - y_{\text{LRRR}})^2 + (z_{\text{recieved}} - z_{\text{LRRR}})^2\Big]^{-1/2} \times \Big[\frac{\partial}{\partial y_{\text{sent}}}(x_{\text{recieved}} - x_{\text{LRRR}})^2 + \frac{\partial}{\partial y_{\text{sent}}}(y_{\text{recieved}} - y_{\text{LRRR}})^2 + \frac{\partial}{\partial y_{\text{sent}}}(z_{\text{recieved}} - z_{\text{LRRR}})^2\Big]$$

$$\frac{\partial \rho_{\text{recieved}}}{\partial y_{\text{sent}}} = \frac{1}{2}\Big[(x_{\text{recieved}} - x_{\text{LRRR}})^2 + (y_{\text{recieved}} - y_{\text{LRRR}})^2 + (z_{\text{recieved}} - z_{\text{LRRR}})^2\Big]^{-1/2} \times \Big[2(x_{\text{recieved}} - x_{\text{LRRR}})\frac{\partial x_{\text{recieved}}}{\partial y_{\text{sent}}} + 2(y_{\text{recieved}} - y_{\text{LRRR}})\frac{\partial y_{\text{recieved}}}{\partial y_{\text{sent}}} + 2(z_{\text{recieved}} - z_{\text{LRRR}})\frac{\partial z_{\text{recieved}}}{\partial y_{\text{sent}}}\Big]$$

$$\frac{\partial \rho_{\text{recieved}}}{\partial y_{\text{sent}}} = \Big[(x_{\text{recieved}} - x_{\text{LRRR}})^2 + (y_{\text{recieved}} - y_{\text{LRRR}})^2 + (z_{\text{recieved}} - z_{\text{LRRR}})^2\Big]^{-1/2} \times$$
$$\Big[(x_{\text{recieved}} - x_{\text{LRRR}})\frac{\partial x_{\text{recieved}}}{\partial y_{\text{sent}}} + (y_{\text{recieved}} - y_{\text{LRRR}})\frac{\partial y_{\text{recieved}}}{\partial y_{\text{sent}}} + (z_{\text{recieved}} - z_{\text{LRRR}})\frac{\partial z_{\text{recieved}}}{\partial y_{\text{sent}}}\Big]$$

$$\frac{\partial \rho_{\text{recieved}}}{\partial y_{\text{sent}}} = \Big[(x_{\text{recieved}} - x_{\text{LRRR}})^2 + (y_{\text{recieved}} - y_{\text{LRRR}})^2 + (z_{\text{recieved}} - z_{\text{LRRR}})^2\Big]^{-1/2} \times$$
$$\Big[(x_{\text{recieved}} - x_{\text{LRRR}})\Phi(1,2) + (y_{\text{recieved}} - y_{\text{LRRR}})\Phi(2,2) + (z_{\text{recieved}} - z_{\text{LRRR}})\Phi(3,2)\Big]$$

$$\frac{\partial \rho_{\text{recieved}}}{\partial y_{\text{sent}}} = \rho_{\text{recieved}}^{-1}\boldsymbol{\rho}_{\text{received}}^{T}\Phi(1:3,2) \tag{A.14}$$

The third term:

$$\frac{\partial \rho_{\text{recieved}}}{\partial \Delta t} = \frac{\partial \rho_{\text{recieved}}}{\partial y_{\text{recieved}}}\frac{\partial y_{\text{recieved}}}{\partial \Delta t}$$

$$\frac{\partial \rho_{\text{recieved}}}{\partial \Delta t} = \frac{\partial}{\partial y_{\text{recieved}}}\Big[(x_{\text{recieved}} - x_{\text{LRRR}})^2 + (y_{\text{recieved}} - y_{\text{LRRR}})^2 + (z_{\text{recieved}} - z_{\text{LRRR}})^2\Big]^{1/2} \times \frac{\partial y_{\text{recieved}}}{\partial \Delta t}$$

$$\frac{\partial \rho_{\text{recieved}}}{\partial \Delta t} = \frac{1}{2}\Big[(x_{\text{recieved}} - x_{\text{LRRR}})^2 + (y_{\text{recieved}} - y_{\text{LRRR}})^2 + (z_{\text{recieved}} - z_{\text{LRRR}})^2\Big]^{-1/2} \times$$
$$\Big[\frac{\partial}{\partial y_{\text{recieved}}}(x_{\text{recieved}} - x_{\text{LRRR}})^2 + \frac{\partial}{\partial y_{\text{recieved}}}(y_{\text{recieved}} - y_{\text{LRRR}})^2 + \frac{\partial}{\partial y_{\text{recieved}}}(z_{\text{recieved}} - z_{\text{LRRR}})^2\Big]\frac{\partial y_{\text{recieved}}}{\partial \Delta t}$$

$$\frac{\partial \rho_{\text{recieved}}}{\partial \Delta t} = \frac{1}{2}\Big[(x_{\text{recieved}} - x_{\text{LRRR}})^2 + (y_{\text{recieved}} - y_{\text{LRRR}})^2 + (z_{\text{recieved}} - z_{\text{LRRR}})^2\Big]^{-1/2} \times$$
$$\Big[2(x_{\text{recieved}} - x_{\text{LRRR}})\frac{\partial x_{\text{recieved}}}{\partial y_{\text{recieved}}} + 2(y_{\text{recieved}} - y_{\text{LRRR}}) + 2(z_{\text{recieved}} - z_{\text{LRRR}})\frac{\partial z_{\text{recieved}}}{\partial y_{\text{recieved}}}\Big]\frac{\partial y_{\text{recieved}}}{\partial \Delta t}$$

$$\frac{\partial \rho_{\text{recieved}}}{\partial \Delta t} = \Big[(x_{\text{recieved}} - x_{\text{LRRR}})^2 + (y_{\text{recieved}} - y_{\text{LRRR}})^2 + (z_{\text{recieved}} - z_{\text{LRRR}})^2\Big]^{-1/2} \times$$
$$\Big[(x_{\text{recieved}} - x_{\text{LRRR}})\frac{\cancel{\partial x_{\text{recieved}}}}{\cancel{\partial y_{\text{recieved}}}} + (y_{\text{recieved}} - y_{\text{LRRR}}) + (z_{\text{recieved}} - z_{\text{LRRR}})\frac{\cancel{\partial z_{\text{recieved}}}}{\cancel{\partial y_{\text{recieved}}}}\Big]\frac{\partial y_{\text{recieved}}}{\partial \Delta t}$$

$$\frac{\partial \rho_{\text{recieved}}}{\partial \Delta t} = \Big[(x_{\text{recieved}} - x_{\text{LRRR}})^2 + (y_{\text{recieved}} - y_{\text{LRRR}})^2 + (z_{\text{recieved}} - z_{\text{LRRR}})^2\Big]^{-1/2} \times$$
$$(y_{\text{recieved}} - y_{\text{LRRR}})v_{y,\text{recieved}}$$

$$\frac{\partial \rho_{\text{recieved}}}{\partial \Delta t} = \rho_{\text{recieved}}^{-1}\boldsymbol{\rho}_{\text{recieved}}(2)v_{y,\text{recieved}} \tag{A.15}$$

Combining all three terms, yielding a scalar value:

$$\begin{aligned}\frac{\partial \Delta t}{\partial y_{\text{sent}}} &= \frac{\boldsymbol{\rho}_{\text{sent}}(2)\rho_{\text{sent}}^{-1} + \rho_{\text{recieved}}^{-1}\boldsymbol{\rho}_{\text{received}}^{T}\Phi(1:3,2)}{c - \rho_{\text{recieved}}^{-1}\boldsymbol{\rho}_{\text{recieved}}(2)v_{y,\text{received}}} \\ &= \frac{\rho_{\text{sent}}^{-1}\big(\boldsymbol{\rho}_{\text{sent}}(2) + \rho_{\text{sent}}\rho_{\text{recieved}}^{-1}\boldsymbol{\rho}_{\text{received}}^{T}\Phi(1:3,2)\big)}{\rho_{\text{recieved}}^{-1}\big(\rho_{\text{recieved}}c - \boldsymbol{\rho}_{\text{recieved}}(2)v_{y,\text{received}}\big)} \\ &= \frac{\rho_{\text{recieved}}\boldsymbol{\rho}_{\text{sent}}(2) + \rho_{\text{sent}}\boldsymbol{\rho}_{\text{received}}^{T}\Phi(1:3,2)}{\rho_{\text{sent}}\rho_{\text{recieved}}c - \rho_{\text{sent}}\boldsymbol{\rho}_{\text{recieved}}(2)v_{y,\text{received}}}\end{aligned} \tag{A.16}$$

Following the pattern from Equations A.12 and A.16 for z gives a scalar:

$$\begin{aligned}\frac{\partial \Delta t}{\partial z_{\text{sent}}} &= \frac{\boldsymbol{\rho}_{\text{sent}}(3)\rho_{\text{sent}}^{-1} + \rho_{\text{recieved}}^{-1}\boldsymbol{\rho}_{\text{received}}^{T}\Phi(1:3,3)}{c - \rho_{\text{recieved}}^{-1}\boldsymbol{\rho}_{\text{recieved}}(3)v_{z,\text{received}}} \\ &= \frac{\rho_{\text{sent}}^{-1}\left(\boldsymbol{\rho}_{\text{sent}}(3) + \rho_{\text{sent}}\rho_{\text{recieved}}^{-1}\boldsymbol{\rho}_{\text{received}}^{T}\Phi(1:3,3)\right)}{\rho_{\text{recieved}}^{-1}\left(\rho_{\text{recieved}}c - \boldsymbol{\rho}_{\text{recieved}}(3)v_{z,\text{received}}\right)} \\ &= \frac{\rho_{\text{recieved}}\boldsymbol{\rho}_{\text{sent}}(3) + \rho_{\text{sent}}\boldsymbol{\rho}_{\text{received}}^{T}\Phi(1:3,3)}{\rho_{\text{sent}}\rho_{\text{recieved}}c - \rho_{\text{sent}}\boldsymbol{\rho}_{\text{recieved}}(3)v_{z,\text{received}}}\end{aligned} \tag{A.17}$$

Consolidating Equations A.12, A.16, and A.17 into vector form:

$$\begin{aligned}\frac{\partial \Delta t}{\partial \boldsymbol{r}} &= \frac{\rho_{\text{recieved}}\boldsymbol{\rho}_{\text{sent}}^{T} + \rho_{\text{sent}}\boldsymbol{\rho}_{\text{received}}^{T}\Phi(1:3,1:3)}{\rho_{\text{sent}}\rho_{\text{recieved}}c - \rho_{\text{sent}}\boldsymbol{\rho}_{\text{received}}^{T}\boldsymbol{v}_{\text{recieved}}} \\ &= \frac{\rho_{\text{recieved}}\boldsymbol{\rho}_{\text{sent}}^{T} + \rho_{\text{sent}}\boldsymbol{\rho}_{\text{received}}^{T}\Phi_{\boldsymbol{rr}}}{\rho_{\text{sent}}\rho_{\text{recieved}}c - \rho_{\text{sent}}\boldsymbol{\rho}_{\text{received}}^{T}\boldsymbol{v}_{\text{recieved}}} \\ &= \frac{\rho_{\text{recieved}}\boldsymbol{\rho}_{\text{sent}}^{T} + \rho_{\text{sent}}\boldsymbol{\rho}_{\text{received}}^{T}\Phi_{\boldsymbol{rr}}}{\rho_{\text{sent}}\left(\rho_{\text{recieved}}c - \boldsymbol{\rho}_{\text{received}}^{T}\boldsymbol{v}_{\text{recieved}}\right)}\end{aligned} \tag{A.18}$$

Where the numerator is a 1×3 vector and the denominator is a scalar.

Now for the velocity components of the state vector, starting from Equation A.7, we can break down the derivative of Δt with respect to the velocity vector into the derivatives of individual states:

$$\frac{\partial \Delta t}{\partial v_{x,\text{sent}}} = \frac{\frac{\partial \rho_{\text{sent}}}{\partial v_{x,\text{sent}}} + \frac{\partial \rho_{\text{recieved}}}{\partial v_{x,\text{sent}}}}{c - \frac{\partial \rho_{\text{recieved}}}{\partial \Delta t}} \tag{A.19}$$

$$\frac{\partial \rho_{\text{sent}}}{\partial v_{x,\text{sent}}} = \frac{\partial}{\partial v_{x,\text{sent}}}\left[(x_{\text{sent}} - x_{\text{LRRR}})^2 + (y_{\text{sent}} - y_{\text{LRRR}})^2 + (z_{\text{sent}} - z_{\text{LRRR}})^2\right]^{1/2}$$

$$\begin{aligned}\frac{\partial \rho_{\text{sent}}}{\partial v_{x,\text{sent}}} = \frac{1}{2}&\left[(x_{\text{sent}} - x_{\text{LRRR}})^2 + (y_{\text{sent}} - y_{\text{LRRR}})^2 + (z_{\text{sent}} - z_{\text{LRRR}})^2\right]^{-1/2} \times \\ &\left[\frac{\partial}{\partial v_{x,\text{sent}}}(x_{\text{sent}} - x_{\text{LRRR}})^2 + \frac{\partial}{\partial v_{x,\text{sent}}}(y_{\text{sent}} - y_{\text{LRRR}})^2 + \frac{\partial}{\partial v_{x,\text{sent}}}(z_{\text{sent}} - z_{\text{LRRR}})^2\right]\end{aligned}$$

$$\frac{\partial \rho_{\text{sent}}}{\partial v_{x,\text{sent}}} = \frac{1}{2}\Big[(x_{\text{sent}} - x_{\text{LRRR}})^2 + (y_{\text{sent}} - y_{\text{LRRR}})^2 + (z_{\text{sent}} - z_{\text{LRRR}})^2\Big]^{-1/2} \times$$
$$\Big[2(x_{\text{sent}} - x_{\text{LRRR}})\frac{\partial x_{\text{sent}}}{\partial v_{x,\text{sent}}} + 2(y_{\text{sent}} - y_{\text{LRRR}})\frac{\partial y_{\text{sent}}}{\partial v_{x,\text{sent}}} + 2(z_{\text{sent}} - z_{\text{LRRR}})\frac{\partial z_{\text{sent}}}{\partial v_{x,\text{sent}}}\Big] = 0$$

The second term:

$$\frac{\partial \rho_{\text{recieved}}}{\partial v_{x,\text{sent}}} = \frac{\partial}{\partial v_{x,\text{sent}}}\Big[(x_{\text{recieved}} - x_{\text{LRRR}})^2 + (y_{\text{recieved}} - y_{\text{LRRR}})^2 + (z_{\text{recieved}} - z_{\text{LRRR}})^2\Big]^{1/2}$$

$$\frac{\partial \rho_{\text{recieved}}}{\partial v_{x,\text{sent}}} = \frac{1}{2}\Big[(x_{\text{recieved}} - x_{\text{LRRR}})^2 + (y_{\text{recieved}} - y_{\text{LRRR}})^2 + (z_{\text{recieved}} - z_{\text{LRRR}})^2\Big]^{-1/2} \times$$
$$\Big[\frac{\partial}{\partial v_{x,\text{sent}}}(x_{\text{recieved}} - x_{\text{LRRR}})^2 + \frac{\partial}{\partial v_{x,\text{sent}}}(y_{\text{recieved}} - y_{\text{LRRR}})^2 + \frac{\partial}{\partial v_{x,\text{sent}}}(z_{\text{recieved}} - z_{\text{LRRR}})^2\Big]$$

$$\frac{\partial \rho_{\text{recieved}}}{\partial v_{x,\text{sent}}} = \frac{1}{2}\Big[(x_{\text{recieved}} - x_{\text{LRRR}})^2 + (y_{\text{recieved}} - y_{\text{LRRR}})^2 + (z_{\text{recieved}} - z_{\text{LRRR}})^2\Big]^{-1/2} \times$$
$$\Big[2(x_{\text{recieved}} - x_{\text{LRRR}})\frac{\partial x_{\text{recieved}}}{\partial v_{x,\text{sent}}} + 2(y_{\text{recieved}} - y_{\text{LRRR}})\frac{\partial y_{\text{recieved}}}{\partial v_{x,\text{sent}}} + 2(z_{\text{recieved}} - z_{\text{LRRR}})\frac{\partial z_{\text{recieved}}}{\partial v_{x,\text{sent}}}\Big]$$

$$\frac{\partial \rho_{\text{recieved}}}{\partial v_{x,\text{sent}}} = \Big[(x_{\text{recieved}} - x_{\text{LRRR}})^2 + (y_{\text{recieved}} - y_{\text{LRRR}})^2 + (z_{\text{recieved}} - z_{\text{LRRR}})^2\Big]^{-1/2} \times$$
$$\Big[(x_{\text{recieved}} - x_{\text{LRRR}})\frac{\partial x_{\text{recieved}}}{\partial v_{x,\text{sent}}} + (y_{\text{recieved}} - y_{\text{LRRR}})\frac{\partial y_{\text{recieved}}}{\partial v_{x,\text{sent}}} + (z_{\text{recieved}} - z_{\text{LRRR}})\frac{\partial z_{\text{recieved}}}{\partial v_{x,\text{sent}}}\Big]$$

$$\frac{\partial \rho_{\text{recieved}}}{\partial v_{x,\text{sent}}} = \Big[(x_{\text{recieved}} - x_{\text{LRRR}})^2 + (y_{\text{recieved}} - y_{\text{LRRR}})^2 + (z_{\text{recieved}} - z_{\text{LRRR}})^2\Big]^{-1/2} \times$$
$$\Big[(x_{\text{recieved}} - x_{\text{LRRR}})\Phi(1,4) + (y_{\text{recieved}} - y_{\text{LRRR}})\Phi(2,4) + (z_{\text{recieved}} - z_{\text{LRRR}})\Phi(3,4)\Big]$$

$$\frac{\partial \rho_{\text{recieved}}}{\partial v_{x,\text{sent}}} = \rho_{\text{recieved}}^{-1} \boldsymbol{\rho}_{\text{received}}^{T} \Phi(1:3,4) \tag{A.20}$$

The third term, $\frac{\partial \rho_{\text{recieved}}}{\partial \Delta t}$, is the same as calculated for the position state derivatives above.

Combining all three terms:

$$\begin{aligned} \frac{\partial \Delta t}{\partial v_{x,\text{sent}}} &= \frac{\frac{\partial \rho_{\text{sent}}}{\partial v_{x,\text{sent}}} + \frac{\partial \rho_{\text{recieved}}}{\partial v_{x,\text{sent}}}}{c - \frac{\partial \rho_{\text{recieved}}}{\partial \Delta t}} \\ &= \frac{0 + \rho_{\text{recieved}}^{-1} \boldsymbol{\rho}_{\text{received}}^{T} \Phi(1:3,4)}{c - v_{x,\text{received}} \boldsymbol{\rho}_{\text{recieved}}(1) \rho_{\text{recieved}}^{-1}} \\ &= \frac{\rho_{\text{recieved}}^{-1} \boldsymbol{\rho}_{\text{received}}^{T} \Phi(1:3,4)}{c - \rho_{\text{recieved}}^{-1} \boldsymbol{\rho}_{\text{recieved}}(1) v_{x,\text{received}}} \end{aligned} \tag{A.21}$$

Following a the same procedure for the y component of velocity:

$$\frac{\partial \Delta t}{\partial v_{y,\text{sent}}} = \frac{\frac{\partial \rho_{\text{sent}}}{\partial v_{y,\text{sent}}} + \frac{\partial \rho_{\text{recieved}}}{\partial v_{y,\text{sent}}}}{c - \frac{\partial \rho_{\text{recieved}}}{\partial \Delta t}} \tag{A.22}$$

$$\frac{\partial \rho_{\text{sent}}}{\partial v_{y,\text{sent}}} = \frac{\partial}{\partial v_{y,\text{sent}}} \Big[(x_{\text{sent}} - x_{\text{LRRR}})^2 + (y_{\text{sent}} - y_{\text{LRRR}})^2 + (z_{\text{sent}} - z_{\text{LRRR}})^2 \Big]^{1/2}$$

$$\begin{aligned} \frac{\partial \rho_{\text{sent}}}{\partial v_{y,\text{sent}}} = \frac{1}{2} &\Big[(x_{\text{sent}} - x_{\text{LRRR}})^2 + (y_{\text{sent}} - y_{\text{LRRR}})^2 + (z_{\text{sent}} - z_{\text{LRRR}})^2 \Big]^{-1/2} \times \\ &\Big[\frac{\partial}{\partial v_{y,\text{sent}}} (x_{\text{sent}} - x_{\text{LRRR}})^2 + \frac{\partial}{\partial v_{y,\text{sent}}} (y_{\text{sent}} - y_{\text{LRRR}})^2 + \frac{\partial}{\partial v_{y,\text{sent}}} (z_{\text{sent}} - z_{\text{LRRR}})^2 \Big] \end{aligned}$$

$$\frac{\partial \rho_{\text{sent}}}{\partial v_{y,\text{sent}}} = \frac{1}{2}\Big[(x_{\text{sent}} - x_{\text{LRRR}})^2 + (y_{\text{sent}} - y_{\text{LRRR}})^2 + (z_{\text{sent}} - z_{\text{LRRR}})^2\Big]^{-1/2} \times$$
$$\Big[2(x_{\text{sent}} - x_{\text{LRRR}})\frac{\partial \cancel{x_{\text{sent}}}}{\partial v_{y,\text{sent}}} + 2(y_{\text{sent}} - y_{\text{LRRR}})\frac{\partial \cancel{y_{\text{sent}}}}{\partial v_{y,\text{sent}}} + 2(z_{\text{sent}} - z_{\text{LRRR}})\frac{\partial \cancel{z_{\text{sent}}}}{\partial v_{y,\text{sent}}}\Big] = 0$$

The second term:

$$\frac{\partial \rho_{\text{recieved}}}{\partial v_{y,\text{sent}}} = \frac{\partial}{\partial v_{y,\text{sent}}}\Big[(x_{\text{recieved}} - x_{\text{LRRR}})^2 + (y_{\text{recieved}} - y_{\text{LRRR}})^2 + (z_{\text{recieved}} - z_{\text{LRRR}})^2\Big]^{1/2}$$

$$\frac{\partial \rho_{\text{recieved}}}{\partial v_{y,\text{sent}}} = \frac{1}{2}\Big[(x_{\text{recieved}} - x_{\text{LRRR}})^2 + (y_{\text{recieved}} - y_{\text{LRRR}})^2 + (z_{\text{recieved}} - z_{\text{LRRR}})^2\Big]^{-1/2} \times$$
$$\Big[\frac{\partial}{\partial v_{y,\text{sent}}}(x_{\text{recieved}} - x_{\text{LRRR}})^2 + \frac{\partial}{\partial v_{y,\text{sent}}}(y_{\text{recieved}} - y_{\text{LRRR}})^2 + \frac{\partial}{\partial v_{y,\text{sent}}}(z_{\text{recieved}} - z_{\text{LRRR}})^2\Big]$$

$$\frac{\partial \rho_{\text{recieved}}}{\partial v_{y,\text{sent}}} = \frac{1}{2}\Big[(x_{\text{recieved}} - x_{\text{LRRR}})^2 + (y_{\text{recieved}} - y_{\text{LRRR}})^2 + (z_{\text{recieved}} - z_{\text{LRRR}})^2\Big]^{-1/2} \times$$
$$\Big[2(x_{\text{recieved}} - x_{\text{LRRR}})\frac{\partial x_{\text{recieved}}}{\partial v_{y,\text{sent}}} + 2(y_{\text{recieved}} - y_{\text{LRRR}})\frac{\partial y_{\text{recieved}}}{\partial v_{y,\text{sent}}} + 2(z_{\text{recieved}} - z_{\text{LRRR}})\frac{\partial z_{\text{recieved}}}{\partial v_{y,\text{sent}}}\Big]$$

$$\frac{\partial \rho_{\text{recieved}}}{\partial v_{y,\text{sent}}} = \Big[(x_{\text{recieved}} - x_{\text{LRRR}})^2 + (y_{\text{recieved}} - y_{\text{LRRR}})^2 + (z_{\text{recieved}} - z_{\text{LRRR}})^2\Big]^{-1/2} \times$$
$$\Big[(x_{\text{recieved}} - x_{\text{LRRR}})\frac{\partial x_{\text{recieved}}}{\partial v_{y,\text{sent}}} + (y_{\text{recieved}} - y_{\text{LRRR}})\frac{\partial y_{\text{recieved}}}{\partial v_{y,\text{sent}}} + (z_{\text{recieved}} - z_{\text{LRRR}})\frac{\partial z_{\text{recieved}}}{\partial v_{y,\text{sent}}}\Big]$$

$$\frac{\partial \rho_{\text{recieved}}}{\partial v_{y,\text{sent}}} = \Big[(x_{\text{recieved}} - x_{\text{LRRR}})^2 + (y_{\text{recieved}} - y_{\text{LRRR}})^2 + (z_{\text{recieved}} - z_{\text{LRRR}})^2\Big]^{-1/2} \times$$
$$\Big[(x_{\text{recieved}} - x_{\text{LRRR}})\Phi(1,5) + (y_{\text{recieved}} - y_{\text{LRRR}})\Phi(2,5) + (z_{\text{recieved}} - z_{\text{LRRR}})\Phi(3,5)\Big]$$

$$\frac{\partial \rho_{\text{recieved}}}{\partial v_{y,\text{sent}}} = \rho_{\text{recieved}}^{-1} \boldsymbol{\rho}_{\text{received}}^{T} \Phi(1:3,5)$$

Again, the third term, $\frac{\partial \rho_{\text{recieved}}}{\partial \Delta t}$, is the same as calculated for the position state derivatives above.

Combining all three terms:

$$\begin{aligned}
\frac{\partial \Delta t}{\partial v_{y,\text{sent}}} &= \frac{\frac{\partial \rho_{\text{sent}}}{\partial v_{y,\text{sent}}} + \frac{\partial \rho_{\text{recieved}}}{\partial v_{y,\text{sent}}}}{c - \frac{\partial \rho_{\text{recieved}}}{\partial \Delta t}} \\
&= \frac{0 + \rho_{\text{recieved}}^{-1} \boldsymbol{\rho}_{\text{received}}^{T} \Phi(1:3,5)}{c - v_{y,\text{received}} \boldsymbol{\rho}_{\text{recieved}}(2) \rho_{\text{recieved}}^{-1}} \\
&= \frac{\rho_{\text{recieved}}^{-1} \boldsymbol{\rho}_{\text{received}}^{T} \Phi(1:3,5)}{c - \rho_{\text{recieved}}^{-1} \boldsymbol{\rho}_{\text{recieved}}(2) v_{y,\text{received}}}
\end{aligned} \tag{A.23}$$

Mirroring the pattern of Equations A.21 and A.23 for the z velocity component:

$$\begin{aligned}
\frac{\partial \Delta t}{\partial v_{z,\text{sent}}} &= \frac{\frac{\partial \rho_{\text{sent}}}{\partial v_{z,\text{sent}}} + \frac{\partial \rho_{\text{recieved}}}{\partial v_{z,\text{sent}}}}{c - \frac{\partial \rho_{\text{recieved}}}{\partial \Delta t}} \\
&= \frac{\rho_{\text{recieved}}^{-1} \boldsymbol{\rho}_{\text{received}}^{T} \Phi(1:3,6)}{c - \rho_{\text{recieved}}^{-1} \boldsymbol{\rho}_{\text{recieved}}(3) v_{z,\text{received}}}
\end{aligned} \tag{A.24}$$

Consolidating Equations A.21, A.23, and A.24 into vector form:

$$\begin{aligned}
\frac{\partial \Delta t}{\partial \boldsymbol{v}_{\text{sent}}} &= \frac{\frac{\partial \rho_{\text{sent}}}{\partial \boldsymbol{v}_{\text{sent}}} + \frac{\partial \rho_{\text{recieved}}}{\partial \boldsymbol{v}_{\text{sent}}}}{c - \frac{\partial \rho_{\text{recieved}}}{\partial \Delta t}} \\
&= \frac{\rho_{\text{recieved}}^{-1} \boldsymbol{\rho}_{\text{received}}^{T} \Phi(1:3,4:6)}{c - \rho_{\text{recieved}}^{-1} \boldsymbol{\rho}_{\text{received}}^{T} \boldsymbol{v}_{\text{recieved}}} \\
&= \frac{\boldsymbol{\rho}_{\text{received}}^{T} \Phi_{\boldsymbol{rv}}}{\rho_{\text{recieved}} c - \boldsymbol{\rho}_{\text{received}}^{T} \boldsymbol{v}_{\text{recieved}}}
\end{aligned} \tag{A.25}$$

The state transition matrix between t_{sent} and t_{recieved} is:

$$\Phi(t_{\text{recieved}}, t_{\text{sent}}) = \begin{bmatrix} \Phi_{\boldsymbol{rr}} & \Phi_{\boldsymbol{rv}} \\ \Phi_{\boldsymbol{vr}} & \Phi_{\boldsymbol{vv}} \end{bmatrix} = \begin{bmatrix} \frac{\partial \boldsymbol{r}_{\text{recieved}}}{\partial \boldsymbol{r}_{\text{sent}}} & \frac{\partial \boldsymbol{v}_{\text{recieved}}}{\partial \boldsymbol{r}_{\text{sent}}} \\ \frac{\partial \boldsymbol{r}_{\text{recieved}}}{\partial \boldsymbol{v}_{\text{sent}}} & \frac{\partial \boldsymbol{v}_{\text{recieved}}}{\partial \boldsymbol{v}_{\text{sent}}} \end{bmatrix}$$

$$= \begin{bmatrix} \frac{\partial x_{\text{recieved}}}{\partial x_{\text{sent}}} & \frac{\partial x_{\text{recieved}}}{\partial y_{\text{sent}}} & \frac{\partial x_{\text{recieved}}}{\partial z_{\text{sent}}} & \frac{\partial x_{\text{recieved}}}{\partial v_{x,\text{sent}}} & \frac{\partial x_{\text{recieved}}}{\partial v_{y,\text{sent}}} & \frac{\partial x_{\text{recieved}}}{\partial v_{z,\text{sent}}} \\ \frac{\partial y_{\text{recieved}}}{\partial x_{\text{sent}}} & \frac{\partial y_{\text{recieved}}}{\partial y_{\text{sent}}} & \frac{\partial y_{\text{recieved}}}{\partial z_{\text{sent}}} & \frac{\partial y_{\text{recieved}}}{\partial v_{x,\text{sent}}} & \frac{\partial y_{\text{recieved}}}{\partial v_{y,\text{sent}}} & \frac{\partial y_{\text{recieved}}}{\partial v_{z,\text{sent}}} \\ \frac{\partial z_{\text{recieved}}}{\partial x_{\text{sent}}} & \frac{\partial z_{\text{recieved}}}{\partial y_{\text{sent}}} & \frac{\partial z_{\text{recieved}}}{\partial z_{\text{sent}}} & \frac{\partial z_{\text{recieved}}}{\partial v_{x,\text{sent}}} & \frac{\partial z_{\text{recieved}}}{\partial v_{y,\text{sent}}} & \frac{\partial z_{\text{recieved}}}{\partial v_{z,\text{sent}}} \\ \frac{\partial v_{x,\text{received}}}{\partial x_{\text{sent}}} & \frac{\partial v_{x,\text{received}}}{\partial y_{\text{sent}}} & \frac{\partial v_{x,\text{received}}}{\partial z_{\text{sent}}} & \frac{\partial v_{x,\text{received}}}{\partial v_{x,\text{sent}}} & \frac{\partial v_{x,\text{received}}}{\partial v_{y,\text{sent}}} & \frac{\partial v_{x,\text{received}}}{\partial v_{z,\text{sent}}} \\ \frac{\partial v_{y,\text{received}}}{\partial x_{\text{sent}}} & \frac{\partial v_{y,\text{received}}}{\partial y_{\text{sent}}} & \frac{\partial v_{y,\text{received}}}{\partial z_{\text{sent}}} & \frac{\partial v_{y,\text{received}}}{\partial v_{x,\text{sent}}} & \frac{\partial v_{y,\text{received}}}{\partial v_{y,\text{sent}}} & \frac{\partial v_{y,\text{received}}}{\partial v_{z,\text{sent}}} \\ \frac{\partial v_{z,\text{received}}}{\partial x_{\text{sent}}} & \frac{\partial v_{z,\text{received}}}{\partial y_{\text{sent}}} & \frac{\partial v_{z,\text{received}}}{\partial z_{\text{sent}}} & \frac{\partial v_{z,\text{received}}}{\partial v_{x,\text{sent}}} & \frac{\partial v_{z,\text{received}}}{\partial v_{y,\text{sent}}} & \frac{\partial v_{z,\text{received}}}{\partial v_{z,\text{sent}}} \end{bmatrix} \tag{A.26}$$

The measurement function (Eqn. 3.8) then becomes:

$$\begin{aligned} \underline{h}(\boldsymbol{r}_{\text{sent}}, \boldsymbol{r}_{\text{received}}) &= \Delta t \\ &= \frac{\rho_{\text{sent}} + \rho_{\text{received}}}{c} \end{aligned} \tag{A.27}$$

The Jacobian of the measurement function becomes:

$$\begin{aligned} H &= \frac{\partial \underline{h}}{\partial \boldsymbol{X}_{\text{sent}}} \\ &= \begin{bmatrix} \frac{\partial \Delta t}{\partial x_{\text{sent}}} & \frac{\partial \Delta t}{\partial y_{\text{sent}}} & \frac{\partial \Delta t}{\partial z_{\text{sent}}} & \frac{\partial \Delta t}{\partial \dot{x}_{\text{sent}}} & \frac{\partial \Delta t}{\partial \dot{y}_{\text{sent}}} & \frac{\partial \Delta t}{\partial \dot{z}_{\text{sent}}} \end{bmatrix} \\ &= \begin{bmatrix} \frac{\partial \Delta t}{\partial \boldsymbol{r}_{\text{sent}}} & \frac{\partial \Delta t}{\partial \dot{\boldsymbol{r}}_{\text{sent}}} \end{bmatrix} \\ &= \begin{bmatrix} \frac{\rho_{\text{received}} \boldsymbol{\rho}_{\text{sent}}^T + \rho_{\text{sent}} \boldsymbol{\rho}_{\text{received}}^T \Phi_{\boldsymbol{rr}}}{\rho_{\text{sent}}(c\rho_{\text{received}} - \boldsymbol{\rho}_{\text{received}}^T \boldsymbol{v}_{\text{received}})} & \frac{\boldsymbol{\rho}_{\text{received}}^T \Phi_{\boldsymbol{rv}}}{c\rho_{\text{received}} - \boldsymbol{\rho}_{\text{received}}^T \boldsymbol{v}_{\text{received}}} \end{bmatrix} \end{aligned} \tag{A.28}$$